ABSTRACT

Title of dissertation: ACTIVE CONTROL OF PERFORMANCE AND VIBRATORY LOADS USING TRAILING-EDGE FLAPS AND LEADING-EDGE SLATS
Kumar Ravichandran
Doctor of Philosophy, 2019

Dissertation directed by: Professor Inderjit Chopra
Department of Aerospace Engineering

The objective of this research work is to develop a comprehensive analysis version of UMARC (University of Maryland Advanced Rotor Code) to study the capabilities of trailing-edge flaps (TEFs)and leading-edge slats (LESs) for helicopter vibration reduction and performance improvement and recommend flap and slat configurations for a typical helicopter rotor such as UH-60A rotor, which maximize these benefits. This study uses propulsive free-flight trim except in hover. Using TEFs , the rotor performance in hover was improved with a combination of torsionally softer blades and positive TEF deflections. For the vibration reduction studies, a multicyclic control algorithm was used to determine the actuation schedule . Suitable combinations of lower harmonic TEF inputs were shown capable of reducing the rotor power requirement by about 4-5 % at an advance ratio of $\mu = 0.4$. The TEF was shown to be capable of suppressing the vibratory loads at a range of forward speeds, using half peak-to-peak deflections of about $5^\circ - 10^\circ$. Softening the blades in torsion resulted in larger flap actuation requirements for vibration reduction.

Parametric sweeps of TEF actuations were carried out to determine suitable combinations of steady and various frequencies of actuation of flaps , which yield overall power reductions and it is observed that a combination of 1, 2, 3, 4 and 5/rev TEF inputs resulted in a power reduction of 1.5% , while also reducing certain vibratory loads by more than 50% in high speed-forward flight.

To explore the advantages of leading-edge slats, the slatted airfoils with configurations S0, S1 and S6 (used by Sikorsky) were used.The slatted blade sections had the SC2110 baseline/slatted airfoils in place of the baseline UH-60A airfoils. Dynamic actuations are chosen to retain the high-lift benefits of the slats while seeking to minimize profile drag penalties over regions of the rotor disk operating at lower angles of attack, i.e., the advancing side.The effects of leading-edge slats extending over 20%, 30% and 40% of the blade span on rotor performance and vibratory hub loads were examined. The study uses propulsive free flight trim. In moderate to high-speed forward flight,leading-edge slats were shown to enhance the maximum rotor thrust by 15-30% at advance ratios larger than 0.2 and reduce power requirements by 10-20% at high thrust levels. 20% span slats offered a good compromise between power reductions and adverse effect on vibratory hub loads.The rotor with leading-edge slats could be trimmed at a maximum forward speed that was about 20 knots greater than for the baseline rotor with no slats.

This study also shows that additional power reduction is achievable by suitable TEF deployments superimposed on certain slat actuations in high-speed forward flight.

ACTIVE CONTROL OF PERFORMANCE AND VIBRATORY LOADS USING TRAILING-EDGE FLAPS AND LEADING-EDGE SLATS

by

Kumar Ravichandran

Dissertation submitted to the Faculty of the Graduate School of the
University of Maryland, College Park in partial fulfillment
of the requirements for the degree of
Doctor of Philosophy
2019

Advisory Committee:
Professor Inderjit Chopra, Chair/Advisor
Professor James Baeder
Professor Olivier A. Bauchau
Associate Professor Anubhav Datta
Associate Professor Nikhil Chopra (Dean's representative)

Acknowledgments

I am pleased to put down all that went through my mind as part of this experience. I would like to thank my advisor, Dr. Inderjit Chopra, my longtime pillar of support, for his dedication and single-mindedness. He guided me first and foremost, but for all my mistakes he put up with, I have to thank him over again.He was instrumental in shaping a great deal of my research.

My special thanks to Dr. V. Nagaraj for his help.

In addition, former students of my advisor, most notably Dr. Jaye Falls and Dr. Anubhav Datta (now Associate professor,Department of Aerospace Engineering, UMD), for sharing their expertise with UMARC.

This research was partially funded by the Aviation Applied Technology Directorate (AATD) and I wish to record my gratitude to Sikorsky Aircraft, Stratford, CT, for their longtime support.

My colleagues at the Alfred Gessow Rotorcraft Center have been very helpful in providing technical assistance. I would like to thank Benjamin Hein, Senior Engineer of Sikorsky Aircraft and Brian E. Wake, Technical Fellow, UTRC(now at Sikorsky), for many discussions.

I would like to mention my colleagues Anand Saxena, Ananth Sridharan, Graham Bowen-Davies, Chen Friedman, Sivaji Medida, for their contributions to my work.

I would like to acknowledge Dr. Shreyas Ananthan, who helped me with so much throughout this research he served as the additional advisor whenever I had

doubts. He was the bedrock for an entire office of students.

A special and grateful bow to my parents who have displayed a firm conviction which has truly astonished me considering how long this process has lasted. I would like to thank my brother as well, who stood with me during my difficult phases.

Table of Contents

List of Tables

List of Figures

Chapter 1: Introduction

1.1 Background

In recent years, modern rotor technology has been evolving to target the requirements for next generation rotorcraft by extending the operational flight envelopes in terms of achievable forward flight speeds, payload capability and maneuverability. Each of these objectives is a function primarily of the aerodynamic performance of the main rotor, which operates in a complex aerodynamic environment, varying from low dynamic pressures and high angles of attack on the retreating side of the disk to high dynamic pressures and low angles of attack on the advancing side. The overall aerodynamic environment of the helicopter in forward flight in (Fig. 1.1) is discussed in Refs. 1-2.

The maximum speed that a helicopter can attain depends on the maximum lift that the rotor disk can produce on the retreating side. Today, all helicopters use cyclic pitch control for varying their lift as the blades rotate but the lift can only be maintained by increasing the angle of attack upto the stalling point of the airfoil. In the case of the blade, the stall is dynamic due to the unsteady nature of

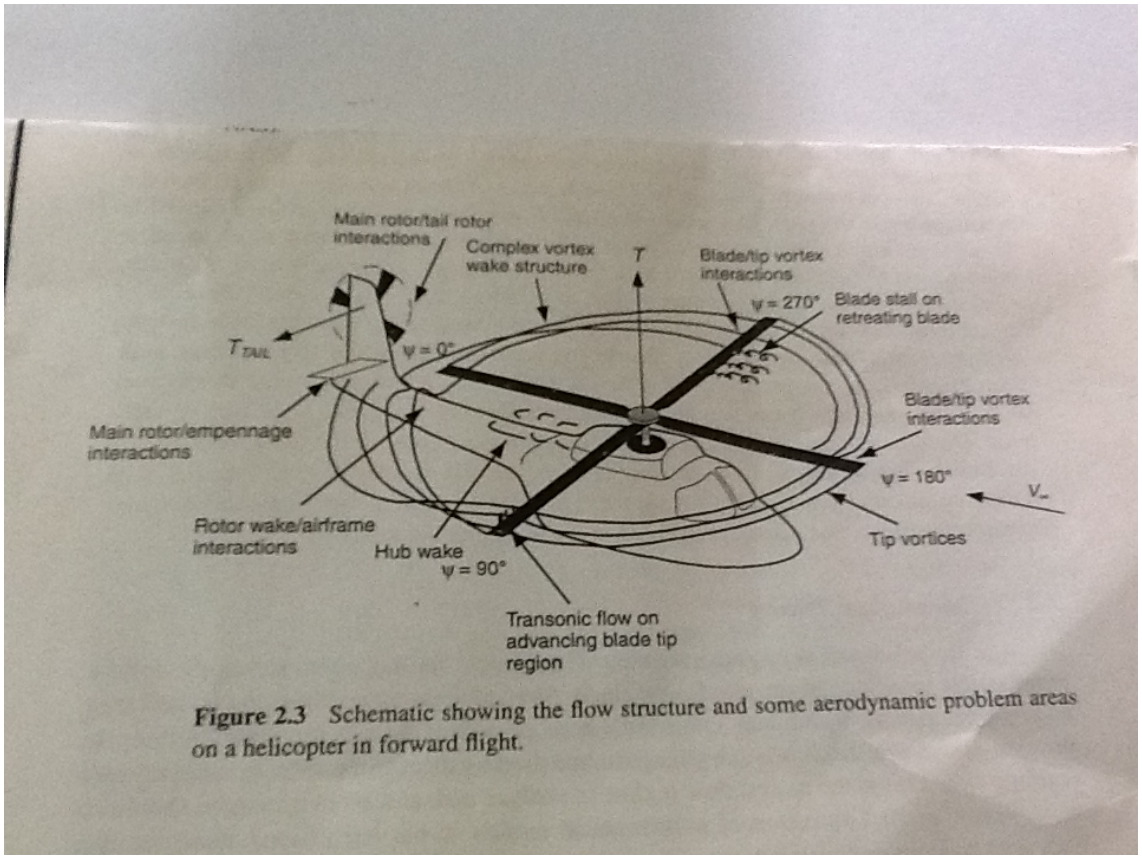

Figure 1.1: Flow structure and some aerodynamic problem areas on a helicopter in forward flight

the flow. Blade stall causes a significant increase of vibratory loads.Hence, the rotor technology has tended toward methods of active control to minimize vibrations and enhance performance over a wide range of operating conditions.

Passive designs involving blade geometry that seek to improve the aerodynamic performance of the main rotor usually focus on airfoil sections as a first step and are faced with the conflicting challenges of the advancing blade compressibility and retreating blade stall. Designs for higher lift in low speed regimes lead to high drag at higher speeds and designs that target low drag under high speed conditions do not achieve the desired lift enhancement at lower speeds. While airfoil technology has come a long way in overcoming specific aerodynamic limitations, any further dramatic improvements in lift characteristics without associated moment or drag penalties may not be feasible for conventional fixed-geometry rotors with single-element airfoils. Targeting vibration reduction can improve the helicopter blade life while stall alleviation can expand the lift envelope.

1.2 Vibration

Helicopters are prone to high vibration levels, which affect the lives of structural components adversely. The primary source of vibration in the helicopter is the main rotor. Vibratory loads can be attributed to the highly unsteady edgewise flow-field and complex wake structure surrounding the rotor, the aeroelastically coupled blade motions, rotor-fuselage interactions and time-varying control inputs, which

affect the lives of structural components adversely.

Considerable emphasis is being laid on the reduction of helicopter noise to improve community acceptance because many of the helicopters in civilian use operate close to urban and populated areas. Further,the impact of vibrations on the comfort of passengers and crew, as well as on the reliability of onboard equipment is also important.

Vibration is the dynamic response of the helicopter airframe and other components in the non-rotating frame due to the rotor hub forces and moments. The aerodynamic loads on the main fuselage and tail produced by the rotor wake can also contribute to airframe vibration. There are also other important sources of helicopter vibration,notably the engine and transmission, but the primary source of vibration in the helicopter is the main rotor. In steady-state forward flight, the periodic forces at the root of the blade are transmitted to the helicopter, producing a periodic vibratory response. For a rotor with N_b identical blades, the main rotor hub acts as a filter for the blade loads and only transmits harmonic loads at multiples of N_b/rev to the fuselage. This is based on the assumption that all the blades are identical and have the same periodic motion. Although this is not practically true, the N_b/rev harmonics still dominate the vibrations.Thus, typically, the N_b /rev components of the vibratory hub loads are the most dominant. The vibration is generally low in hover, where the aerodynamic environment is nearly axisymmetric and cyclic pitch nearly zero, and increases with forward speed to high levels at the maximum speed of the helicopter. There is also a high level of vibration at transition ($\mu \sim 0.15$) because of the dominance of rotor wake influence on

the blade airloads. The vibration increases with descent at low speed and increases with thrust at high speeds ([2] and [3]). Because the helicopter drag is small at low speeds, the tip path plane incidence remains small, and the tip vortices in the wake remain close to the disk plane. The advance ratio is low enough so that the blades sweep past the tip vortices from preceding blades. Such close blade-vortex interactions produce significant higher harmonic airloading, that is transmitted to the hub.This vibration is increased by operations that keep the wake near the disk plane, such as decelerating or descending flight. As the speed increases, the helicopter rotor tip-path-plane tilts forward to provide the propulsive force,which means that the wake is convected away from the disc plane and the wake-induced vibration decreases.At still higher speeds, the vibration increases again,primarily as a result of the higher harmonic loading produced by stall and compressibility effects. Large vibratory loads can limit the maximum speed of the aicraft, as any aerodynamic or inertial dissimilarity between the blades primarily generates 1/rev vibrations.

The specifications for rotorcraft vibration have been gradually evolving over time. The specification is in terms of acceleration,velocity or displacement, which can be converted to acceleration in g's as a function of frequency. The U.S. Government documents MIL-8501(1952)(Ref [4]) and MIL-8501A(Ref [5]) provide the limits for various locations in the rotorcraft (pilot,crew,passengers,litters) and for steady flight upto cruise speed. The MIL-H-8501A(1961) refined the limit at high frequency,but also increased the limit to 50 % relative to MIL-H-8501(1952), reflecting an assessment of what the technology could provide.

The design standard ADS-27A-SP(2006)([6]] defines an intrusion index, based

on the vibration spectra,for the longitudinal, lateral and vertical directions at a location. The intrusion index is the square root of the sum of the squares of the 4 largest peaks(excluding 1/rev) for each of the 3 normalized spectra.An intrusion index limit is defined for various operating conditions and positions in the aircraft. The vibration requirement is that the intrusion index be lower than the intrusion index limit. Keeping in view what is possible with the technology available,the specifications have become more elaborate. The vibration level permitted has been increased,especially at low speeds,but a distinction is made between the levels permissible in the cabin and cockpit. Specifications for particular rotorcraft have used the Intrusion Index,but with increased limits. The requirements for the comfort of the crew and passengers are only likely to get more demanding over time and hence vibration prediction and control will continue to pose significant challenges in rotorcraft design.

1.3 Vibration reduction techniques

Vibration reduction can be accomplished by minimizing the source vibratory loads at the source,i.e.the rotor .The oscillatory hub forces and moments,including the aerodynamic loads acting on the fuselage and tail must be reduced to minimize the response of the structure. Vibration reduction methods can be passive or active.

Passive vibration reduction methods such as pendulum absorbers ([7], [8] and [9]) or rotor blade modal shaping ([10] and [11]) or frequency attenuators generally have poor off-design performance as well as a significant weight penalty([12]

and [13]). Further, proper operation of the pendulum absorbers requires minimum friction in the pendulum hinges.A centrifugal pendulum absorber was developed by Viswanathan [14] et.al, which employs mercury as the tuning weight and flight tests performed on Bell Helicopter models 206LM and 412 showed that the mercury pendulum absorbers were effective in reducing cabin vibration.This has not been put to commercial use,probably because of environmental and corrosion considerations.

Blade-mounted pendulum absorbers also change orientation with changes in blade collective and cyclic pitch,resulting in adverse coupling of the blade flatwise and inplane motions ([15]). Both bifilar and pendulum absorbers produce aerodynamic drag penalties.Other passive methods such as aeroelastic optimization([16]) and composite couplings ([17]) may not have the weight penalty, but may not be optimum for a range of flight conditions.

Active vibration control in the fixed frame enhances vibration reduction, possibly at reduced weight penalty ([18]). However,these systems cannot address the source of the vibration but have significant effect on drive system space around the gearbox. Regarding the various categories of frequency attenuators, they are broadly related to the topic of blade structural optimization ([19], [20], [21], [22]). However,it is not evident whether structural optimization alone without additional vibration treatment can lead to acceptable vibration reduction. The various other methods of rotor control include:

- Blade camber control-asymmetric actuation using smart materials around the blade sections.Harmonic actuations at 2/rev could reduce the noise and vibratory loads on the rotor,improving the rotor performance ([23], [24]).

- Blade twist control-differential actuation using smart materials arranged along the blade span. The idea behind active twist is to modify twist distribution of the rotating blade, not only to improve the lift and overall helicopter performance, but also to actively control vibrations.

  Chen et.al.([25]) pioneered torsion actuation by designing and testing a Froude-scale model embedded with specially-shaped piezoelectric elements. Blade twist of the order of $\pm 0.4^{\circ}$ at the tip showed the potential of the system for vibration suppression.

  Wilbur et.al.([26]) carried out experimental studies in the NASA Langley Transonic Dynamics Tunnel on a 4-bladed, active twist rotor, and reported significant reductions in fixed-system loads of $60-95\%$ with active blade twist upto 1.4°.

  Studies by Thakkar et.al.([27]) show that about 69 % reduction can be achieved using a distributed actuation system, to modify the blade twist with the actuation of two sections.

  The disadvantage in this approach is it requires significantly increased actuation for twisting the entire blade compared to that required for small flaps.

- Blade pitch control: individual blade pitch actuation in the rotating frame.It results in the complexity of power slipring.

- Tilting shaft: In order to orient the rotor thrust suitably.It requires a large actuation force.

- Servo flaps: on-blade airfoil sections located aft of the trailing edges of the rotor blades.These result in large drag penalty.

Direct blade control as in the first three methods, requires large actuation forces and complex actuation systems, as does the tilting shaft concept. Servo flaps incur extra weight and drag penalties due to the extra supports, and gaps between the flaps and the hinges.

Other active control methods that use multicyclic pitch excitation of the swashplate, can be far more effective because they eliminate vibration at its source.These systems actuate the rotor blades at higher harmonics to generate unsteady forces, which counteract existing vibratory airloads. These techniques include higher harmonic control and individual blade control.

1.3.1 Higher harmonic control

Higher harmonic control(HHC),where the blades are activated in the non-rotating frame by the swashplate by introducing pitch commands at N_b/rev resulting in blade pitch oscillations at frequencies of N_b-1/rev, N_b/rev, N_b+1/rev in the rotating frame. If applied with the correct phasing, HHC can result in significant vibration reduction. If these blade pitch actuations are applied appropriately,they can generate a combination of aerodynamic and inertial loads to counteract the existing blade loads,which cause airframe vibration. HHC has been studied using numerical simulations ([28], [29], [30], [31], [32]), model-scale ([33], [34], [35], [36])as well

as full scale rotor tests([37], [38], [39]) in wind tunnels.HHC produces substantial reductions in vibration. A comprehensive analytical formulation was developed to examine the problems associated with the implementation of HHC to reduce vibration for hingeless rotors ([40]).The study showed that flap,lag and torsion characteristics,offset of blade centre of mass from elastic axis, offset of elastic axis from blade quarter-chord axis,and blade thrust greatly affect the HHC actuator power requirement. However, HHC can not address other control objectives like performance improvement,stall alleviation and power reduction as these may require excitation of the blades at harmonics other than N_b/rev. The search for a solution to these issues resulted in the development of Individual Blade Control(IBC).

1.3.2 Individual Blade Control

In IBC, each blade can be controlled independently in the rotating frame. Several implementations of IBC are available. In HHC for a N-bladed rotor, excitation of the swashplate allows only N_b/rev, N_b -1/rev and N_b +1/rev excitation of the rotor blades.IBC can be used to generate 2/rev and other harmonics in the rotating frame.IBC also allows feedback loops for each blade in the rotating frame.Kretz ([41]) used a rotor-control system characterized by the fact that each blade is governed independently by a fixed feedback system comprising an electrohydraulic actuator as the main power element to alleviate instabilities at high advance ratios and high lift coefficients. Significant work on IBC was conducted by Ham ([42], [43], [44]). In the conventional IBC approach,the pitch of each rotor blade is individually controlled in the rotating frame using servo-actuators. This higher

harmonic pitch input is superimposed on the pilot pitch input. The IBC shows considerable potential to achieve not only vibration reduction,but also noise reduction and performance enhancement. However,both HHC and IBC require complex mechanisms for actuation and associated weight penalties and considerable actuation forces.

1.4 Performance enhancement techniques

Gurney flap is a small flap deployed vertically at the trailing edge of the rotor blade. It modifies the flow at the trailing-edge and brings the separation point closer to the trailing-edge and this results in an increase in the lift over a large range of angles of attack with a small drag penalty ([45], [46]). Studies have shown an increase in drag and pitching moments with increasing lengths ([45], [46], [47]). Hence, Gurney flaps have advantages depending on the application.

Concepts that enhance performance over a wide range of operating conditions are: fixed and dynamic slats, variable droop leading-edge (VDLE) airfoils, circulation control blowing, trailing-edge flaps(TEFs) and leading-edge slats(LESs). These have been considered for active aerodynamic flow control. VDLE airfoils have shown dynamic stall mitigation capability, as discussed in subsequent sections.TEFs and LESs appear attractive for their conceptual simplicity and wide-ranging applicability to minimizing vibratory loads and noise signatures and improving rotor performance.

1.5 Trailing-edge flaps

The advent of complex and lightweight smart-material actuators, which have large stroke and energy density, makes vibration control with TEFs an attractive alternative,especially as the blade-integrated flaps are capable of other functions, in addition to vibration control, while being aeromechanically stable([49]). Flaps on helicopters are not designed for primary control as in aeroplanes. They are designed to act as a secondary control to improve the efficiency of the rotor blade by modifying the lift of the profile and by reducing the vibration of the rotor. However, there has been some interest in using TEFs for primary control in a swashplateless rotor also and hence it would be pertinent to include some observations in this regard.

1.6 Trailing-edge flaps for primary control

Eliminating the swashplate and the associated control system can lead to significant reductions in weight, drag and cost and an improvement of rotor performance.

Kaman used servo flaps since 1947 on K-125,which inspired the work by Ormiston([48]) of the ways to replace the helicopter rotor swashplate and blade pitch control system with on-blade elevon control surfaces for primary flight control . Results indicated that with aeroelastic design for pitch frequencies in the neighbourhood of 2/rev,reasonable elevon control effectiveness may be achieved.

Shen et.al ([49], [50], [51], [52] and [53]) conducted a comprehensive aeroelastic analysis of the effectiveness of trailing-edge flaps for primary control using University of Maryland Advanced Rotorcraft Code(UMARC). The swashplateless rotor was shown to achieve better rotor performance and was overall more stable than the conventional helicopter. Simulations of TEFs performing both primary control and active vibration control were carried out,and it was shown that TEFs are capable of simultaneously trimming the rotor and reducing vibratory hub loads.

Falls et.al continued Shen's pioneering work on TEFs for swashplateless control ([54], [55]). Design was investigated through parametric studies of the TEFs for a conceptual rotor , such as a UH-60A swashplateless variant. Performance analysis of TEFs in helicopter primary control was carried out ([55]) using UMARC. The TEF design features,such as index angle, aerodynamic overhang, chord and length were identified to be important, especially at high speed flight conditions.The swashplateless rotor required less main rotor power than the conventional UH-60A helicopter from hover to μ=0.25.The swashplateless UH-60A was found less efficient than the baseline UH-60A at higher advance ratios([55]).

1.7 TEFs for Vibration Reduction and Performance Enhancement

The trailing-edge flap actuators, hinges and supports are placed within the rotor blade. Deflecting the flaps causes pitching moment changes, which in turn force the blade to pitch about the root bearing, thus controlling the blade pitch.The blade must have a pre-collective (pitch index)larger than the expected trim value, since the

flaps produce an augmentation in lift and hence nose-down pitching moment when deflected downwards. It must also be hinged behind its leading edge(overhang) to reduce hinge moments and hence actuation requirements.

The geometry of the flap includes key design parameters: the outboard spanwise locations experience higher dynamic pressures and hence smaller deflections are required. Also, larger flap length results in smaller deflections; these combine to suggest a location close to 75% R ([56]). Flap chord determines whether it acts primarily as a lift flap or a moment flap. Deflections are smaller for larger flap chord but actuation requirements increase, so a compromise is required here.

A blade-mounted trailing edge flap driven by a piezoelectric actuator, such as in a MD900 light utility helicopter was studied for reduction of vibration and noise and aerodynamic performance improvements ([57]). The active flap system was whirl tower tested to demonstrate its excellent authority.

A review of the state of the art in vibration reduction in rotorcraft using active control is given by Friedmann and Millott ([58]), showing that the actively controlled flap has remarkable potential for vibration reduction.

Koratkar et.al. ([59]) developed a Mach-scaled rotor blade with piezoelectric bender-actuated trailing-edge flaps for vibration control. UMARC was used to determine the optimal flap span,chord and spanwise location of the TEF for this study,which showed upto 90% hub load vibrations were reduced with flap deflections of about $\pm 4^{\circ}$.

TEFs have also been analyzed with great success for active vibration control, notably through numerical simulations performed by Milgram and Chopra

([56], [60])), using an analytical model for helicopter main rotor with plain trailing-edge flaps in compressible flows. The analysis incorporated a nonlinear aeroelastic rotor model and a multicyclic flap controller, and it was validated using experimental wind tunnel data. The trailing-edge flap system was found to be effective in reducing vibration at all advance ratios,but the reduction was not great at low speeds (μ=0.10) and high speeds($\mu \geq 0.35$). The parametric study for Sikorsky S-76 main rotor suggested that a flap with the smallest possible chord and the largest possible deflection is preferred.

Wind tunnel testing of Mach-scaled rotors with active TEFs with each blade controlled independently was performed by Roget and Chopra and the results show that multiple fixed-frame loads can be minimized simultaneously ([61] on a demo aircraft with reduced payload.

Full-scale tests by Eurocopter on the BK-117 ([62]) show that active rotor control can provide considerable reduction of rotor-induced vibration.

Jain et. al,using coupled CFD-CSD simulations, showed that TEFs can improve rotor performance in high-speed forward flight ([63]). The study was on a UH-60A Blackhawk rotor for two key flight conditions in forward flight: high speed and high thrust. It showed that active controls could reduce rotor loads,improve rotor performance and reduce vibrations,by careful selection of operating conditions.

Cheng et al. ([64]) carried out a study using 2/rev inputs on the UH-60A rotor specifically for performance improvement, demonstrating the benefits of lower harmonic inputs to performance.

Yeo ([65]) explored different active control concepts for rotor performance

improvement including TEFs.The study was conducted to assess the capability of active controls to cause rotor performance improvements,using the comprehensive analysis CAMRAD II.The baseline rotor considered was a 4-bladed articulated rotor with a VR-12 airfoil. The study showed that with 2/rev harmonic excitation, TEFs are capable of improving rotor performance.

To exploit the benefits of TEFs and minimize the drag penalties, they need to be actively controlled to address phenomena occurring at multiples of rotor frequency. Different objectives, such as vibration and power reduction, needed different actuation requirements. Fixed-frame vibration is targeted by exciting the flaps at rotor harmonics, so as to generate forces to counteract the ones causing vibrations.For the reduction of N_b/rev fixed frame vibration, the TEF input frequencies used were N_b,$N_b \pm 1$/rev. Power reduction is achieved by the redistribution of the disk loading to make it more uniform and modify blade angle of attack to minimize associated drag penalties.The TEF input frequencies used for this purpose are 1 and 2/rev. Hence, it is inevitable that a compromise must be arrived at between the various benefits of using TEFs.

1.8 Dynamic Stall

Dynamic stall is a critical phenomenon occurring in high-thrust forward flight conditions. The rotor blade sections operate at low dynamic pressures and high angles of attack on the retreating side of the disk. The unsteady flow conditions and proximity to the airfoil stall limit leads to a phenomenon called dynamic stall,

characterized by the production of a leading edge vortex which convects over the upper surface of the airfoil. There is a large increase in the nose-down pitching moment as the vortex convects over the airfoil.The large pitching moment oscillations lead to severe vibratory hub loads and performance penalties. The details of the dynamic stall are available in Ref. ([1]). The schematic is shown in (Fig. 1.2).

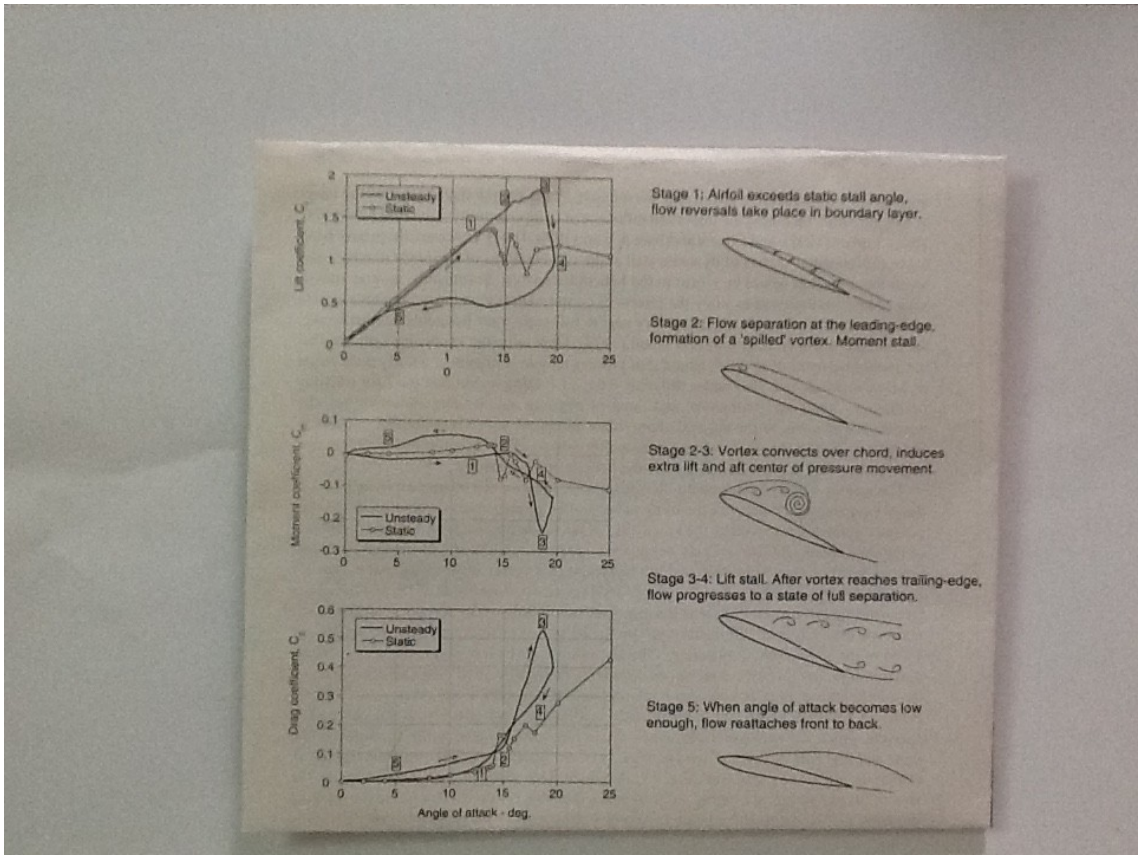

Figure 1.2: Stages of dynamic stall on a helicopter blade

It has been shown ([66]) that under high-speed forward-flight conditions,the surface pressures and the force coefficients indicate that the slat is beneficial in reducing retreating blade dynamic stall. It was found that the slat reduces the torque and pitching moments on the retreating side compared to the baseline. An

approach to combating dynamic stall is to design airfoil sections with improved dynamic characteristics.

Martin et.al.([67]) showed with numerical computations and experimental tests that a Variable Droop Leading Edge (VDLE) airfoil is a feasible concept for application to a rotor high-lift condition. The ability of the VDLE airfoil to control the dynamic stall process was demonstrated. However, the ultimate integration of a VDLE airfoil into a full-scale rotor is likely to pose several challenges. Carr et.al.([71]) conducted wind-tunnel tests on a RC(6)-08 airfoil with 2 different leading-edge slat configurations and showed that slats are capable of suppressing dynamic stall.

Wong ([68]) compared predicted dynamic stall characteristics with experimental data on a VR-7 airfoil with a modified upper surface to obtain better static characteristics. The results showed the minor upper-surface modification led to alleviation of dynamic stall effects.These airfoils are limited to a narrow range of operating conditions.

Another approach involves active control using TEFs or LE Slats, with suitably prescribed inputs to target the retreating blade.

1.9 LESs for vibration reduction and Performance Enhancement

Leading edge slats are high-lift devices, which delay the onset of stall on an airfoil by energizing the airfoil and delaying separation. The use of slats for primary control is expected to be possible, but is likely to be very different from trailing-

edge flaps,because a slat naturally causes nose-up pitch. However, the control of unsteady loads(vibrations) resulting from retreating blade stall in forward flight can be readily addressed by the use of slats.

To explore the benefits of leading-edge slats,we have to keep in mind the fact that the maximum thrust generated by the rotor is limited by blade stall. In high speed forward flight,the reduced dynamic pressures on the retreating blade and phenomenon of dynamic stall lead to loss of thrust.On the other hand, shock-induced flow separation on the advancing blade, which sees transonic flow,imposes a limit on maximum achievable forward speed. Leading edge slats help increase the maximum static lift coefficient of the base airfoil,thus may mitigate the problem of retreating blade stall.

Experimental studies were conducted by McAlister ([69]), on a VR-7 airfoil at fixed angles of attack upto 30° in a water tunnel. The addition of slat was found to delay the static drag and static moment stall. The study showed the slat caused a more gradual advance of trailing-edge separation to occur over the main airfoil section. This translates into a significant improvement in the maximum rotor thrust capability. However, using fixed slats is accompanied by an increased drag penalty especially at low thrust conditions.

Wind tunnel tests conducted by Noonan ([70]), in the Langley Transonic Dynamics Tunnel to evaluate rotor performance using slotted airfoils in the rotor blade tip region. This study tested four rotor configurations and reported benefits at high thrust levels and speeds for the forward-slotted airfoils with $-6°$ slat.

A study was also conducted by Narramore, et al ([73]) using high-lift airfoils

generated by inverse design techniques. Rotor performance using the slotted airfoils was better than the baseline rotor.

Carr et al.([71]) designed a Multi-Element Airfoil(MEA) RC(6)-08 with 2 slat configurations and tested it in the NASA Compressible Dynamic Stall Facility. The results showed the improvements that can be attained through suitable slat design,achieved after comparing the slatted variant with the basic single-element airfoil.The slot is the space between the slat and the blade. Interferograms obtained in the studies indicate that the slat/slot combination continues to energize the flow on the main airfoil through the jet in the slot.

Studies were conducted by Chandrashekhara([72]) through experiments controlling dynamic stall using the Dynamically Deforming Leading-Edge (DDLE) airfoil,the slatted airfoil, the airfoil with zero-mass flux synthetic jet and the Variable Droop Leading Edge (VDLE) airfoils. The conclusion was that the DDLE airfoil, the slatted airoil and the VDLE airfoil demonstrated significant capability to control and delay the onset of compressible dynamic stall. The slatted airfoil was found to use natural blowing through the slat passage to mitigate dynamic stall effects.

Yeo et. al. ([74]) studied analytically the benefits of multi-element forward slotted airfoils for a UH-60A helicopter. Baseline SC1095 and SC1094R8 airfoil characteristics were modified based on CFD calculations of an A3C slotted airfoil to incorporate aerodynamic characteristics of a high-lifting airfoil. The slotted airfoil increased maximum thrust of the UH-60A helicopter by up to 25%, but a significant penalty is observed at $C_T/\sigma < 0.11$. Performance of the slotted airfoil with the wide chord blade showed that the slotted airfoil has limited advantages over the regular

wide chord blade.

Lorber et al.([75]) have made computational and experimental fixed- geometry slat-blade configurations to determine slat positions for maximum lift and minimum drag performance. These Multi-Element Airfoil studies used the optimized A3C slat airfoil shape. Tests conducted on a model rotor fitted with four interchangeable slots showed that the most effective slats significantly improved the rotor stall boundary, but the performance was subdued at low thrusts.An active slat actuation was proposed for improving the slat performance.

Asitav et.al.([76]).carried out a CFD-CSD simulation of the effects of leading-edge slats on rotor performance.For this study of the various slat positions investigated by Lorber et.al. ([75]), two slat positions -S1 and S6- were identified for their low drag and high lift characteristics respectively. A harmonic actuation of the slat that completely retracts it on the advancing side(S1)and completely deploys it in downward position (S6)on the retreating side, minimizes the drag penalty while enhancing the lift capability of the blade([76]). The results indicated that the slatted airfoils are able to perform significantly better than the unslatted baseline. The results indicated that the slatted airfoil is able to achieve higher static lift coefficients compared to the baseline by delaying the onset of boundary layer separation on the main airfoil section. The drop in the pitching moment coefficient is less severe in the presence of a slat. It allows better performance in unsteady conditions. The 4-bladed UH-60A rotor geometry was studied operating in the high-altitude,high thrust flight condition,identified as C9017.It was found from this study that both static and dynamic slat actuations effectively mitigated dynamic stall.

Yeo([77]) compared different active control concepts for rotor performance improvement using the comprehensive analysis CAMRAD-II, including LESs and TEFs, and concluded that leading-edge slats were effective in increasing the blade maximum loading capability.Carefully chosen actuations are capable of reducing rotor hub vibration levels([78]).

1.10 Goal of this research

The overall goal of the present research is flight envelope expansion through the use of active control of the rotor using trailing-edge flaps and leading-edge slats (Fig. 1.3).

It is obvious that one single rotor design cannot achieve all the desired characteristics:

1. Reduction in vibration and noise levels.

2. Increase in blade loading (pushing out the rotor stall boundary).

3. Increase in the maximum flight speed.

Comprehensive rotor analyses are well suited for evaluation of active control concepts through parametric studies to determine configurations that yield maximum benefits as well as understand the mechanisms of their operation. Performance gains with active control surfaces are expected to be largest at high speeds and high thrust levels, where a small redistribution of loading can result in significant reductions.

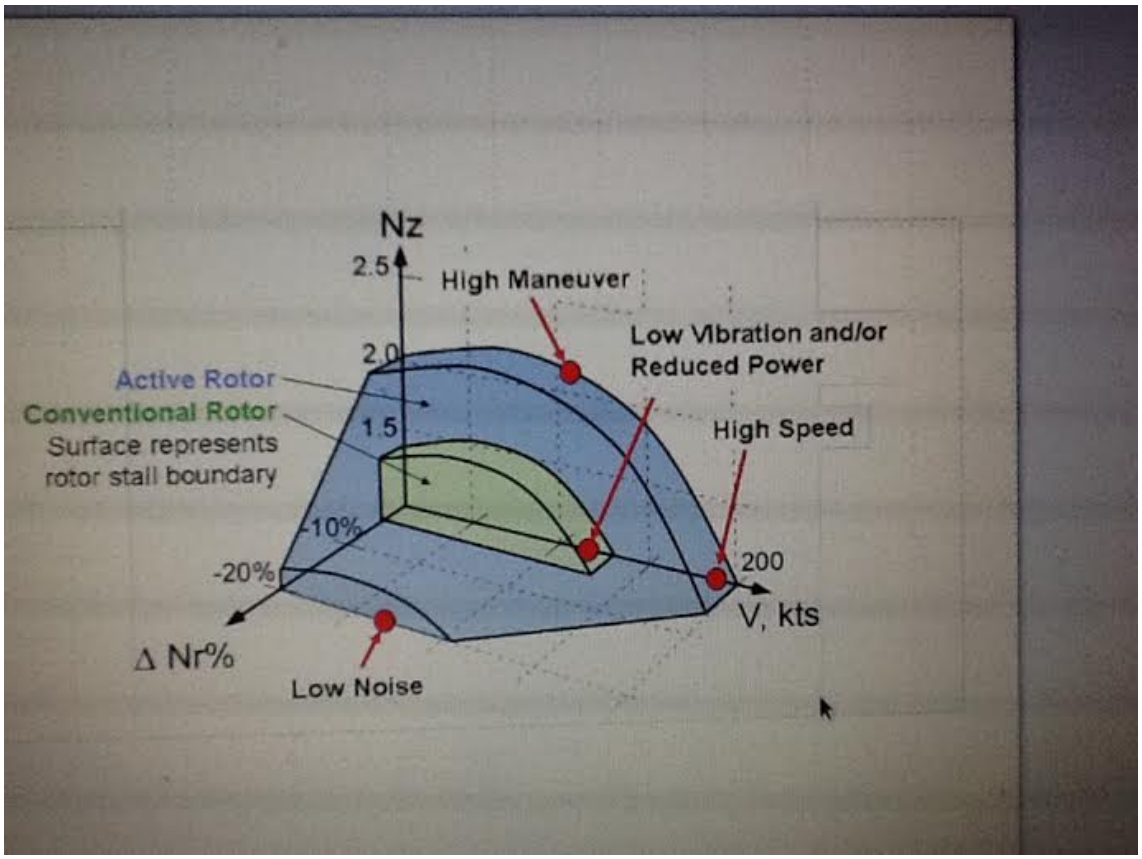

Figure 1.3: Flight envelope

Using trailing-edge flaps and leading-edge slats can allow the designers to tune the rotor for increased performance and/or vibration and noise reduction over a broad range of flight conditions.

1.10.1 Analysis with Trailing-edge flaps

To systematically study the effects of active control with TEFs on performance in terms of power consumption and vibration, first, hover performance is considered. Next, high-speed flight conditions are explored for power reduction using a combination of TEF inputs at different frequencies. Then, the standard high speed, high vibration, moderate thrust flight condition (such as C8534) from the UH-60A airloads program([79]) is explored for vibration reduction.Then, the posssibility of simultaneous power and vibration reduction with TEFs is addressed.

1.10.2 Analysis with Leading-edge slats

Because of the complexities and challenges of slat actuations in a rotating environment, the merits of using active slatted rotor blades need to be examined systematically before the concept can be implemented in blade design. Accordingly, in this study, a comprehenensive analysis has been made to assess and quantify the impact of leading-edge slats on rotor performance, vibratory loads, blade bending and thrust capability for a range of flight conditions.

1.10.3 Analysis of Superimposition of TEFs and LESs

Having developed prediction capability for slatted rotor which shows significant gains in maximum rotor thrust and dynamic stall alleviation with slats, another subject of research that excited interest was to study the superimposition of TEFs and leading-edge slats in an effort to improve the power benefits by alleviating the negative loading on the advancing side.

1.11 Approach

The primary research objective was to analyze,validate and optimize TEFs/LESs for active vibration control and performance enhancement.The tasks identified,to achieve these goals,were:

The University of Maryland Advanced Rotor Code(UMARC) was utilized; the primary focus of the present research was the determination of the operating conditions and the rotor geometry for which the flight envelope could be expanded. The UH-60A rotor geometry and structural properties, as specified by the UH-60A Airloads Program was used as the base geometry for the initial performance analysis. The baseline rotor was the UH-60A,with SC1095 and SC1094R8 airfoils.For the LES studies,the slatted blade sections had the SC2110 baseline/slatted airfoils in place of the baseline UH-60A airfoils:SC1095 and SC1094R8. The structural,inertial and aerodynamic contributions of trailing edge flaps and leading-edge slats were

integrated into the baseline blade analysis in UMARC.

For the TEF/LES studies, the flap is modeled as a single additional degree of freedom while the slat motion is modeled with 3 additional degrees of freedom to improve conformity of the slat airfoil with the blade airfoil and the motion of the flap and slat is prescribed in the analysis. The baseline rotor analysis is a coupled trim procedure that solves the blade equations of motion in time and space(using the finite element method)to obtain the blade response. The response is used to calculate blade and hub loads, which define the necessary control settings for vehicle trim. This process is iterated till the convergence of response and trim(in steady flight). Adding the modeling of flaps and slats to the baseline rotor analysis UMARC was the single most important step of the study: the addition of active rotor surfaces results in incremental inertial and aerodynamic loads which are added to the blade equations of motion with additional degrees of freedom for the flap/slat.

1.11.1 TEF studies

For the TEF studies, UMARC was used to quantify the capabilities of the flaps for helicopter vibration reduction and performance enhancement. UH-60A performance data are computed using UMARC, which has been validated against data from the UH-60 Airloads Project. The TEF used in this model was a 'moment flap', meaning it operates by modifying the section pitching moments and inducing a blade elastic twist in response to the moments. A parameter that directly affects the blade twist,and therefore effectiveness of the TEF, is the torsional stiffness(GJ)

of the blade.

Vibration was studied at various flight speeds,particularly for the C8534 and C9017 flights.

TEFs(span 10% R, 10-15% c, midspan at 65% R) were evaluated for performance improvement in hover, reduction of 4/rev hub vibratory loads and power at the high speed flight condition C8534 and reduction of dynamic stall loads,hub vibratory loads and power at the high thrust forward flight condition C9017. The TEF was shown to be capable of multiple functions,namely vibration reduction, stall alleviation and power reduction,using HPP actuation amplitudes of 5-10°.

The rotor performance in hover was improved with a combination of torsionally softer blades and positive TEF deflections,which contribute to a positive elastic twist response and reduced induced losses. The effect of torsional stiffness is primarily on the blade first torsional mode: the first torsion frequency reduces from $4.3/rev$ for the baseline blade to $3.3/rev$ for the 50% stiff blade.

The rotor performance in high speed forward flight was improved by suitable conbination of steady,$1/rev$ and $2/rev$ TEF inputs to reduce the negative loading on the advancing blade and thus off-load the front and rear parts of the disk. Power reductions of the order of 2% at $\mu = 0.3$ and $4-5\%$ at $\mu = 0.4$ were observed using HPP actuation amplitudes of 5-10°.

Power reductions of the order of $10-20\%$ at various speeds were achieved using dynamic slat actuations combining high-lift and low-drag orientations in a $1/rev$ fashion across azimuth.The maximum slat rotation angle between different orientations was about 10°.

$1/rev$ TEF inputs were prescribed to the slatted rotor to further target the areas of negative loading on the rotor disk. Additional power reductions of about 2% were achieved by this method at the maximum baseline rotor thrust level at μ=0.4.

1.11.2 LES studies

Airfoils with leading-edge slats, by virtue of their higher maximum lift capability, are capable of pushing the rotor maximum lift boundary above its conventional level. Additionally, the dynamic behavior of slatted airfoils,in terms of delaying boundary layer separation from the airfoil surface, is superior to airfoils without slats. Properly modeling this requires refinement and validation of the parameters in the Leishman-Beddoes dynamic stall model(used in UMARC), for slatted airfoils. The current results are obtained without unsteady corrections to the airloads due to airfoil dynamic properties,with the understanding that the improved dynamic properties of slatted airfoils will further enhance the lift obtained here with the assumption of fully attached flow.

The modified UMARC code is used to study the capabilities of leading-edge slats for helicopter performance improvement in moderate to high-speed forward flight.The 3 different slat configurations that were studied include: low drag (S0),high lift (S6), and a compromise between the two extreme cases (S1). Dynamic actuations were chosen to retain the high-lift benefits of the slat while seeking to reduce the profile drag penalties over regions of the disk operating at lower angles of attack

i.e. the advancing side.

The UH-60A rotor lift boundary as predicted by UMARC was compared to the McHugh lift boundary for the nominal rotor speed. The agreement was good at intermediate advance ratios. CFD runs were performed to generate 2D airfoil tables for the baseline SC2110 and two MEA (Multi-Element Airfoil) cases with leading-edge slats at S6 and S1 positions. The slat actuation case studied includes S1 on the advancing side and S6 on the retreating side. The airfoil aerodynamic coefficient predictions were validated for the three positions using the experimental data available from ([75]). The maximum achievable rotor thrust was increased by about $25-30\%$ at advance ratios greater than 0.2 using leading-edge slats.The effects of leading-edge slats extending over 20%,30% and 40% of the blade span on rotor performance and vibratory hub loads were examined.These devices can extend the maximum thrust achievable and reduce power requirements,at the cost of increased vibration. The rotor with leading-edge slats could be trimmed at a maximum forward speed that was about 20 knots greater than the baseline without slats.The maximum achievable thrust is increased by $15-30\%$ at advance ratios greater than 0.2. Power requirements at high blade loading conditions may be reduced by as much as $10-20\%$. Of the configurations investigated,the 20% span slats offered a good compromise between power reduction and vibration minimization.

1.11.3 Studies of superimposition of TEFs and LESs

1/rev TEF actuations of the form $\delta = \delta_{1p}\cos(\psi + \phi_{1p})$ were imposed on the

slatted rotor operating at $\mu = 0.4$, $C_W/\sigma = 0.095$ in an effort to improve the power benefits by alleviating the negative loading on the advancing blade. The increments in section aerodynamic properties due to TEFs were assumed to be generic CFD-generated values obtained for the SC1094R8 airfoil.

Chapter 2: Methodology

The University of Maryland Advanced Rotor Code (UMARC)([80]) was utilised to study the effects of TEFs and leading-edge slats. The blades are modeled as second-order, nonlinear, Euler-Bernoulli beams, capable of undergoing coupled flap,lag,torsion, and axial motion.Each blade was discretized into 20 spanwise beam elements and each element consisted of 15 degrees of freedom. The equations of motion are solved using modal reduction (with 10 coupled rotating modes) and finite element in time with 12 equally-spaced time elements (six nodes per element) to calculate the steady periodic response solution. The structural, inertial and aerodynamic contributions of trailing edge flaps and aerodynamic contributions of leading-edge slats were integrated into the baseline blade analysis in UMARC. The flap is modeled as a single, additional degree of freedom while the slat motion is modeled with 3 additional degrees of freedom to improve conformity of the slat airfoil with the blade airfoil and the motions of the flap and slat are prescribed in the analysis. The lifting-line aerodynamic model incorporates sectional lift, drag, and moment coefficients obtained from C-81 lookup tables for both the main blade and the flapped and slatted sections, a Weissinger-L near wake model, a refined Bagai-Leishman pseudo-implicit free wake model ([81])) with the capability of modeling multiple

free trailers, and Leishman-Beddoes unsteady models for attached flow/dynamic stall([82]).The near-wake model was modified to account for the effect of TEFs and LESs on the blade bound circulation distribution.The coupled blade response and vehicle trim equations are solved simultaneously to obtain the blade deflections and trim control settings.The study uses propulsive free flight trim, except at hover. Vehicle weight and speed are prescribed and the rotor control angles, tail rotor collective and fuselage attitude angles are obtained to maintain force and moment equilibrium about three axes. For hover cases, shaft orientation was fixed and the rotor control angles were obtained to trim the rotor to the specified thrust and zero hub rolling and pitching moments.

2.1 Validation of UMARC and determination of Stall Boundaries

The UH-60A performance data computed using UMARC has been validated ([83])against flight data from the UH-60A Airloads Project. The determination of stall boundary is essential for evaluation of the benefits of TEFs and LESs. UMARC has been further modified to accommodate the effects of TEFs([54]) and leading-edge slats.

The choice of a suitable indicator that can be used to identify the onset of blade stall is unclear. The main objective of this research effort was to analyze the rotor airloads in highly stalled flow conditions to determine a suitable metric that can be used as an indicator for blade stall. As a jump-off point, the McHugh

experimental lift boundary, which gives the thrust limits of the rotor for a range of advance ratios, was used to identify this metric.

UMARC was used to obtain trim solutions for flight conditions near the McHugh's experimental lift boundary for the UH-60A rotor([84]). At these high values of blade loading, the rotor is operating in a highly stalled condition and so, obtaining reliable trim solutions requires good initial guess values. To resolve this issue, the rotor thrust setting was set to a low enough value ($C_T/\sigma = 0.08$ has been explored for a range of advance ratios) at a given advance ratio and progressively increased till it reached the value of the desired lift boundary. At each step, the converged trim control angles from the previously trimmed thrust condition were prescribed as the initial guess for trim. In some conditions like hover where the trim shaft angles are known (to be small), an alternative procedure to determine the lifting limit consists of trimming the rotor to these settings.

Fig. (2.1) shows the comparison of the McHugh lift boundary with the predicted lift boundary using UMARC, as a function of advance ratio. The boundaries agree very well for mid-range advance ratios but the limits predicted by UMARC are slightly lower at low and high advance ratios. Figure (2.2) shows the predicted trim settings for the points on the UMARC lift boundary. The general trends of the trim angles are similar to those due to increase in advance ratio at a constant thrust level. Fig. (2.3) shows the trend of the trim angles for cases of constant blade loading (C_T/σ=0.07-0.1).

The next step is to arrive at a suitable criterion for rotor stall. One possible criterion is to examine the regions over the rotor disk where the blade airfoil is

stalled as per its static stall limits. To this end, the local angle of attack and section pitching moment are plotted across the rotor disk (once trim is achieved), and the regions where static stall is occurring are highlighted. The objective is to determine whether the static stall condition is appropriate to identify rotor stall and, if possible, to seek a parameter which clearly signals the onset of stall and hence places a bound on the thrust level.

The flight condition at μ=0.237 has been explored at a range of thrust levels (C_T/σ=0.09-0.1325, the lifting limit, flight condition C9017). Figures (2.4)-(2.12) show the contour plots of angle of attack, pitching moment coefficient and static stall boundaries for $C_T/\sigma = 0.09$,0.11 and 0.1325. It can be seen that static stall regions exist for thrust levels far below the thrust limit, though they become more significant at higher levels. Some quantities which have identified dynamic stall in the past, under different flight conditions, are the higher harmonic blade root vibratory loads. Figs. (2.13)-(2.20) show these contours for the points on the UMARC-predicted lift boundary at advance ratios of 0, 0.15 and 0.3 .

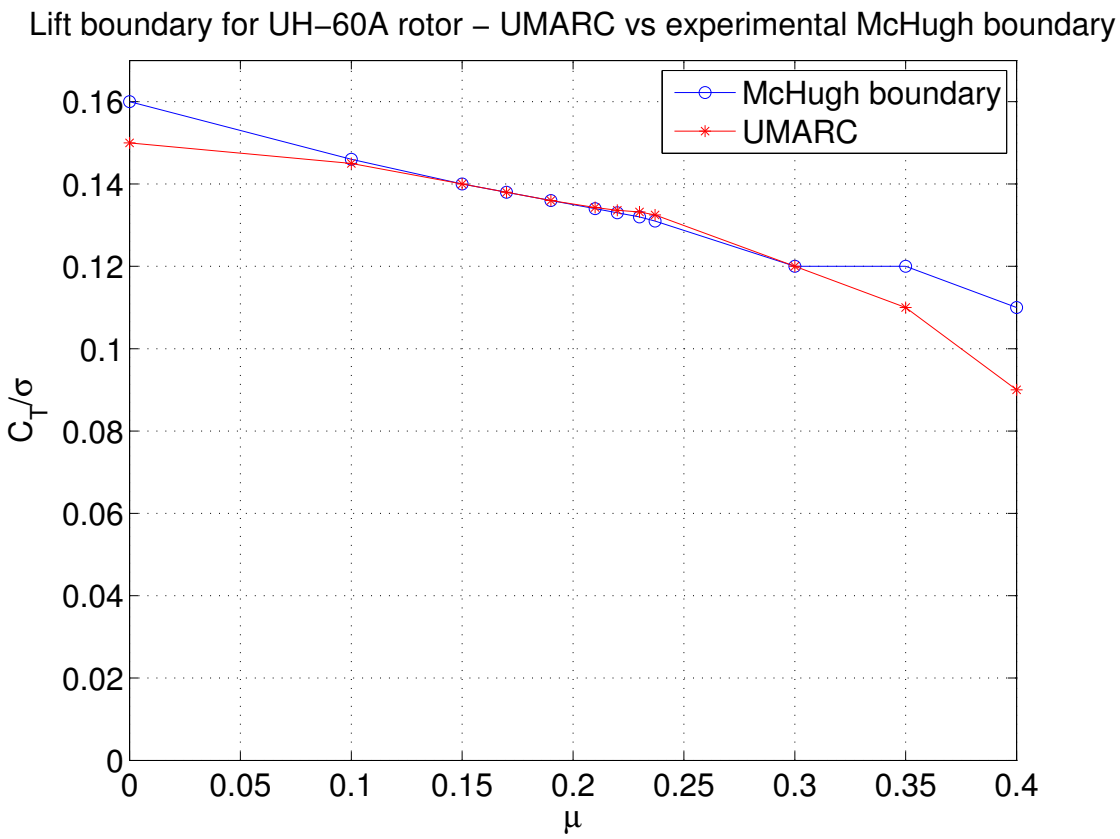

Figure 2.1: Comparison of the McHugh lift boundary with UMARC prediction

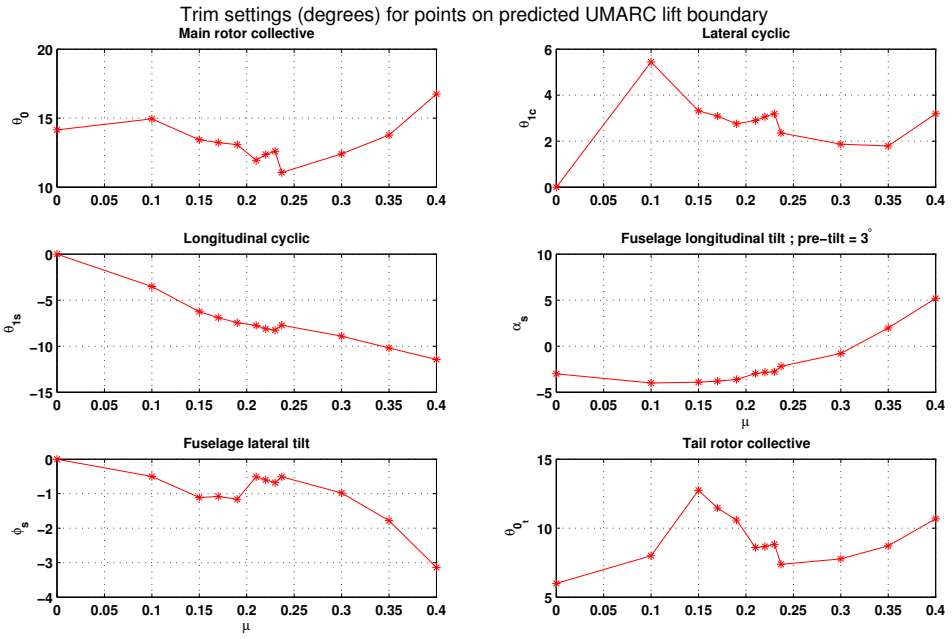

Figure 2.2: Trim settings for points on the predicted UMARC lift boundary

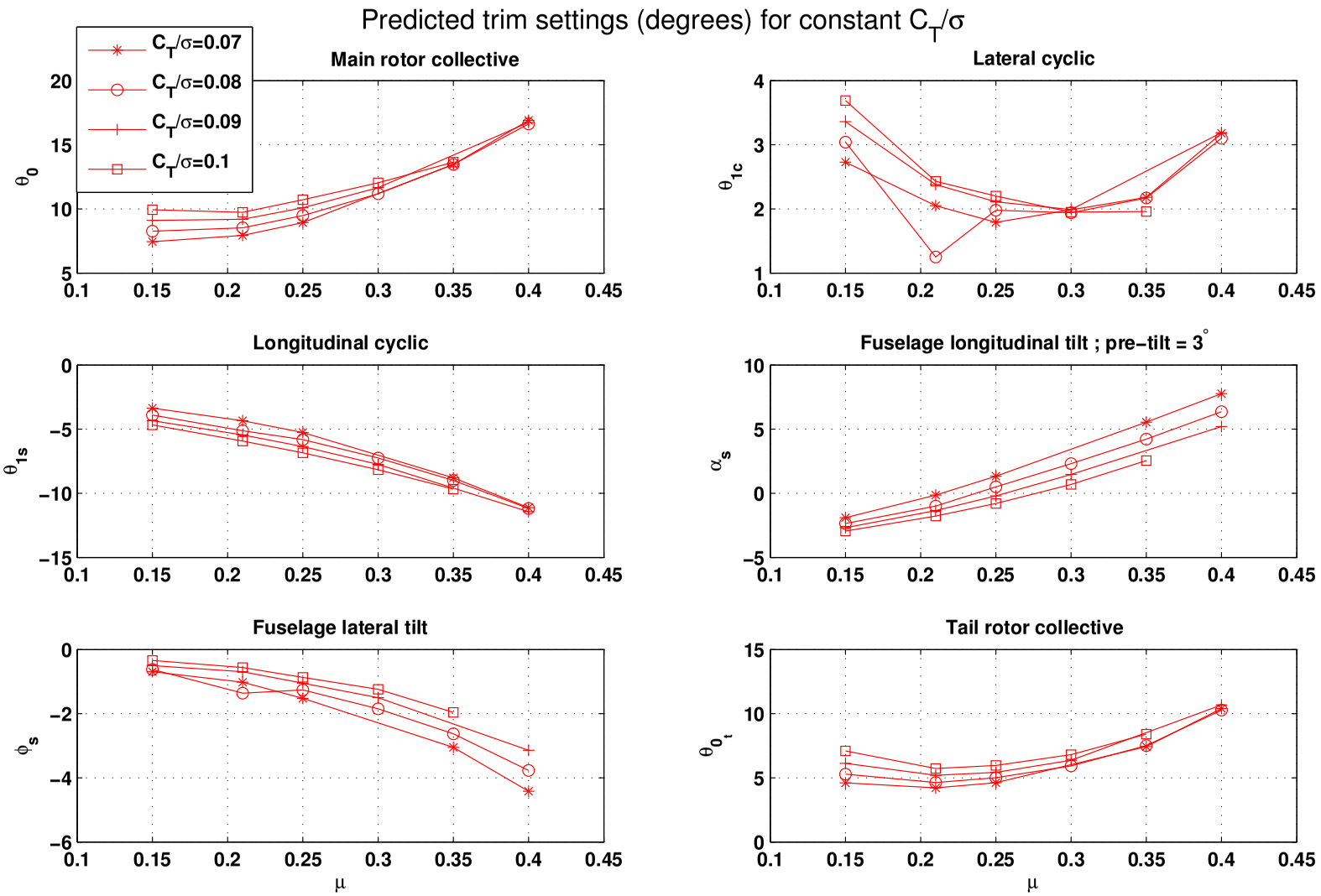
Predicted trim settings (degrees) for constant C_T/σ
C_T/σ=0.07
C_T/σ=0.08
C_T/σ=0.09
C_T/σ=0.1
Main rotor collective
θ_0
Lateral cyclic
θ_{1c}
Longitudinal cyclic
θ_{1s}
Fuselage longitudinal tilt ; pre−tilt = 3°
α_s
Fuselage lateral tilt
ϕ_s
Tail rotor collective
θ_{0_t}
μ
μ

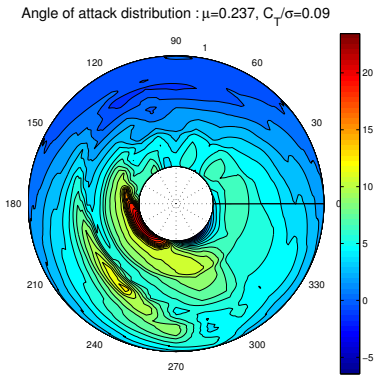

Figure 2.4: Angle of attack distribution for μ=0.237,C_T/σ=0.09

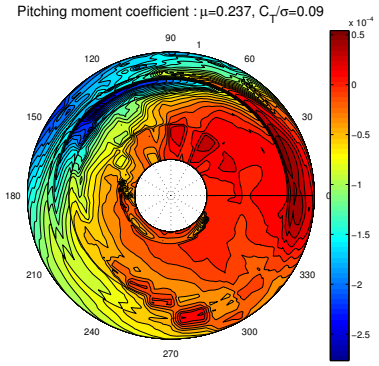

Figure 2.5: Pitching moment distribution for μ=0.237,C_T/σ=0.09

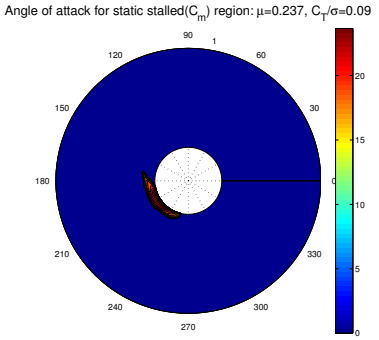

Figure 2.6: Angle of attack for static C_m stall;μ=0.237,C_T/σ=0.09

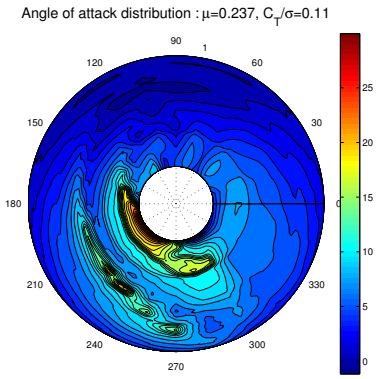

Figure 2.7: Angle of attack distribution for μ=0.237,C_T/σ=0.011

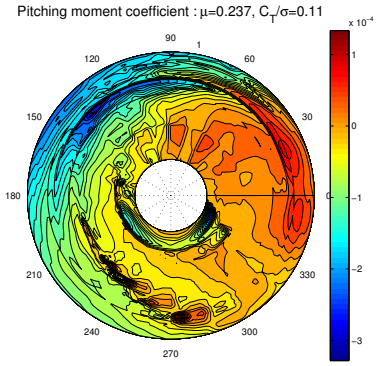

Figure 2.8: Pitching moment distribution for μ=0.237,C_T/σ=0.011

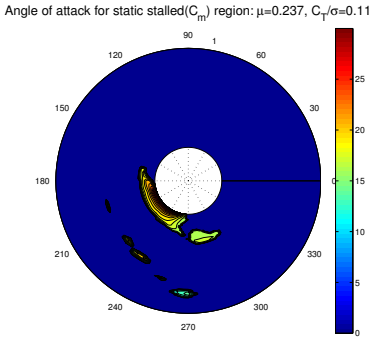

Figure 2.9: Angle of attack for static C_m stall;μ=0.237,C_T/σ=0.011

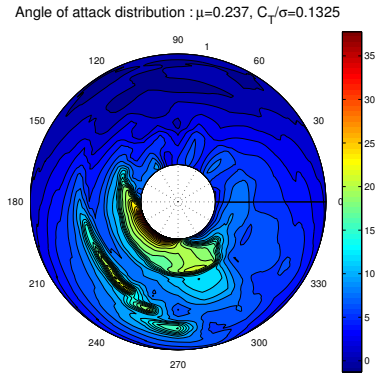

Figure 2.10: Angle of attack distribution for μ=0.237,C$_T/\sigma$=0.1325

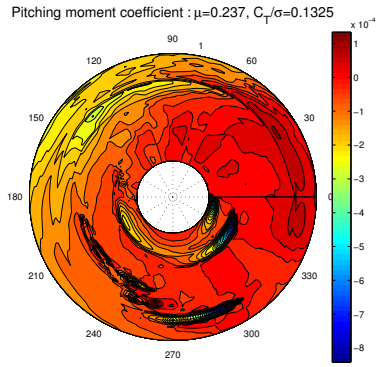

Figure 2.11: Pitching moment distribution for μ=0.237,C$_T/\sigma$=0.1325

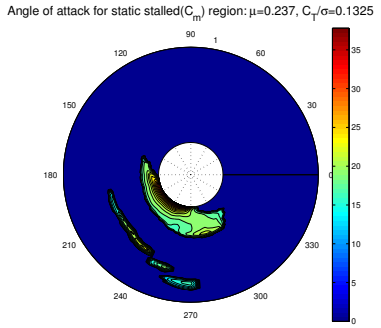

Figure 2.12: Angle of attack for static C_m stall;μ=0.237,C$_T/\sigma$=0.1325

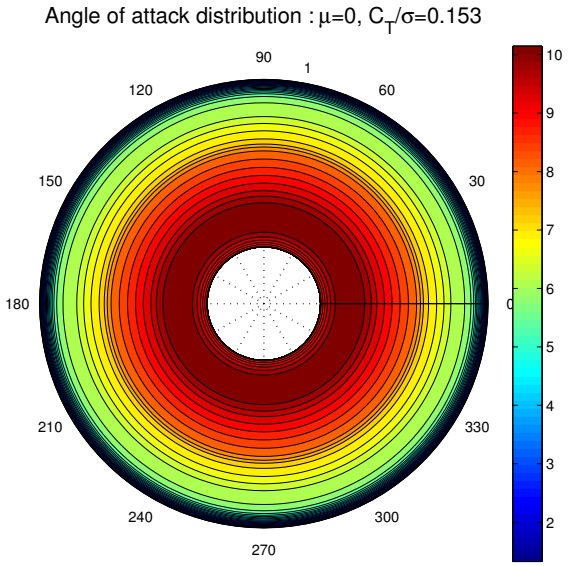

Figure 2.13: Angle of attack distribution for μ=0,C_T/σ=0.153

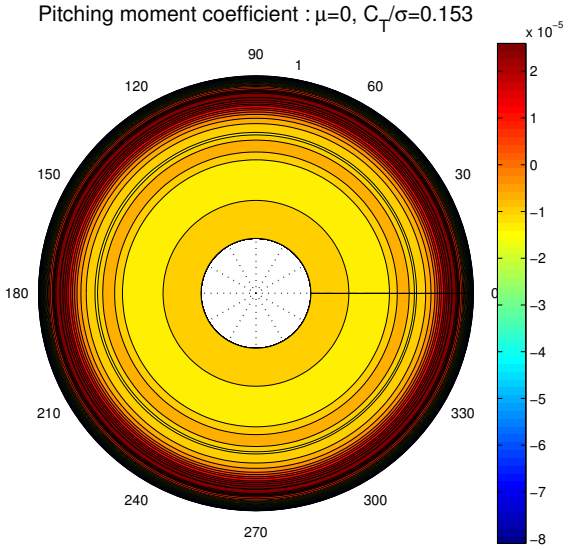

Figure 2.14: Pitching moment distribution for μ=0,C_T/σ=0.153

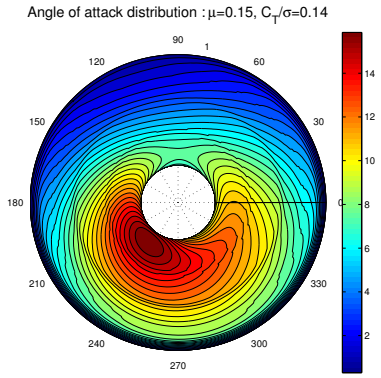

Figure 2.15: Angle of attack distribution for μ=0.15,C$_T/\sigma$=0.14

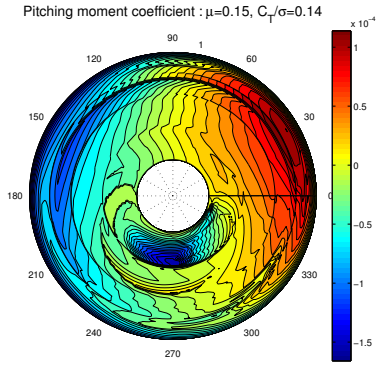

Figure 2.16: Pitching moment distribution for μ=0.15,C$_T/\sigma$=0.14

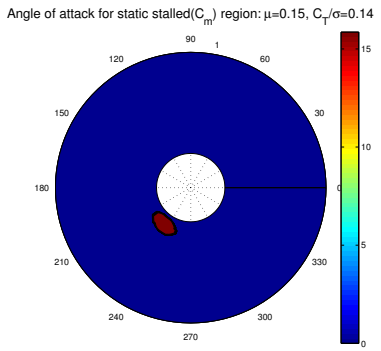

Figure 2.17: Angle of attack for static C_m stall;μ=0.15,C$_T/\sigma$=0.14

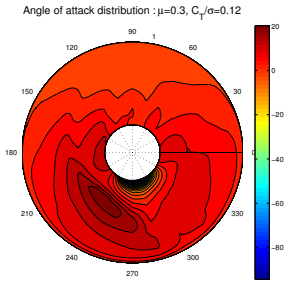

Figure 2.18: Angle of attack distribution for μ=0.3,C_T/σ=0.12

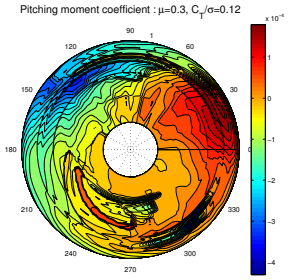

Figure 2.19: Pitching moment distribution for μ=0.15,C_T/σ=0.12

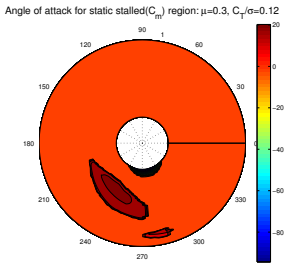

Figure 2.20: Angle of attack for static C_m stall for μ=0.3,C_T/σ=0.12

2.2 Analytical Model:TEFs

Performance gains with active control surfaces are expected to be largest at high speeds and high thrust levels, where a small redistribution of loading can result in significant gains. Parametric sweeps of TEF actuations were carried out to determine suitable combinations of steady, 1/rev and 2/rev TEF inputs that yield overall power reductions. Different combinations of steady plus 2/rev TEF inputs were prescribed, in order to obtain the trends of the actuations that had the best impact on performance.

The basic rotor and flap data, TEF geometry and standard flight conditions used in this study are listed in Table 2.1.The TEF geometry was prescribed based on sizing studies performed at Sikorsky Aircraft per Hoerner ([85]).

2.3 TEF blade section aerodynamic characteristics

The two-dimensional (2D) airfoil characteristics (C_l , C_d , C_m) in the C-81 table look-up format for the TEF sections were generated using an in-house CFD analysis TURNS ([86]) for the baseline SC1094R8 airfoil and for TEF deflections of $\pm 2.5°$, $\pm 5°$, $\pm 10°$, $\pm 15°$ and a range of operational Mach numbers (0.3 to 0.8) and angles of attack (-20° to +20° in steps of 2.5°).The aerodynamic characteristics of the TEF section, at a representative Mach number (with the TEF midspan blade section at 65%R) of 0.5 are shown in the figure[2.21] for the baseline SC1094R8 airfoil and TEF deflections of -5° and 5°. A downward (positive) TEF deflection increases the lift, increases drag at positive angles of attack and decreases drag at negative angles of attack, and increases nose-down pitching moments. Overall, a positive TEF deflection improves section L/D at small angles of attack.

2.4 Multicyclic Controller for TEFs

For the vibration reduction studies, earlier results were obtained by exploring the contours of the vibratory hub loads for a wide range of flap inputs to detect the points of minima. A table of the results (Table . 2.2 and Table . 2.3) for 3, 4 and 5/rev TEF actuations and blade stiffness of (100%GJ) and (75%GJ) for simultaneous reduction of different loads, is given below.

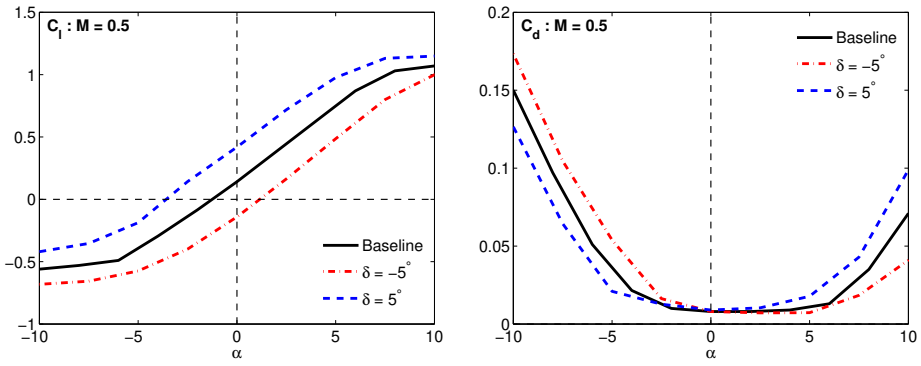

Figure 2.21: 2D CFD-generated airfoil characteristics (SC1094R8) with $-5°$ and $5°$ TEF deflections at M = 0.5

Properties	Value
UH-60A rotor data	
Rotor type	Articulated
Number of blades N_b	4
Radius R	26.83 ft.
Chord c	1.73 ft.(nominal)
Rotor speed Ω	258 RPM
Solidity σ	0.0832
Lock number γ	6.33
Trailing-edge flap data	
Length	$10\%R$
Chord	$15\%c$
Midspan location	$65\%R$
Hinge location	Flap leading-edge
Leading-edge slat data	
Length	$40\%R$
Chord	$15\%c$
Midspan location	$70\%R$
Baseline airfoil	SC2110
Slat orientations	S0,S1,S6

Table 2.1: Basic rotor,flap and slat data

Blade natural frequencies (/rev)

	1	2	3
Flap	1.04	2.84	4.69
Lag	0.28	12.4	-
Torsion	4.3	13.5	-

Flight conditions	
C8534	$\mu = 0.368$, $C_W/\sigma = 0.0783$
C9017	$\mu = 0.237$, $C_W/\sigma = 0.1325$

Open-loop TEF inputs

UNIVERSITY OF MARYLAND

- **3/rev**

Stiffness	Load	TEF Actuation	ΔF_h ((p-p)/2, $4/rev$)
100%	F_{z_h}	$0.44°\cos(3\psi) - 1.41°\sin(3\psi)$	99.9
	M_{x_h}	$1.14°\cos(3\psi) - 2.75°\sin(3\psi)$	99.7
	M_{y_h}	$0.91°\cos(3\psi) - 3.07°\sin(3\psi)$	99.8
	G	$0.1°\cos(3\psi) - 2.1°\sin(3\psi)$	
75%	F_{z_h}	$0.78°\cos(3\psi) - 1.12°\sin(3\psi)$	99.2
	M_{x_h}	$1.19°\cos(3\psi) - 3.20°\sin(3\psi)$	99.9
	M_{y_h}	$0.83°\cos(3\psi) - 3.27°\sin(3\psi)$	99.8
	G	$0.1°\cos(3\psi) - 2.5°\sin(3\psi)$	

- **4/rev**

Stiffness	Load	TEF Actuation	ΔF_h ((p-p)/2, $4/rev$)
100%	F_{z_h}	$0.74°\cos(4\psi) - 0.15°\sin(4\psi)$	99.4
	M_{x_h}	$2.83°\cos(4\psi) + 0.45°\sin(4\psi)$	99.9
	M_{y_h}	$0.45°\cos(4\psi) + 2.67°\sin(4\psi)$	99.5
	G	$0.9°\cos(4\psi) - 0.1°\sin(4\psi)$	
75%	F_{z_h}	$0.73°\cos(4\psi) + 0.06°\sin(4\psi)$	98.9
	M_{x_h}	$2.98°\cos(4\psi) + 0.50°\sin(4\psi)$	99.6
	M_{y_h}	$0.66°\cos(4\psi) + 2.76°\sin(4\psi)$	99.9
	G	$0.8°\cos(4\psi)$	

Table 2.2: $3/rev$ and $4/rev$ TEF actuations for minimization of diferent loads

Open-loop TEF inputs (contd.)

UNIVERSITY OF MARYLAND

- **5/rev**

Stiffness	Load	TEF Actuation	ΔF_h ((p-p)/2, $4/rev$)
100%	F_{z_h}	$0.64^\circ\cos(5\psi) + 0.99^\circ\sin(5\psi)$	99.6
	M_{x_h}	$0.72^\circ\cos(5\psi) + 1.82^\circ\sin(5\psi)$	99.8
	M_{y_h}	$-1.98^\circ\cos(5\psi) - 0.54^\circ\sin(5\psi)$	99.6
	G	$0.5^\circ\cos(5\psi) + 1.0^\circ\sin(5\psi)$	
75%	F_{z_h}	$0.45^\circ\cos(5\psi) + 1.18^\circ\sin(5\psi)$	99.0
	M_{x_h}	$0.75^\circ\cos(5\psi) + 2.12^\circ\sin(5\psi)$	99.9
	M_{y_h}	$-2.41^\circ\cos(5\psi) - 0.72^\circ\sin(5\psi)$	99.7
	G	$0.3^\circ\cos(5\psi) + 1.1^\circ\sin(5\psi)$	

- **Not easy to predict actuations for simultaneous reduction of different loads**
- **Multicyclic control methodology**

Table 2.3: $5/rev$ TEF actuations for minimization of diferent loads

It may be observed that it is not easy to predict actuations for simultaneous reduction of different loads,and so an algorithm for multicyclic control was developed and implemented for use with UMARC to determine the optimal TEF actuation schedule and the flap inputs necessary for vibration reduction.This algorithm is based on a linear, quasi-static representation of the rotor hub vibration response to TEF inputs ([90]).

1. This algorithm estimates the Jacobian for the hub loads with respect to flap inputs and uses this to calculate the inputs for minimizing a vibration objective function that is a suitably weighted combination of the hub loads ([87]).

2. The results from the multicyclic controller are compared to previously reported results to validate the accuracy of the prediction of optimal TEF inputs.

3. Vibration data for reduction of the 3 hub loads F_{z_h},M_{x_h} and M_{y_h} were obtained from the controller.

Validation of multicyclic controller for TEFs

The reductions in the three hub loads from the baseline value and the combination of flap amplitudes found to achieve maximal reduction were compared for the 'Brute Force' method i.e. identification of optimal actuations from the load reduction contours, and the Multicyclic Controller method. It was found that the controller predicts the minima with good accuracy. This means that the linear, quasi-static model of helicopter vibration with respect to trailing-edge flap inputs

([87]), constructed about an operating condition corresponding to a vector of flap inputs and resulting hub loads, is valid.

A scalar vibration objective function J_1 was defined to minimize the target hub loads and, optionally, the TEF deflections.

$$\mathbf{J}_1 = {\mathbf{z}_n}^T W_z \mathbf{z}_n + \theta_n^T W_\theta \theta_n \tag{2.1}$$

Here $\mathbf{z}_n$ is a vector containing the cosine and sine components of the non-dimensional N_b/rev fixed system hub loads F_x, F_y, F_z, M_x and M_y, and $\boldsymbol{\theta}_n$ is a vector containing the harmonics of the flap control inputs at a time step n. The shear and moment hub loads are respectively non-dimensionalized by the quantities $m_0(\Omega R)^2$ and $m_0(\Omega R)^2 R$. For the reduction of N_b/rev hub loads, the flap actuations consist of $(N_b - 1, N_b, N_b + 1)$/rev components. The matrices W_z and W_θ contain weighting functions for the vibration harmonics and control inputs respectively. Choosing the weights suitably enables targeting specific loads and using specific input flap harmonics.

The system vibration response $\mathbf{z}_n$ is linearized about the current control state using the sensitivity matrix T calculated once at the uncontrolled operating condition using a forward difference method.

$$\mathbf{z}_n = \mathbf{z}_{n-1} + T(\boldsymbol{\theta}_{n-1} - \boldsymbol{\theta}_n) \tag{2.2}$$

Minimizing J_1 by solving $\partial J / \partial \boldsymbol{\theta}_n = 0$ yields the algorithm for updating the control input vector $\boldsymbol{\theta}_n$

$$\boldsymbol{\Delta\theta}_n = C\mathbf{z}_{n-1} - C_\theta \boldsymbol{\theta}_{n-1} \tag{2.3}$$

In Eq. 2.3,

$$\begin{aligned} C &= -DT^T W_z \\ C_\theta &= DW_\theta \\ D &= (T^T W_z T + W_\theta)^{-1} \end{aligned} \tag{2.4}$$

In the present study, the diagonal weighting matrix W_z was assumed to have the form

$$W_z = (1-\beta) \begin{bmatrix} \epsilon/F_{x0}^2 & & & & & \\ & \epsilon/F_{y0}^2 & & & & \\ & & 1/F_{z0}^2 & & & \\ & & & 1/M_{x0}^2 & & \\ & & & & 1/M_{y0}^2 & \end{bmatrix} \tag{2.5}$$

$$W_\theta = \beta I \tag{2.6}$$

In the present study, $\beta = 0$ was used, so the controller attempts to minimize the hub loads without constraining the amplitude of the flap motion.

The reductions in target hub loads,using the TEF multicyclic controller,at the flight condition C8534,for the blade torsional stiffness of 100%,75%,60% and 50%,are given in Table . 2.4 and Table . 2.5 . The TEF optimal actuations are graphically

shown in Fig.2.22.The reduction of the target hub loads,at various advance ratios,for forward flight $C_W/\sigma = 0.08$,is shown in Table.2.6.

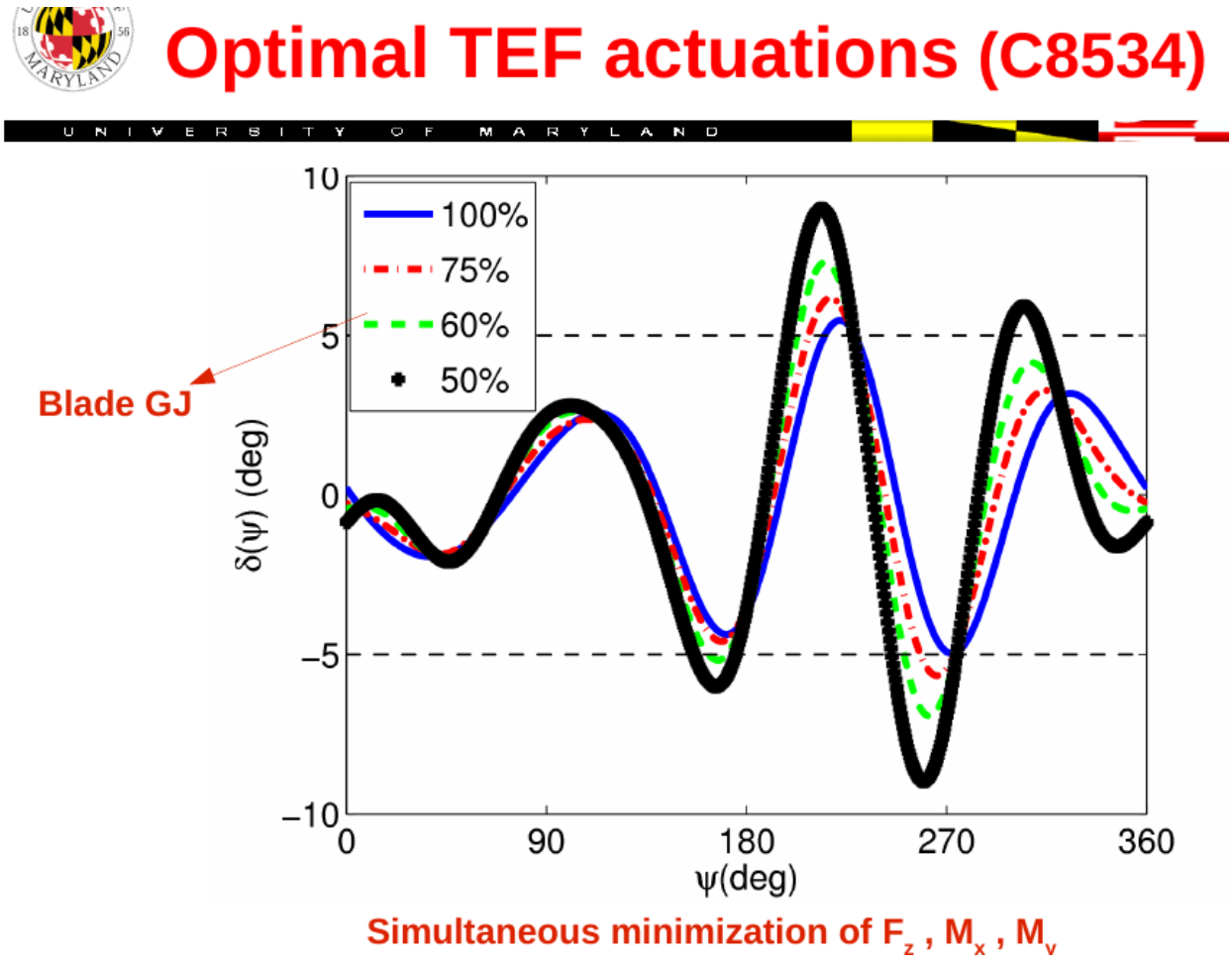

Figure 2.22: Multicyclic control of three hub forces for optimal TEF actuations for various GJ: C8534

Multicyclic Controller – results (C8534)

UNIVERSITY OF MARYLAND

- Multicyclic control for minimization of 4/rev vibratory loads

Load	TEF Actuation
F_{z_h}	$0.28^\circ\sin(3\psi - 46.47^\circ) + 0.18^\circ\sin(4\psi + 59.04^\circ) + 0.13^\circ\cos(5\psi)$
M_{x_h}	$2.87^\circ\sin(3\psi - 23.17^\circ) + 1.62^\circ\sin(4\psi - 83.62^\circ) + 0.66^\circ\sin(5\psi - 8.75^\circ)$
M_{y_h}	$0.61^\circ\sin(3\psi + 78.7^\circ) + 1.54^\circ\sin(4\psi - 12.41^\circ) + 1.03^\circ\sin(5\psi + 14.04^\circ)$
J	$3.31^\circ\sin(3\psi - 30.52^\circ) + 1.69^\circ\sin(4\psi - 82.16^\circ) + 0.35^\circ\sin(5\psi + 39.17^\circ)$

- % reductions in Fz, Mx, My for above cases

Target load(s)

Load	ΔF_h ((p-p)/2, $4/rev$)		
	F_{z_h}	M_{x_h}	M_{y_h}
F_{z_h}	**99.4**	19.8	6.9
M_{x_h}	94.9	**99.9**	63.1
M_{y_h}	-450	-56.8	**99.7**
J	**98.5**	**99.7**	**99.6**

Table 2.4: Multicyclic control for minimization of $4/rev$ vibratory loads:C8534

- **Variation of blade GJ : minimization of J (defined to minimize 4/rev hub F_z, M_x, M_y)**

Torsional Stiffness	TEF Actuation
100%	$3.32^\circ\sin(3\psi - 30.7^\circ) + 1.78^\circ\sin(4\psi - 80.9^\circ) + 0.41^\circ\sin(5\psi + 42.4^\circ)$
75%	$3.24^\circ\sin(3\psi - 15.9^\circ) + 2.18^\circ\sin(4\psi - 57.9^\circ) + 0.86^\circ\sin(5\psi + 55.4^\circ)$
60%	$3.51^\circ\sin(3\psi - 6.5^\circ) + 2.8^\circ\sin(4\psi - 43.8^\circ) + 1.28^\circ\sin(5\psi + 60.2^\circ)$
50%	$3.91^\circ\sin(3\psi + 4.0^\circ) + 3.81^\circ\sin(4\psi - 35.7^\circ) + 1.83^\circ\sin(5\psi + 63.4^\circ)$

- **% reductions in 4/rev hub loads for above cases**

Torsional Stiffness	% reduction from baseline					(p-p)/2 deflection (°)
	F_{x_h}	F_{y_h}	F_{z_h}	M_{x_h}	M_{y_h}	
100%	14.3	53.2	98.0	99.1	99.4	5.22
75%	20.4	78.9	98.0	94.2	99.1	5.92
60%	25.9	79.9	92.2	95.6	99.2	7.12
50%	34.1	77.7	93.6	99.0	98.3	8.98

Table 2.5: Multicyclic control for minimization of J:C8534

- **100% GJ : minimization of *J* (defined to minimize 4/rev hub F_z, M_x, M_y)**
- **Forward flight : C_W/σ=0.08**

Advance ratio (μ)	% reduction from baseline					(p-p)/2 deflection (°)
	F_{x_h}	F_{y_h}	F_{z_h}	M_{x_h}	M_{y_h}	
0.15	72.0	78.2	97.5	98.0	97.7	2.23
0.21	67.6	53.6	99.8	99.2	98.9	2.33
0.25	33.8	63.2	99.3	98.7	99.0	2.14
0.3	5.5	66.2	97.9	98.6	99.7	3.25
0.368 (C8534)	14.3	53.2	98.0	99.1	99.4	5.22

Table 2.6: Multicyclic control for minimization of J: $C_W/\sigma = 0.08$,at various forward flight speeds

2.5 Analytical Model: LES

2.5.1 Leading-edge slat structural model

Previously, the slat motion was modeled as a combination of 2 prescribed rotations (see Fig. 2.23), one about the blade elastic center (denoted by χ_b) and the other about its hinge (denoted by χ_s). The separation R_s was assumed constant. The local (deformed blade) coordinate system is centred at the blade elastic center and the coordinate directions are along $\{\mathbf{i}_\xi, \mathbf{j}_\eta, \mathbf{k}_\zeta\}$. The local slat coordinate system is defined by $\{\mathbf{i_s}, \mathbf{j_s}, \mathbf{k_s}\}$, centred at the slat hinge.

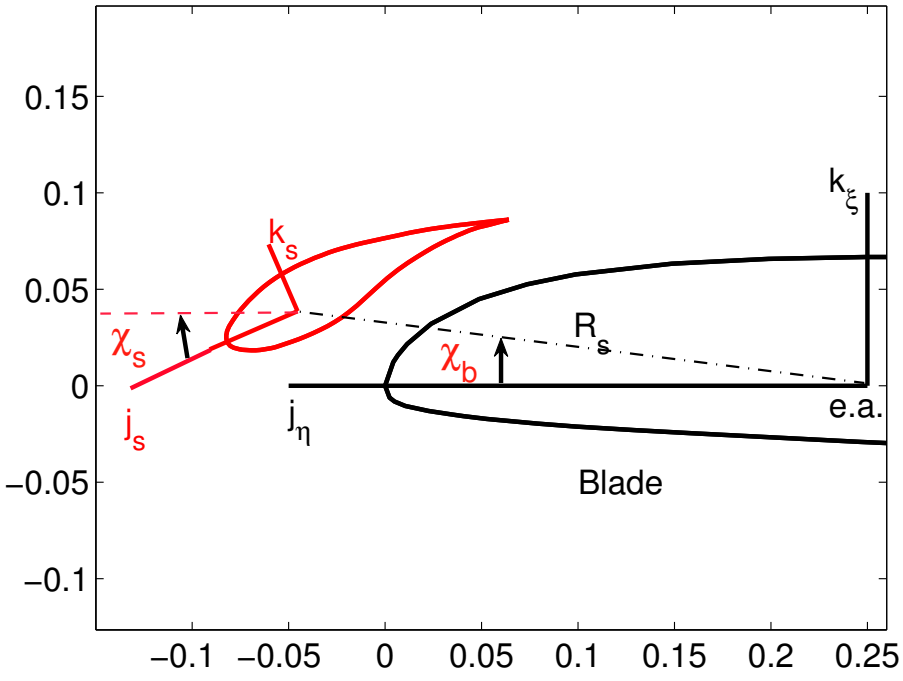

Figure 2.23: 2 degree-of-freedom slat model

The fidelity of the model with respect to the experimental slat positions S1-S6 as described in [75] was investigated using suitable combinations of χ_b and χ_s. While it is possible to approximate to some extent the translation-rotation of the slat by means of 2 rotations, it was determined that a more accurate description of the actual motion of the slat will require an additional degree of freedom.

To this end, a 3 degree-of-freedom model has been developed, the 3 degrees being the 2 coordinates of the slat hinge (denoted by η_h and ζ_h), and the rotation of the slat about the hinge (χ_s), maintaining the length of the strut connecting the slat to the hinge (R_s) and the angle between the strut and the slat local axes (χ_0) constant.(Fig. 2.24). The attached animations illustrate that the new model captures any given actuation schedule corresponding to the experimental setup, exactly.

Also,in Fig.2.25,both the 2 and 3 DOF models of the slat motion are given to illustrate the differences.

From the data corresponding to the experimental setup, the following characteristics were extracted (note that lengths are non-dimensionalized with respect to the baseline blade chord, taken to be $24''$) :

1. Baseline blade airfoil SC2110; slat airfoil supplied was designed for constant area flow between slat and baseline blade

2. For attachment to the quarter-chord position of the slat section, $R_s = 0.075$;

3. Coordinates of the experimental hinge positions in the blade coordinates ($\mathbf{j}_\eta, \mathbf{k}_\zeta$) : S1 = (0.21,0.06) ; S6 = (0.23,0.04)

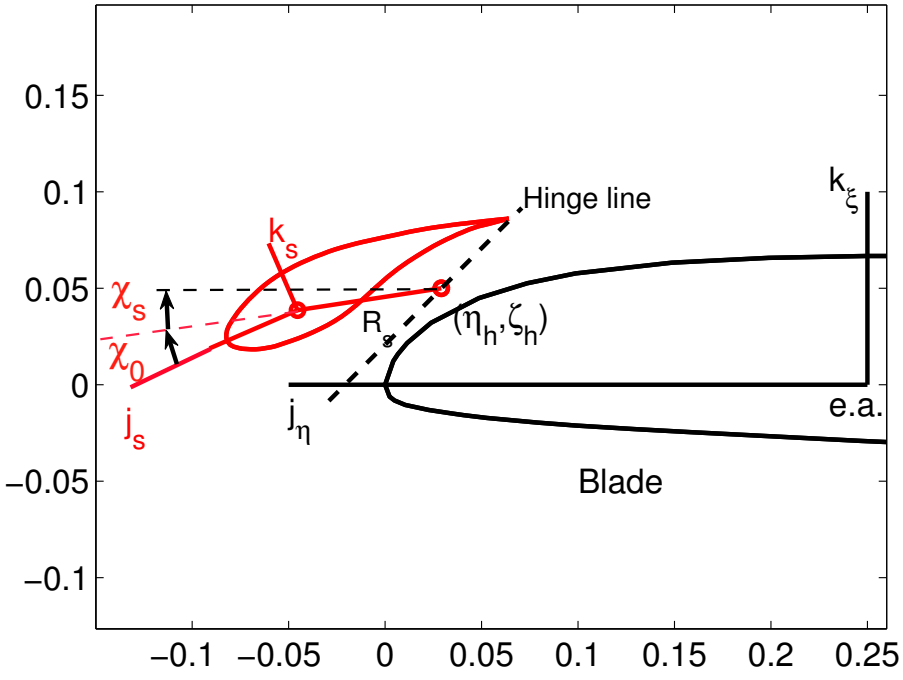

Figure 2.24: 3 degree-of-freedom slat model

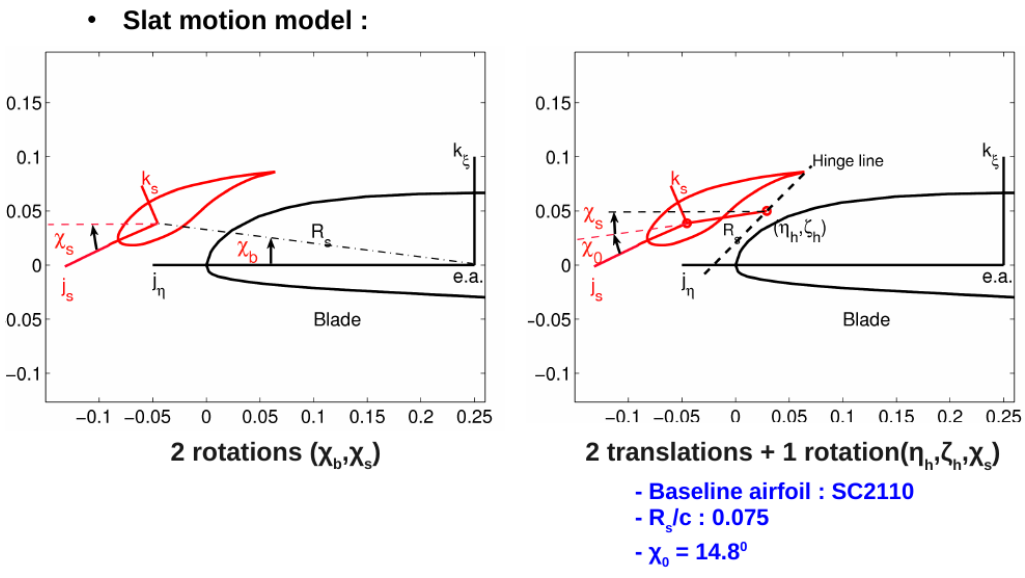

Figure 2.25: 2 and 3 degrees of freedom slat models

4. Angle between slat local axes and strut , $\chi_0 = 14.76°$

Enhancements were made to the baseline blade analysis in the University of Maryland Advanced Rotor Code (UMARC) for the integration of the complete structural, inertial and aerodynamic contributions of leading-edge slats to model its' benefits.The slat airfoil is modeled as an additional element on the baseline blade(same geometry as the UH-60A blade). The slat motion is modeled with 3 additional degrees of freedom to improve conformity of the slat airfoil with the blade airfoil and to capture the experimental translation-rotation actuation methodology.The quasi-steady aerodynamic effects are being modeled using 2D table lookup for section aerodynamic coefficients as a function of angle of atttack,Mach number and slat orientation.

The inertial contributions of the leading-edge slat to the baseline blade equations of motion have been formulated and incorporated in the finite-element model in UMARC, with 3 additional global degrees of freedom.

The aerodynamic forces in the presence of the slat are calculated by an airfoil table-lookup process, with section aerodynamic coefficients obtained from 2-D CFD analysis for different blade angles of attack, local Mach number and slat position. The motion of the slat is from S1 on the advancing blade to S6 on the retreating blade in a $1/rev$ fashion, i.e.

- $\eta_h(\psi) = \eta_{S1} + d(\psi)/\sqrt{2}$
- $\zeta_h(\psi) = \zeta_{S1} + d(\psi)/\sqrt{2}$
- $\chi_s(\psi) = \theta(\psi)$

where the hinge distance from S1 on the hinge line S1-S6 (negative toward S6) is given by

$$d(\psi) = -0.32'' + 0.32'' sin(\psi)$$

normalized with respect to the blade chord; and the rotation of the slat from the blade axis is given by

$$\theta(\psi) = -23.75^{\circ} + 3.75^{\circ} sin(\psi)$$

The slat geometry used in this study and the definition of 'effective chord' are shown in Fig. 2.26 and Fig. 2.27.

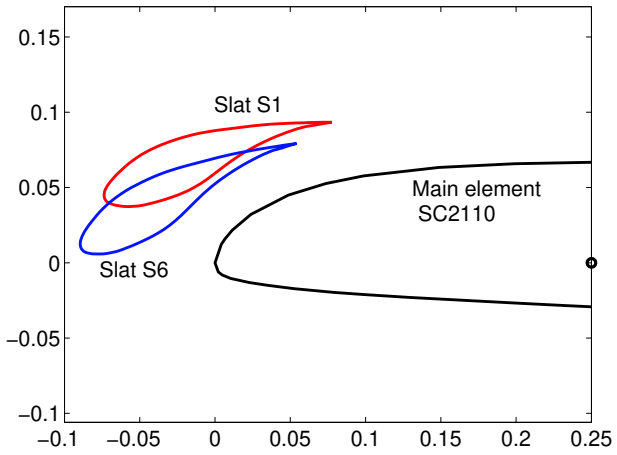

Figure 2.26: Slat configurations with respect to baseline airfoil

2.5.2 Description of slat motion

The equations of motion governing the slat are given below.The final equations of motion governing the extension, torsion and the slat motion can be obtained using

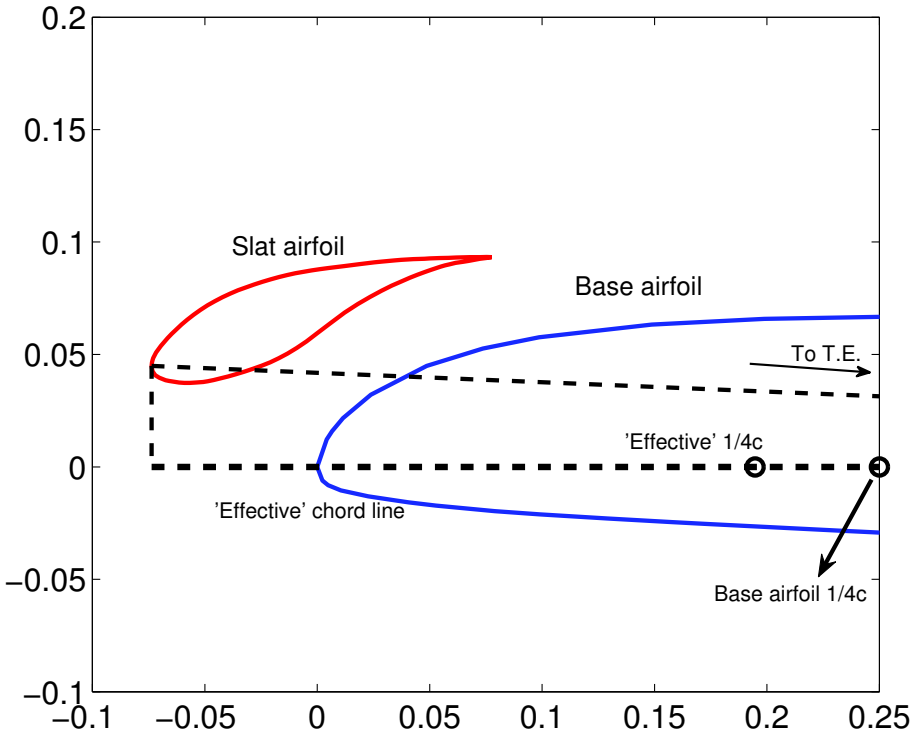

Figure 2.27: Definition of 'effective' chord

the expression for Hamilton's Variational Principle and the equations for the contributions from the slat and blade(and/or TEF and work done by external forces).

As shown in Fig. 2.28, the slat motion is modeled as a combination of 2 prescribed rotations, one about the blade elastic center (denoted by χ_b) and the other about its hinge (denoted by χ_s). The separation R_s is assumed constant. The local (deformed blade) coordinate system is centred at the blade elastic center and the coordinate directions are along $\{\mathbf{i}_\xi, \mathbf{j}_\eta, \mathbf{k}_\zeta\}$. The local slat coordinate system is defined by $\{\mathbf{i_s}, \mathbf{j_s}, \mathbf{k_s}\}$, centred at the slat hinge.

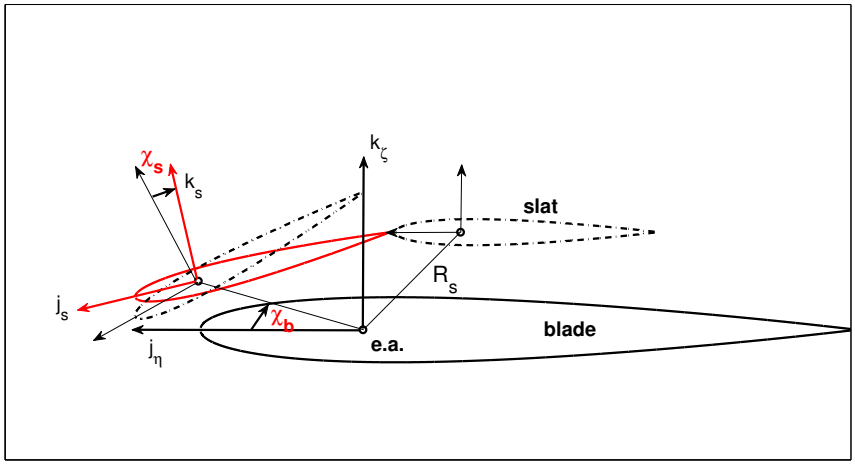

Figure 2.28: Definition of slat degrees of freedom

2.5.3 Hamilton's principle

The finite element energy expressions for the elastic model are derived using the generalized Hamilton's principle, given as :

$$\int_{t_1}^{t_2} (\delta U - \delta T - \delta W) dt = 0 \tag{2.7}$$

where δU, δT and δW are the virtual work contributions of conservative forces (variation of potential energy), inertial forces (variation of kinetic energy) and non-conservative forces. In the following sections, the incremental contributions of the slat to the total energy are given, without ignoring any terms based on ordering schemes.

2.5.4 Strain Energy

(a)Section properties

Slat section properties

$$\eta_1 = \eta_s cos\chi_s + R_s cos\chi_b$$

$$\zeta_1 = \eta_s sin\chi_s + R_s sin\chi_b$$

$$\int\int_s d\eta d\zeta = A_s$$

$$\int\int_s \eta_s d\eta d\zeta = A_s e^a_{As}$$

$$\int\int_s \zeta_s d\eta d\zeta = 0$$

$$\int\int_s \eta_s^2 d\eta d\zeta = I^a_{Zs}$$

$$\int\int_s \zeta_s^2 d\eta d\zeta = 0$$

$$\int\int_s (\eta_s^2 + \zeta_s^2)^2 d\eta d\zeta = B^a_{1s}$$

$$\int\int_s \eta_s (\eta_s^2 + \zeta_s^2)^2 d\eta d\zeta = B^a_{2s}$$

Derived slat section properties

$$\int\int_s \eta_1 d\eta d\zeta = A_s e_{As}$$
$$\int\int_s \zeta_1 d\eta d\zeta = A_s d_{As}$$
$$\int\int_s \eta_1^2 d\eta d\zeta = I_{Zs}$$
$$\int\int_s \zeta_1^2 d\eta d\zeta = I_{Ys}$$
$$\int\int_s (\eta_1^2 + \zeta_1^2) d\eta d\zeta = I_{Ys} + I_{Zs} = A_s k_{As}^2$$
$$\int\int_s (\eta_1^2 + \zeta_1^2)^2 d\eta d\zeta = B_{1s}$$
$$\int\int_s \eta_1 (\eta_1^2 + \zeta_1^2)^2 d\eta d\zeta = B_{2s}$$
$$\int\int_s \zeta_1 (\eta_1^2 + \zeta_1^2)^2 d\eta d\zeta = B_{3s}$$
$$\int\int_s \eta_1 (\eta_1^2 + \zeta_1^2) d\eta d\zeta = D_{1s}$$
$$\int\int_s \zeta_1 (\eta_1^2 + \zeta_1^2) d\eta d\zeta = D_{2s}$$

(b)Expression for strain energy The potential energy for the rotor is the sum of blade and slat contributions.

$$\delta U = \delta U_b + \delta U_s$$

The contribution of the deformation of the blade itself to δU_s is given by

$$\int_s \int\int (E_x \epsilon_{xx} \delta\epsilon_{xx} + G\epsilon_{x\eta} \delta\epsilon_{x\eta} + G\epsilon_{x\zeta} \delta\epsilon_{x\zeta}) d\eta d\zeta dx$$

where the integration is carried out over the slat spanwise limits.

In addition, the slat motions themselves give rise to

$$\Delta\delta U_s = k_{\chi_b}\chi_b\delta\chi_b + k_{\chi_s}\chi_s\delta\chi_s$$

where k_{χ_b}, k_{χ_s} are the equivalent springs located at the origins of the slat motions, i.e. the blade elastic center and the slat hinge. Thus

$$\begin{aligned}\delta\overline{U_s} = \frac{\delta U_s}{m_0\Omega^2R^3} = \int_s (&U_{u'_e}\delta u'_e + U_{v'}\delta v' + U_{w'}\delta w' + U_{v''}\delta v'' + U_{w''}\delta w'' \\ &+U_{\hat{\phi}}\delta\hat{\phi} + U_{\hat{\phi}'}\delta\hat{\phi}' + U_{\hat{\phi}''}\delta\hat{\phi}'' + U_{\chi_b}\delta\chi_b + U_{\chi_s}\delta\chi_s)dx\end{aligned} \tag{2.8}$$

(c)Slat contributions

$$\begin{aligned}U_{u'_e} = \quad & EA_s[u'_e + k_{As}^2(\theta'\hat{\phi}' + \theta'w'v'' + \tfrac{\hat{\phi}'^2}{2} + \tfrac{w'^2v''^2}{2} + \hat{\phi}'w'v'')] \\ & -EA_se_{As}[v''(cos\theta - \hat{\phi}sin\theta) + w''(sin\theta + \hat{\phi}cos\theta)] \\ & -EA_sd_{As}[w''(cos\theta - \hat{\phi}sin\theta) - v''(sin\theta + \hat{\phi}cos\theta)]\end{aligned}$$

$$U_{v'} = 0$$

$$U_{w'} = GJ_s(\hat{\phi}'v'' + w'v''^2) + EA_s[k_{As}^2(\theta'v''u'_e + \hat{\phi}'v''u'_e + u'_e w'v''^2)$$

$$-(\theta'v''^2 + \hat{\phi}'v''^2 + w'v''^3)\{e_{As}(cos\theta - \hat{\phi}sin\theta) + d_{As}(sin\theta + \hat{\phi}cos\theta)\}$$

$$-(\theta'v''w'' + \hat{\phi}'v''w'' + w'v''^2w'')\{d_{As}(cos\theta - \hat{\phi}sin\theta) + e_{As}(sin\theta + \hat{\phi}cos\theta)\}$$

$$+EB_{1s}(\theta'^2\hat{\phi}'v'' + \tfrac{3}{2}\theta'\hat{\phi}'^2v'' + 2\theta'\hat{\phi}'w'v''^2 + 2\theta'^2w'v''^2 + \tfrac{3}{2}\theta'w'^2v''^3 +$$

$$\tfrac{1}{2}\hat{\phi}'^3v'' + \tfrac{3}{2}\hat{\phi}'^2w'v''^2 + \theta'\hat{\phi}'w'v''^2 + \tfrac{3}{2}\hat{\phi}'w'^2v''^3 + \tfrac{1}{2}w'^3v''^4)$$

$$U_{v''} = GJ_s(\hat{\phi}'w' + v''w'^2) + EA_s[u'_e\{-e_{As}(cos\theta - \hat{\phi}sin\theta) + d_{As}(sin\theta + \hat{\phi}cos\theta)\}]$$

$$+v''\{EI_{Zs}cos^2\theta_1 + EI_{Ys}sin^2\theta_1 - 2EI_{ZYs}cos\theta_1 sin\theta_1\}$$

$$+w''\{(EI_{Zs} - EI_{Ys})cos\theta_1 sin\theta_1 + EI_{ZYs}cos2\theta_1\}$$

$$+[sin\theta(EB_{3s} - \hat{\phi}EB_{2s}) + cos\theta(\hat{\phi}EB_{3s} - EB_{2s})](\theta'\hat{\phi}' + \theta'w'v'' + \tfrac{\hat{\phi}'^2}{2} + \tfrac{w'^2v''^2}{2} + \hat{\phi}'w'v'')$$

$$U_{w''} = -EA_s[u'_e\{d_{As}(cos\theta - \hat{\phi}sin\theta) + e_{As}(sin\theta + \hat{\phi}cos\theta)\}]$$

$$w''\{EI_{Zs}sin^2\theta_1 + EI_{Ys}cos^2\theta_1 + 2EI_{ZYs}cos\theta_1 sin\theta_1\}$$

$$+v''\{(EI_{Zs} - EI_{Ys})cos\theta_1 sin\theta_1 + EI_{ZYs}cos2\theta_1\}$$

$$-[sin\theta(EB_{2s} - \hat{\phi}EB_{3s}) + cos\theta(\hat{\phi}EB_{2s} + EB_{3s})](\theta'\hat{\phi}' + \theta'w'v'' + \tfrac{\hat{\phi}'^2}{2} + \tfrac{w'^2v''^2}{2} + \hat{\phi}'w'v'')$$

$$
\begin{aligned}
U_{\phi} = \quad & EA_s u'_e[v''\{d_{As}(cos\theta - \hat{\phi}sin\theta) + e_{As}(sin\theta + \hat{\phi}cos\theta)\} \\
& -w''\{e_{As}(cos\theta - \hat{\phi}sin\theta) - d_{As}(sin\theta + \hat{\phi}cos\theta)\}] \\
& +E(\theta'\hat{\phi}' + \theta' w' v'' + \tfrac{\hat{\phi}'^2}{2} + \tfrac{w'^2 v''^2}{2} + \hat{\phi}' w' v'')[(v''sin\theta_1 - w''cos\theta_1)D_{1s} \\
& +(v''cos\theta_1 + w''sin\theta_1)D_{2s}] \\
& +w''^2[(EI_{Zs} - EI_{Ys})cos\theta_1 sin\theta_1 + EI_{ZYs}cos2\theta_1] \\
& -v''^2[(EI_{Zs} - EI_{Ys})cos\theta_1 sin\theta_1 + EI_{ZYs}cos2\theta_1] \\
& +v''w''[(EI_{Zs} - EI_{Ys})cos2\theta_1 - 2EI_{ZYs}sin2\theta_1]
\end{aligned}
$$

$$
\begin{aligned}
U_{\phi'} = \quad & GJ_s(\hat{\phi}' + w'v'') + EA_s k_{As}^2(\theta' + \hat{\phi}' + w'v'')u'_e \\
& +EB_{1s}(\theta'^2\hat{\phi}' + \theta'^2 w'v'' + \tfrac{3}{2}\theta'\hat{\phi}'^2 + 3\theta'\hat{\phi}'w'v'' + \tfrac{3}{2}\theta' w'^2 v''^2 + \tfrac{1}{2}\hat{\phi}'^3 \\
& +\tfrac{3}{2}\hat{\phi}'^2 w'v''^2 + \tfrac{3}{2}\hat{\phi}' w'^2 v''^2 + \tfrac{1}{2}w'^3 v''^3) \\
& -EB_{2s}(\theta' + \hat{\phi}' + w'v'')\{v''(cos\theta - \hat{\phi}sin\theta) + w''(sin\theta + \hat{\phi}cos\theta)\} \\
& +EB_{3s}(\theta' + \hat{\phi}' + w'v'')\{v''(sin\theta + \hat{\phi}cos\theta) + w''(cos\theta - \hat{\phi})\}
\end{aligned}
$$

$$
U_{\phi''} = 0
$$

$$U_{\chi_b} = k_{\chi_b}\chi_b + GA_sR_se^a_{As}sin(\chi_s-\chi_b)(\hat{\phi}'^2+\hat{\phi}'w'v''+w'^2v''^2)$$

$$+EA_su'_e[v''(R_s\{sin\chi_bcos\theta_1+cos\chi_bsin\theta_1\})-w''(R_s\{cos\chi_bcos\theta_1-sin\chi_bsin\theta_1\})$$

$$-2R_se^a_{As}sin(\chi_b-\chi_s)(\theta'\hat{\phi}'+\theta'w'v''+\tfrac{\hat{\phi}'^2}{2}+\tfrac{w'^2v''^2}{2}+\hat{\phi}'w'v'')]$$

$$+w''^2[EA_sR_s^2sin(\chi_b+\theta_1)cos(\chi_b+\theta_1)+EA_sR_se^a_{As}cos(\chi_b+\theta_1)sin(\chi_s+\theta_1)]$$

$$-v''^2[EA_sR_s^2sin(\chi_b+\theta_1)cos(\chi_b+\theta_1)+EA_sR_se^a_{As}sin(\chi_b+\theta_1)cos(\chi_s+\theta_1)]$$

$$+v''w''[EA_sR_s^2cos2(\chi_b+\theta_1)+EA_sR_se^a_{As}cos(\chi_b+\chi_s+2\theta_1)]$$

$$+2E(\theta'\hat{\phi}'+\theta'w'v''+\tfrac{\hat{\phi}'^2}{2}+\tfrac{w'^2v''^2}{2}+\hat{\phi}'w'v'')[\{v''cos(\chi_b+\theta_1)$$

$$+w''sin(\chi_b+\theta_1)\}A_sR_s^2e^a_{As}sin(\chi_b-\chi_s)$$

$$+\{v''cos(\chi_s+\theta_1)+w''sin(\chi_s+\theta_1)\}R_sI^a_{Zs}sin(\chi_b-\chi_s)]$$

$$+E[\{R_s^3A_s+A_sR_sI^a_{Zs}+2A_sR_s^2e^a_{As}cos(\chi_b-\chi_s)\}$$

$$(\theta'\hat{\phi}'+\theta'w'v''+\tfrac{\hat{\phi}'^2}{2}+\tfrac{w'^2v''^2}{2}+\hat{\phi}'w'v'')\{v''sin(\chi_b+\theta_1)-w''cos(\chi_b+\theta_1)\}$$

$$-2\{R_s^3A_se^a_{As}+R_s\textstyle\int\int_s\eta_s^3d\eta d\zeta+2R_s^2I^a_{Zs}cos(\chi_b-\chi_s)\}sin(\chi_b-\chi_s)$$

$$(\theta'\hat{\phi}'+\theta'w'v''+\tfrac{\hat{\phi}'^2}{2}+\tfrac{w'^2v''^2}{2}+\hat{\phi}'w'v'')^2]$$

$$
\begin{aligned}
U_{\chi_s} = \quad & k_{\chi_s}\chi_s + GA_sR_se^a_{As}sin(\chi_b-\chi_s)(\hat{\phi}'^2+\hat{\phi}'w'v''+w'^2v''^2) \\
& +EA_su'_e[v''(e^a_{As}\{sin\chi_scos\theta_1+cos\chi_ssin\theta_1\})-w''(e^a_{As}\{cos\chi_scos\theta_1-sin\chi_ssin\theta_1\}) \\
& -2R_se^a_{As}sin(\chi_b-\chi_s)(\theta'\hat{\phi}'+\theta'w'v''+\tfrac{\hat{\phi}'^2}{2}+\tfrac{w'^2v''^2}{2}+\hat{\phi}'w'v'')] \\
& +w''^2[EA_sR_se^a_{As}sin(\chi_b+\theta_1)cos(\chi_s+\theta_1)+EI^a_{Zs}cos(\chi_s+\theta_1)sin(\chi_s+\theta_1)] \\
& -v''^2[EA_sR_se^a_{As}sin(\chi_s+\theta_1)cos(\chi_b+\theta_1)+EI^a_{Zs}sin(\chi_s+\theta_1)cos(\chi_s+\theta_1)] \\
& +v''w''[EA_sR_se^a_{As}cos(\chi_b+\chi_s+\theta_1)+EI^a_{Zs}cos2(\chi_s+\theta_1)] \\
& -2E(\theta'\hat{\phi}'+\theta'w'v''+\tfrac{\hat{\phi}'^2}{2}+\tfrac{w'^2v''^2}{2}+\hat{\phi}'w'v'')[\{v''cos(\chi_b+\theta_1) \\
& +w''sin(\chi_b+\theta_1)\}A_sR_s^2e^a_{As}sin(\chi_b-\chi_s) \\
& +\{v''cos(\chi_s+\theta_1)+w''sin(\chi_s+\theta_1)\}R_sI^a_{Zs}sin(\chi_b-\chi_s)] \\
& +E[\{R_s^2A_se^a_{As}+\textstyle\int\int_s\eta_s^3d\eta d\zeta+2R_sI^a_{Zs}cos(\chi_b-\chi_s)\} \\
& (\theta'\hat{\phi}'+\theta'w'v''+\tfrac{\hat{\phi}'^2}{2}+\tfrac{w'^2v''^2}{2}+\hat{\phi}'w'v'')\{v''sin(\chi_s+\theta_1)-w''cos(\chi_s+\theta_1)\} \\
& +2\{R_s^3A_se^a_{As}+R_s\textstyle\int\int_s\eta_s^3d\eta d\zeta+2R_s^2I^a_{Zs}cos(\chi_b-\chi_s)\}sin(\chi_b-\chi_s) \\
& (\theta'\hat{\phi}'+\theta'w'v''+\tfrac{\hat{\phi}'^2}{2}+\tfrac{w'^2v''^2}{2}+\hat{\phi}'w'v'')^2]
\end{aligned}
$$

2.5.5 Kinetic Energy

(a) Section properties

Slat section properties

$$\int\int_s \rho d\eta d\zeta = m_s$$
$$\int\int_s \rho\eta_s d\eta d\zeta = m_s e_s^a$$
$$\int\int_s \rho\zeta_s d\eta d\zeta = 0$$
$$\int\int_s \rho\eta_s^2 d\eta d\zeta = I_{Zs}^a$$

Derived slat section properties

$$\int\int_s \rho\eta_1 d\eta d\zeta = m_s e_s \qquad \int\int_s \rho\zeta_1 d\eta d\zeta = m_s d_s$$
$$\int\int_s \rho\eta_1^2 d\eta d\zeta = m_s k_{m2s}^2 \qquad \int\int_s \rho\zeta_1^2 d\eta d\zeta = m_s k_{m1s}^2$$
$$\int\int_s \rho(\eta_1^2+\zeta_1^2) d\eta d\zeta = m_s k_{ms}^2 \qquad \int\int_s \rho\eta_1\zeta_1 d\eta d\zeta = m_s k_{m3s}^2$$
$$\int\int_s \rho\dot{\eta}_1 d\eta d\zeta = m_s \dot{e}_s \qquad \int\int_s \rho\dot{\zeta}_1 d\eta d\zeta = m_s \dot{d}_s$$
$$\int\int_s \rho\ddot{\eta}_1 d\eta d\zeta = m_s \ddot{e}_s \qquad \int\int_s \rho\ddot{\zeta}_1 d\eta d\zeta = m_s \ddot{d}_s$$
$$\int\int_s \rho\eta_s\eta_1 d\eta d\zeta = m_s e_{s\eta}^2 \qquad \int\int_s \rho\eta_s\zeta_1 d\eta d\zeta = m_s d_{s\eta}^2$$
$$\int\int_s \rho\eta_s\dot{\eta}_1 d\eta d\zeta = m_s \dot{e}_{s\eta}^2 \qquad \int\int_s \rho\eta_s\dot{\zeta}_1 d\eta d\zeta = m_s \dot{d}_{s\eta}^2$$
$$\int\int_s \rho\eta_s\ddot{\eta}_1 d\eta d\zeta = m_s \ddot{e}_{s\eta}^2 \qquad \int\int_s \rho\eta_s\ddot{\zeta}_1 d\eta d\zeta = m_s \ddot{d}_{s\eta}^2$$
$$\int\int_s \rho\zeta_1\dot{\eta}_1 d\eta d\zeta = m_s k_{m4s}^2 \qquad \int\int_s \rho\eta_1\dot{\zeta}_1 d\eta d\zeta = m_s k_{m5s}^2$$
$$\int\int_s \rho\eta_1\dot{\eta}_1 d\eta d\zeta = m_s k_{m6s}^2 \qquad \int\int_s \rho\zeta_1\dot{\zeta}_1 d\eta d\zeta = m_s k_{m7s}^2$$
$$\int\int_s \rho\zeta_1\ddot{\eta}_1 d\eta d\zeta = m_s k_{m8s}^2 \qquad \int\int_s \rho\eta_1\ddot{\zeta}_1 d\eta d\zeta = m_s k_{m9s}^2$$
$$\int\int_s \rho\eta_1\ddot{\eta}_1 d\eta d\zeta = m_s k_{m10s}^2 \qquad \int\int_s \rho\zeta_1\dot{\zeta}_1 d\eta d\zeta = m_s k_{m11s}^2$$

(b)Expression for kinetic energy The potential energy for the rotor is the

sum of blade and slat contributions.

$$\delta T = \delta T_b + \delta T_s$$

where

$$\delta T_s = \int_s \rho \mathbf{v_s}.\delta \mathbf{v_s} d\eta_s d\zeta_s dx$$

where the integration is carried out over the slat spanwise limits. Thus

$$\delta\overline{T_s} = \frac{\delta T_s}{m_0 \Omega^2 R^3} = \int_{x_i}^{x_f} (T_{u_e}\delta u_e + T_v \delta v + T_w \delta w + T_{v'}\delta v' + T_{w'}\delta w' + T_{\hat{\phi}}\delta\hat{\phi} + T_{\chi_b}\delta\chi_b + T_{\chi_s}\delta\chi_s)dx \tag{2.9}$$

(c)Slat contributions

$$\begin{aligned} T_{u_e} = \quad & m_s[x + (-(\beta_p + 2\dot{\theta})e_s - 2\dot{d}_s)sin\theta + (-(\beta_p + 2\dot{\theta})d_s - 2\dot{e}_s)cos\theta \\ & -\tfrac{1}{2}\textstyle\int_0^x (v'^2 + w'^2)dx + \int_0^x (\dot{v}'^2 + v'\ddot{v}' + \dot{w}'^2 + w'\ddot{w}')dx \\ & + u_e - \ddot{u}_e + 2\dot{v} - w\beta_p + v'\{\langle d_s(1+\dot{\theta}^2) - 2\dot{e}_s\dot{\theta} - e_s\ddot{\theta} - \ddot{d}_s\rangle sin\theta \\ & + \langle -e_s(1+\dot{\theta}^2) - 2\dot{d}_s\dot{\theta} - d_s\ddot{\theta} + \ddot{d}_s\rangle cos\theta\} + 2\dot{v}'\{\langle -e_s\dot{\theta} - \dot{d}_s\rangle sin\theta + \langle -d_s\dot{\theta} + \dot{e}_s\rangle cos\theta\} \\ & + \ddot{v}'\{e_s cos\theta - d_s sin\theta\} + w'\{\langle -e_s(1+\dot{\theta}^2) - 2\dot{d}_s\dot{\theta} - d_s\ddot{\theta} + \ddot{e}_s\rangle sin\theta \\ & + \langle -d_s(1+\dot{\theta}^2) + 2\dot{e}_s\dot{\theta} + e_s\ddot{\theta} + \ddot{d}_s\rangle cos\theta\} + 2\dot{w}'\{\langle -d_s\dot{\theta} + \dot{e}_s\rangle sin\theta + \langle e_s\dot{\theta} + \dot{d}_s\rangle cos\theta\} \\ & + \ddot{w}'\{e_s sin\theta + d_s cos\theta\} + \hat{\phi}\{\langle -e_s\beta_p - 2e_s\dot{\theta} - 2\dot{d}_s\rangle cos\theta + \langle d_s\beta_p + 2d_s\dot{\theta} - 2\dot{e}_s\rangle sin\theta\} \\ & + 2\dot{\hat{\phi}}\{-d_s cos\theta - e_s sin\theta] \end{aligned}$$

$$
\begin{aligned}
T_v = \quad & m_s[2\textstyle\int_0^x (v'\dot{v}' + w'\dot{w}')dx + \{-d_s(1+\dot{\theta}^2+2\beta_p\dot{\theta}) + 2(\beta_p+\dot{\theta})\dot{e}_s + e_s\ddot{\theta} + \ddot{d}_s\}sin\theta \\
& + \{e_s(1+\dot{\theta}^2+2\beta_p\dot{\theta}) + 2(\beta_p+\dot{\theta})\dot{d}_s + d_s\ddot{\theta} - \ddot{e}_s\}cos\theta \\
& -2\dot{u}_e + v - \ddot{v} + 2\dot{w}\beta_p + v'\{-2\langle e_s\dot{\theta} + \dot{d}_s\rangle sin\theta + 2\langle -2d_s\dot{\theta} + \dot{e}_s\rangle cos\theta\} \\
& + \dot{v}'\{-2d_s sin\theta + 2e_s cos\theta\} + w'\{2\langle -2d_s\dot{\theta} + \dot{e}_s\rangle sin\theta + 2\langle e_s\dot{\theta} + \dot{d}_s\rangle cos\theta\} \\
& + \dot{w}'\{2e_s sin\theta + 2d_s cos\theta\} + \hat{\phi}\{\langle -d_s(1+\dot{\theta}^2+2\beta_p\dot{\theta}) + 2(\beta_p+\dot{\theta})\dot{e}_s + e_s\ddot{\theta} + \ddot{d}_s\rangle cos\theta \\
& - \langle e_s(1+\dot{\theta}^2+2\beta_p\dot{\theta}) + 2(\beta_p+\dot{\theta})\dot{d}_s + d_s\ddot{\theta} - \ddot{e}_s\rangle sin\theta\} \\
& + \dot{\hat{\phi}}\{2\langle e_s(\beta_p+\dot{\theta}) + \dot{d}_s\rangle cos\theta + 2\langle -d_s(\beta_p+\dot{\theta}) + \dot{e}_s\rangle sin\theta\} \\
& + \ddot{\hat{\phi}}\{e_s sin\theta + d_s cos\theta\}]
\end{aligned}
$$

$$
\begin{aligned}
T_{v'} = \quad & m_s[(e_s cos\theta - d_s sin\theta)\{\tfrac{1}{2}\textstyle\int_0^x (v'^2 + w'^2)dx - x - \int_0^x (\dot{v'}^2 + v'\ddot{v'} + \dot{w'}^2 + w'\ddot{w'})dx\} \\
& + sin\theta cos\theta\{(k_{m2s}^2 - k_{m1s}^2)(\beta_p + \dot{\theta}) + 2(k_{m4s}^2 + k_{m5s}^2)\} \\
& + cos^2\theta\{2(\beta_p + 2\dot{\theta})k_{m3s}^2 + 2(k_{m7s}^2 - k_{m6s}^2)\} - ((\beta_p + 2\dot{\theta})k_{m3s}^2 + 2k_{m7s}^2) \\
& + u_e\{d_s sin\theta - e_s cos\theta\} + \ddot{u_e}\{-d_s sin\theta + e_s cos\theta\} + 2\dot{v}\{d_s sin\theta - e_s cos\theta\} \\
& + w\beta_p\{-d_s sin\theta + e_s cos\theta\} \\
& + v'\{cos\theta sin\theta\langle -2k_{m3s}^2(1 + \dot{\theta}^2) \\
& - 2(k_{m7s}^2 - k_{m6s}^2)\dot{\theta} + (k_{m2s}^2 - k_{m1s}^2)\ddot{\theta} + (k_{m8s}^2 + k_{m9s}^2)\rangle \\
& + cos^2\theta\langle (1 + \dot{\theta}^2)(k_{m2s}^2 - k_{m1s}^2) + 2(k_{m4s}^2 + k_{m5s}^2)\dot{\theta} + 2k_{m3s}^2\ddot{\theta} + (k_{m11s}^2 - k_{m10s}^2)\rangle \\
& + \langle (1 + \dot{\theta}^2)k_{m1s}^2 - 2k_{m4s}^2\dot{\theta} - k_{m3s}^2\ddot{\theta} - k_{m10s}^2\rangle\} \\
& + \dot{v'}\{2cos\theta sin\theta\langle (k_{m2s}^2 - k_{m1s}^2)\dot{\theta} + (k_{m4s}^2 + k_{m5s}^2)\rangle \\
& + 2cos^2\theta\langle 2k_{m3s}^2\dot{\theta} + (k_{m7s}^2 - k_{m6s}^2)\rangle - 2\langle k_{m3s}^2\dot{\theta} + k_{m7s}^2\rangle \\
& + \ddot{v'}\{2cos\theta sin\theta k_{m3s}^2 - cos^2\theta(k_{m2s}^2 - k_{m1s}^2) - k_{m1s}^2\} \\
& + w'\{cos\theta sin\theta\langle (k_{m2s}^2 - k_{m1s}^2)(1 + \dot{\theta}^2) + 2(k_{m4s}^2 + k_{m5s}^2)\dot{\theta} \\
& + 2k_{m3s}^2\ddot{\theta} + (k_{m11s}^2 - k_{m10s}^2)\rangle \\
& + cos^2\theta\langle 2(1 + \dot{\theta}^2)k_{m3s}^2 + 2(k_{m7s}^2 - k_{m6s}^2)\dot{\theta} - (k_{m2s}^2 - k_{m1s}^2)\ddot{\theta} - (k_{m8s}^2 + k_{m9s}^2)\rangle \\
& - \langle (1 + \dot{\theta}^2)k_{m3s}^2 + 2k_{m7s}^2\dot{\theta} + k_{m1s}^2\ddot{\theta} - k_{m8s}^2\rangle\} \\
& + \dot{w'}\{2cos\theta sin\theta\langle 2k_{m3s}^2\dot{\theta} + (k_{m7s}^2 - k_{m6s}^2)\rangle \\
& + 2cos^2\theta\langle -(k_{m2s}^2 - k_{m1s}^2)\dot{\theta} - (k_{m4s}^2 + k_{m5s}^2)\rangle + 2\langle -k_{m1s}^2\dot{\theta} + k_{m4s}^2\rangle\} \\
& + \ddot{w'}\{-cos\theta sin\theta(k_{m2s}^2 - k_{m1s}^2) - 2cos^2\theta k_{m3s}^2 + k_{m3s}^2\} \\
& + \hat{\phi}\{(d_s cos\theta + e_s sin\theta)\langle -\tfrac{1}{2}\textstyle\int_0^x (v'^2 + w'^2)dx + x + \int_0^x (\dot{v'}^2 + v'\ddot{v'} + \dot{w'}^2 + w'\ddot{w'})dx\rangle \\
& - 4cos\theta sin\theta\langle k_{m3s}^2(\beta_p + 2\dot{\theta}) + (k_{m7s}^2 - k_{m6s}^2)\rangle + cos2\theta\langle (k_{m2s}^2 - k_{m1s}^2)(\beta_p + 2\dot{\theta}) \\
& + 2(k_{m4s}^2 + k_{m5s}^2)\rangle + \dot{\hat{\phi}}\langle sin2\theta(k_{m2s}^2 - k_{m1s}^2) + 2cos2\theta k_{m3s}^2\rangle]
\end{aligned}
$$

$$
\begin{aligned}
T_w = \quad & m_s[\beta_p(\tfrac{1}{2}\textstyle\int_0^x (v'^2 + w'^2)dx - x) + sin\theta\{e_s(\dot{\theta}^2 + 2\beta_p\dot{\theta}) + 2(\beta_p + \dot{\theta})\dot{d}_s + d_s\ddot{\theta} - \ddot{e}_s\} \\
& + cos\theta\{d_s(\dot{\theta}^2 + 2\beta_p\dot{\theta}) - 2(\beta_p + \dot{\theta})\dot{e}_s - e_s\ddot{\theta} - \ddot{d}_s\} \\
& - \beta_p u_e - 2\dot{v}\beta_p - \ddot{w} + v'\{\beta_p(e_s cos\theta - d_s sin\theta)\} \\
& + w'\{\beta_p(e_s sin\theta + d_s cos\theta)\} + \hat{\phi}\{-sin\theta\langle d_s(\dot{\theta}^2 + 2\beta_p\dot{\theta}) - 2(\beta_p + \dot{\theta})\dot{e}_s - e_s\ddot{\theta} - \ddot{d}_s\rangle \\
& + cos\theta\langle e_s(\dot{\theta}^2 + 2\beta_p\dot{\theta}) + 2(\beta_p + \dot{\theta})\dot{d}_s + d_s\ddot{\theta} - \ddot{e}_s\rangle\} \\
& + \dot{\hat{\phi}}\{2sin\theta\langle e_s(\beta_p + \dot{\theta} + \dot{d}_s)\rangle + 2cos\theta\langle s_s(\beta_p + \dot{\theta} - \dot{e}_s)\rangle\} \\
& + \ddot{\hat{\phi}}\{d_s sin\theta - e_s cos\theta\}]
\end{aligned}
$$

$$
\begin{aligned}
T_{w'} = \quad & m_s[(e_s sin\theta + d_s cos\theta)\{\tfrac{1}{2}\textstyle\int_0^x (v'^2 + w'^2)dx - x - \int_0^x (\dot{v'}^2 + v'\ddot{v'} + \dot{w'}^2 + w'\ddot{w'})dx\} \\
& + sin\theta cos\theta\{2k_{m3s}^2(\beta_p + 2\dot{\theta}) + 2(k_{m7s}^2 - k_{m6s}^2)\} \\
& + cos^2\theta\{-(\beta_p + 2\dot{\theta})(k_{m2s}^2 - k_{m1s}^2) - 2(k_{m4s}^2 + k_{m5s}^2)\} + k_{m2s}^2(\beta_p + 2\dot{\theta}) + 2k_{m5s}^2) \\
& + u_e\{-e_s sin\theta - d_s cos\theta\} + \ddot{u_e}\{e_s sin\theta + d_s cos\theta\} + 2\dot{v}\{-d_s cos\theta - e_s sin\theta\} \\
& + w\beta_p\{e_s sin\theta + d_s cos\theta\} + v'\{cos\theta sin\theta\langle(k_{m2s}^2 - k_{m1s}^2)(1 + \dot{\theta}^2) + 2(k_{m4s}^2 + k_{m5s}^2)\dot{\theta} \\
& + 2k_{m3s}^2\ddot{\theta} + (k_{m11s}^2 - k_{m10s}^2)\rangle \\
& + cos^2\theta\langle 2(1 + \dot{\theta}^2)k_{m3s}^2 + 2(k_{m7s}^2 - k_{m6s}^2)\dot{\theta} - (k_{m2s}^2 - k_{m1s}^2)\ddot{\theta} - (k_{m8s}^2 + k_{m9s}^2)\rangle \\
& + \langle -(1 + \dot{\theta}^2)k_{m3s}^2 + 2k_{m6s}^2\dot{\theta} + k_{m2s}^2\ddot{\theta} + k_{m9s}^2\rangle\} \\
& + \dot{v'}\{2cos\theta sin\theta\langle 2k_{m3s}^2\dot{\theta} + (k_{m7s}^2 - k_{m6s}^2)\rangle \\
& - 2cos^2\theta\langle(k_{m2s}^2 - k_{m1s}^2)\dot{\theta} - (k_{m4s}^2 + k_{m5s}^2)\rangle + 2\langle k_{m2s}^2\dot{\theta} + k_{m5s}^2\rangle \\
& + \ddot{v'}\{-cos\theta sin\theta(k_{m2s}^2 - k_{m1s}^2) - 2cos^2\theta k_{m3s}^2 + k_{m3s}^2\} \\
& + w'\{cos\theta sin\theta\langle 2k_{m3s}^2(1 + \dot{\theta}^2) + 2(k_{m7s}^2 - k_{m6s}^2)\dot{\theta} \\
& - (k_{m2s}^2 - k_{m1s}^2)\ddot{\theta} - (k_{m8s}^2 + k_{m9s}^2)\rangle \\
& + cos^2\theta\langle -(k_{m2s}^2 - k_{m1s}^2)(1 + \dot{\theta}^2) - 2(k_{m4s}^2 + k_{m5s}^2)\dot{\theta} - 2k_{m3s}^2\ddot{\theta} - (k_{m11s}^2 - k_{m10s}^2)\rangle \\
& + \langle(1 + \dot{\theta}^2)k_{m2s}^2 + 2k_{m5s}^2\dot{\theta} + k_{m3s}^2\ddot{\theta} - k_{m10s}^2\rangle\} \\
& + \dot{w'}\{2cos\theta sin\theta\langle -(k_{m2s}^2 - k_{m1s}^2)\dot{\theta} - (k_{m4s}^2 + k_{m5s}^2)\rangle \\
& + 2cos^2\theta\langle -2k_{m3s}^2\dot{\theta} - (k_{m7s}^2 - k_{m6s}^2)\rangle + 2\langle k_{m3s}^2\dot{\theta} - k_{m6s}^2\rangle\} \\
& + \ddot{w'}\{-2cos\theta sin\theta k_{m3s}^2 + cos^2\theta(k_{m2s}^2 - k_{m1s}^2) - k_{m2s}^2\} \\
& + \hat{\phi}\{(e_s cos\theta - d_s sin\theta)\langle\tfrac{1}{2}\textstyle\int_0^x (v'^2 + w'^2)dx - x - \int_0^x (\dot{v'}^2 + v'\ddot{v'} + \dot{w'}^2 + w'\ddot{w'})dx\rangle \\
& + 2cos\theta sin\theta\langle 2(k_{m2s}^2 - k_{m1s}^2)(\beta_p + 2\dot{\theta}) + 4(k_{m4s}^2 + k_{m5s}^2)\rangle \\
& + cos2\theta\langle 2k_{m3s}^2(\beta_p + 2\dot{\theta}) + 2(k_{m7s}^2 - k_{m6s}^2)\rangle \\
& + \dot{\hat{\phi}}\langle 2sin2\theta k_{m3s}^2 - 2cos2\theta(k_{m2s}^2 - k_{m1s}^2) + 2k_{m2s}^2\rangle]
\end{aligned}
$$

$$
\begin{aligned}
T_{\hat{\phi}} = \quad & m_s[-2(k_{m6s}^2 + k_{m7s}^2)(\beta_p + \dot{\theta}) - k_{ms}^2\ddot{\theta} + (k_{m8s}^2 - k_{m9s}^2) - k_{m3s}^2 cos2\theta \\
& + cos\theta\langle e_s\beta_p(\tfrac{1}{2}\textstyle\int_0^x (v'^2 + w'^2)dx - x) - 2d_s\int_0^x (v'\dot{v}' + w'\dot{w}')dx\rangle \\
& + sin\theta\langle -d_s\beta_p(\tfrac{1}{2}\textstyle\int_0^x (v'^2 + w'^2)dx - x) - 2e_s\int_0^x (v'\dot{v}' + w'\dot{w}')dx\rangle \\
& - cos\theta sin\theta(k_{m2s}^2 - k_{m1s}^2) + u_e\{\beta_p(d_s sin\theta - e_s cos\theta)\} + 2\dot{u_e}\{e_s sin\theta + d_s cos\theta\} \\
& - v\{e_s sin\theta + d_s cos\theta\} + 2\dot{v}\{\beta_p(d_s sin\theta - e_s cos\theta)\} \\
& + \ddot{v}\{e_s sin\theta + d_s cos\theta\} - 2\dot{w}\{\beta_p(e_s sin\theta + d_s cos\theta)\} + \ddot{w}\{d_s sin\theta - e_s cos\theta\} \\
& + v'\{(e_s sin\theta + d_s cos\theta)(-\tfrac{1}{2}\textstyle\int_0^x (v'^2 + w'^2)dx + x + \int_0^x (\dot{v'}^2 + v'\ddot{v}' + \dot{w'}^2 + w'\ddot{w}')dx) \\
& - 2sin2\theta\beta_p k_{m3s}^2 + \beta_p cos2\theta(k_{m2s}^2 - k_{m1s}^2)\} \\
& + \dot{v}'\{-2sin2\theta(k_{m2s}^2 - k_{m1s}^2) - 2k_{m3s}^2 cos2\theta\} \\
& + w'\{(e_s cos\theta - d_s sin\theta)(\tfrac{1}{2}\textstyle\int_0^x (v'^2 + w'^2)dx - x - \int_0^x (\dot{v'}^2 + v'\ddot{v}' + \dot{w'}^2 + w'\ddot{w}')dx) \\
& + cos2\theta\langle 2\beta_p k_{m3s}^2 - 2(k_{m6s}^2 + k_{m7s}^2)\rangle + \beta_p sin2\theta(k_{m2s}^2 - k_{m1s}^2)\} \\
& + \dot{w}'\{-2sin2\theta k_{m3s}^2 + 2cos^2\theta(k_{m2s}^2 - k_{m1s}^2) - 2k_{m2s}^2\} \\
& + \hat{\phi}\{(e_s sin\theta + d_s cos\theta)\beta_p(-\tfrac{1}{2}\textstyle\int_0^x (v'^2 + w'^2)dx + x) \\
& + 2(d_s sin\theta - e_s cos\theta)\textstyle\int_0^x (v'\dot{v}' + w'\dot{w}')dx \\
& - cos2\theta(k_{m2s}^2 - k_{m1s}^2) + 2sin2\theta k_{m3s}^2\} \\
& + \dot{\hat{\phi}}\{-2(k_{m6s}^2 + k_{m7s}^2)\} - \ddot{\hat{\phi}}k_{ms}^2]
\end{aligned}
$$

$$
\begin{aligned}
T_{\chi_b} = \quad & m_s R_s[\beta_p cos(\theta+\chi_b)(\tfrac{1}{2}\textstyle\int_0^x (v'^2+w'^2)dx - x) - 2sin(\theta+\chi_b)\int_0^x (v'\dot{v}'+w'\dot{w}')dx \\
& +(2\beta_p+\dot{\theta})\dot{\theta}(d_s cos\chi_b - e_s sin\chi_b) - 2(\beta_p+\dot{\theta})(\dot{d}_s sin\chi_b + \dot{e}_s cos\chi_b) \\
& -(e_s cos\chi_b + d_s sin\chi_b)\ddot{\theta} + (\ddot{e}_s sin\chi_b - \ddot{d}_s cos\chi_b) + d_s cos\chi_b \\
& -cos^2\theta(d_s cos\chi_b + e_s sin\chi_b) + sin\theta cos\theta(d_s sin\chi_b - e_s cos\chi_b) \\
& +u_e\{-cos(\theta+\chi_b)\beta_p\} + \dot{u_e}\{2sin(\theta+\chi_b)\} - v\{sin(\theta+\chi_b)\} \\
& -\dot{v}\{2\beta_p cos(\theta+\chi_b)\} + \ddot{v}sin(\theta+\chi_b) \\
& +\dot{w}\{-2\beta_p sin(\theta+\chi_b)\} + \ddot{w}\{-cos(\theta+\chi_b)\} \\
& +v'\{sin(\theta+\chi_b)(-\tfrac{1}{2}\textstyle\int_0^x (v'^2+w'^2)dx + x + \int_0^x (\dot{v}'^2 + v'\ddot{v}' + \dot{w}'^2 + w'\ddot{w}')dx) \\
& +cos\theta sin\theta\langle -2\beta_p(e_s sin\chi_b + d_s cos\chi_b)\rangle \\
& +cos2\theta\langle \beta_p(e_s cos\chi_b - d_s sin\chi_b)\rangle\} \\
& +\dot{v}'\{sin2\theta(d_s sin\chi_b - e_s cos\chi_b) - 2cos^2\theta(e_s sin\chi_b + d_s cos\chi_b) + 2d_s cos\chi_b\} \\
& +w'\{cos(\theta+\chi_b)(\tfrac{1}{2}\textstyle\int_0^x (v'^2+w'^2)dx - x - \int_0^x (\dot{v}'^2 + v'\ddot{v}' + \dot{w}'^2 + w'\ddot{w}')dx) \\
& +sin2\theta\langle \beta_p(e_s cos\chi_b - d_s sin\chi_b)\rangle + 2cos^2\theta\langle \beta_p(d_s cos\chi_b + e_s sin\chi_b)\rangle \\
& -2\beta_p e_s sin\chi_b + 2(d_s cos\chi_b - e_s sin\chi_b)\dot{\theta} - 2(\dot{d}_s sin\chi_b + \dot{e}_s cos\chi_b)\} \\
& +\dot{w}'\{-sin2\theta(d_s cos\chi_b + e_s sin\chi_b) + 2cos^2\theta(e_s cos\chi_b - d_s sin\chi_b) - 2e_s cos\chi_b\} \\
& +\hat{\phi}\{sin(\theta+\chi_b)(x - \tfrac{1}{2}\textstyle\int_0^x (v'^2+w'^2)dx) - 2cos(\theta+\chi_b)\int_0^x (v'\dot{v}'+w'\dot{w}')dx \\
& +sin2\theta(e_s sin\chi_b + d_s cos\chi_b) + cos2\theta(d_s sin\chi_b - e_s cos\chi_b)\} \\
& +\dot{\hat{\phi}}\{2(\beta_p+\dot{\theta})(d_s cos\chi_b - e_s sin\chi_b) - 2(\dot{d}_s sin\chi_b + \dot{e}_s cos\chi_b)\} \\
& -\ddot{\hat{\phi}}\{e_s cos\chi_b + d_s sin\chi_b\}]
\end{aligned}
$$

$$
\begin{aligned}
T_{\chi_s} = \quad & m_s[\beta_p e_s^a cos(\theta+\chi_s)(\tfrac{1}{2}\textstyle\int_0^x (v'^2+w'^2)dx - x) \\
& -2e_s^a sin(\theta+\chi_s)\textstyle\int_0^x (v'\dot{v}'+w'\dot{w}')dx \\
& +(2\beta_p+\dot{\theta})\dot{\theta}(d_{s\eta}^2 cos\chi_s - e_{s\eta}^2 sin\chi_s) - 2(\beta_p+\dot{\theta})(\dot{d}_{s\eta}^2 sin\chi_s + \dot{e}_{s\eta}^2 cos\chi_s) \\
& -(e_{s\eta}^2 cos\chi_s + d_{s\eta}^2 sin\chi_s)\ddot{\theta} + (\ddot{e}_{s\eta}^2 sin\chi_s - \ddot{d}_{s\eta}^2 cos\chi_s) + d_{s\eta}^2 cos\chi_s \\
& -cos^2\theta(d_{s\eta}^2 cos\chi_s + e_{s\eta}^2 sin\chi_s) + sin\theta cos\theta(d_{s\eta}^2 sin\chi_s - e_{s\eta}^2 cos\chi_s) \\
& +u_e\{-cos(\theta+\chi_s)\beta_p e_s^a\} + \dot{u_e}\{2e_s^a sin(\theta+\chi_s)\} \\
& -v\{e_s^a sin(\theta+\chi_s)\} - \dot{v}\{2\beta_p e_s^a cos(\theta+\chi_s)\} + \ddot{v}e_s^a sin(\theta+\chi_s) \\
& +\dot{w}\{-2\beta_p e_s^a sin(\theta+\chi_s)\} + \ddot{w}\{-e_s^a cos(\theta+\chi_s)\} \\
& +v'\{e_s^a sin(\theta+\chi_s)(-\tfrac{1}{2}\textstyle\int_0^x (v'^2+w'^2)dx + x + \int_0^x (\dot{v}'^2 + v'\ddot{v}' + \dot{w}'^2 + w'\ddot{w}')dx) \\
& +cos\theta sin\theta\langle -2\beta_p(e_{s\eta}^2 sin\chi_s + d_{s\eta}^2 cos\chi_s)\rangle + cos2\theta\langle\beta_p(e_{s\eta}^2 cos\chi_s - d_{s\eta}^2 sin\chi_s)\rangle\} \\
& +\dot{v}'\{sin2\theta(d_{s\eta}^2 sin\chi_s - e_{s\eta}^2 cos\chi_s) - 2cos^2\theta(e_{s\eta}^2 sin\chi_s + d_{s\eta}^2 cos\chi_s) + 2d_{s\eta}^2 cos\chi_s\} \\
& +w'\{e_s^a cos(\theta+\chi_s)(\tfrac{1}{2}\textstyle\int_0^x (v'^2+w'^2)dx - x - \int_0^x (\dot{v}'^2 + v'\ddot{v}' + \dot{w}'^2 + w'\ddot{w}')dx) \\
& +sin2\theta\langle\beta_p(e_{s\eta}^2 cos\chi_s - d_{s\eta}^2 sin\chi_s)\rangle + 2cos^2\theta\langle\beta_p(d_{s\eta}^2 cos\chi_s + e_{s\eta}^2 sin\chi_s)\rangle \\
& -2\beta_p e_{s\eta}^2 sin\chi_s \\
& +2(d_{s\eta}^2 cos\chi_s - e_{s\eta}^2 sin\chi_s)\dot{\theta} - 2(\dot{d}_{s\eta}^2 sin\chi_s + \dot{e}_{s\eta}^2 cos\chi_s)\} \\
& +\dot{w}'\{-sin2\theta(d_{s\eta}^2 cos\chi_s + e_{s\eta}^2 sin\chi_s) + 2cos^2\theta(e_{s\eta}^2 cos\chi_s - d_{s\eta}^2 sin\chi_s) - 2e_{s\eta}^2 cos\chi_s\} \\
& +\hat{\phi}\{e_s^a sin(\theta+\chi_s)(x - \tfrac{1}{2}\textstyle\int_0^x (v'^2+w'^2)dx) - 2e_s^a cos(\theta+\chi_s)\int_0^x (v'\dot{v}'+w'\dot{w}')dx \\
& +sin2\theta(e_{s\eta}^2 sin\chi_s + d_{s\eta}^2 cos\chi_s) + cos2\theta(d_{s\eta}^2 sin\chi_s - e_{s\eta}^2 cos\chi_s)\} \\
& +\dot{\hat{\phi}}\{2(\beta_p+\dot{\theta})(d_{s\eta}^2 cos\chi_s - e_{s\eta}^2 sin\chi_s) - 2(\dot{d}_{s\eta}^2 sin\chi_s + \dot{e}_{s\eta}^2 cos\chi_s)\} \\
& -\ddot{\hat{\phi}}\{e_{s\eta}^2 cos\chi_s + d_{s\eta}^2 sin\chi_s\}]
\end{aligned}
$$

2.5.6 Non-conservative forces - virtual work

This is expressed as :

$$\delta\overline{W} = \frac{\delta W}{m_0\Omega^2R^3} = \int_0^R (L_u\delta u + L_v\delta v + L_w\delta w + M_{\hat{\phi}}\delta\hat{\phi} + M_{\chi_b}\delta\chi_b + M_{\chi_s}\delta\chi_s)dx \quad (2.10)$$

where the slat contributions are only across its physical spanwise and chordwise limits.

The airloads L_u, L_v, L_w in the x,y,z directions and the aerodynamic moments about the elastic axis and slat hinges $M_{\hat{\phi}}, M_{\chi_b}, M_{\chi_s}$ are calculated from unsteady theory or using look-up tables for the airfoil with slat attached, for different angles of attack, slat positions and local Mach number.

2.5.7 Assembly of final equations of motion

Hence, using the expression for Hamilton's variational principle, Eqn. 2.7 and the separate contributions from the slat (Eqns. 2.8-2.10) and blade (and/or trailing-edge flaps) and the work done by external forces Eqn. 2.10, we can obtain the governing equations for extension (u_e), bending (v, w), torsion ($\hat{\phi}$), and the slat motions (χ_b, χ_s) by setting the coefficients of the variations in the following equation to zero.

$$\int_{t_1}^{t_2} \{(....)\delta u + (....)\delta v + (....)\delta w + (....)\delta\hat{\phi} + (....)\delta\chi_b + (....)\delta\chi_s\}dt = 0 \quad (2.11)$$

2.6 Slatted airfoil characteristics:

The slat configurations explored were proposed by Lorber et al.([75]).Figure 1(a) shows slat configurations S0, S1 and S6. Configuration S1 is a compromise between high lift and low drag, while S6 (which has the slat element deployed further forward) provides still higher maximum lift, with higher drag (at small angles of attack) as well. S0 is a baseline position with a low drag penalty. The slatted blade sections had the SC2110 baseline/slatted airfoils in place of the baseline UH-60A airfoils: SC1095 and SC1094R8. The slat configurations were designed for optimum channeling of the flow near the leading-edge of the SC2110 airfoil, hence the replacement of the baseline UH-60A airfoils in the slat sections.

The correlations between the slat configurations used by Lorber et al.([75]) and the slat motion prescribed in this study are given in Fig.2.29.

2.7 Validation of the leading-edge slat model

The purely aerodynamic effect of slats was examined by fitting the baseline rotor with slatted airfoils, without any modifications to the rotor dynamics due to slats. Fig.2.31 shows the predicted hover performance (FM vs. C_T/σ) of the UH-60A rotor fitted with the SC2110/S1/S6 airfoils in place of the SC1094R8([88]).

The two-dimensional(2D) airfoil characteristics (C_l, C_d, C_m) in the C-81 table look-up format for the slatted sections were generated using CFD analysis

TURNS([89]) for the SC2110 airfoil section as well as the slat orientations S1 and S6. Dynamic slat actuations were simulated by a look-up table scheme interpolating between different orientations across azimuth, identified by the rotation angle of the slat element with respect to the baseline profile. Note that the slatted sections are assumed to move such that the offset between the elastic axis and effective quarter chord is invariant at any radial location. The aerodynamic characteristics of the SC2110 and the S1 and S6-slatted airfoil sections were obtained at steps of 0.1 in Mach number between 0.3 and 0.7 and 2° in angle of attack from about -15° to 25°.The 4 coefficients, namely C_l,C_d, C_l/C_d and C_m are plotted against angle of attack(α)(deg) at a representative Mach number as shown in Fig.2.30. All coefficients are referenced to the 'effective' airfoil chord (and pitching moments defined about the 'effective quarter-chord point'), as defined in Fig. 2.27. In general, the slat elements improve the maximum lift characteristics of the blade section, while imposing a drag penalty at small angles.

The slat dynamics model in UMARC was evaluated for various flight conditions of interest, especially high thrust and forward flight conditions.The validation of the baseline UH-60A forward flight performance with flight test data from the Airloads Programme([79]) was carried out for two weight coefficients of C_W/σ=0.0783(flight 85) and C_W/σ=0.0891(flight 84).The break-up of the power into different components,namely the profile,parasite and induced/propulsive power was carried out for the purpose of performance evaluation. Figs. 2.32 and 2.33 show the various components of the main rotor power coefficient as a function of advance ratio,respectively for C_T/σ=0.0783 and C_T/σ=0.0891.

The correlation of predictions with test data is quite satisfactory.

UNIVERSITY OF MARYLAND

- **Correlation between experiment and slat motion model**

Position	η_h/c	ζ_h/c	χ_s(deg)
S1	0.21	0.06	5.2
S2	0.21	0.06	10.2
S3	0.21	0.06	0.2
S4	0.22	0.05	10.2
S5	0.22	0.05	12.7
S6	0.23	0.04	12.7

- **Proposed motion : periodic between S1 on advancing blade ($\psi = 90^0$) and S6 on retreating blade ($\psi = 270^0$)**

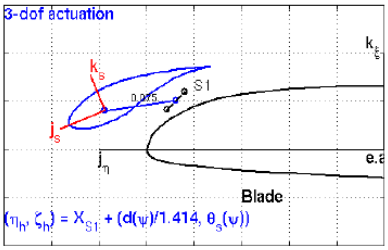

Figure 2.29: Correlation between experiments and slat motion

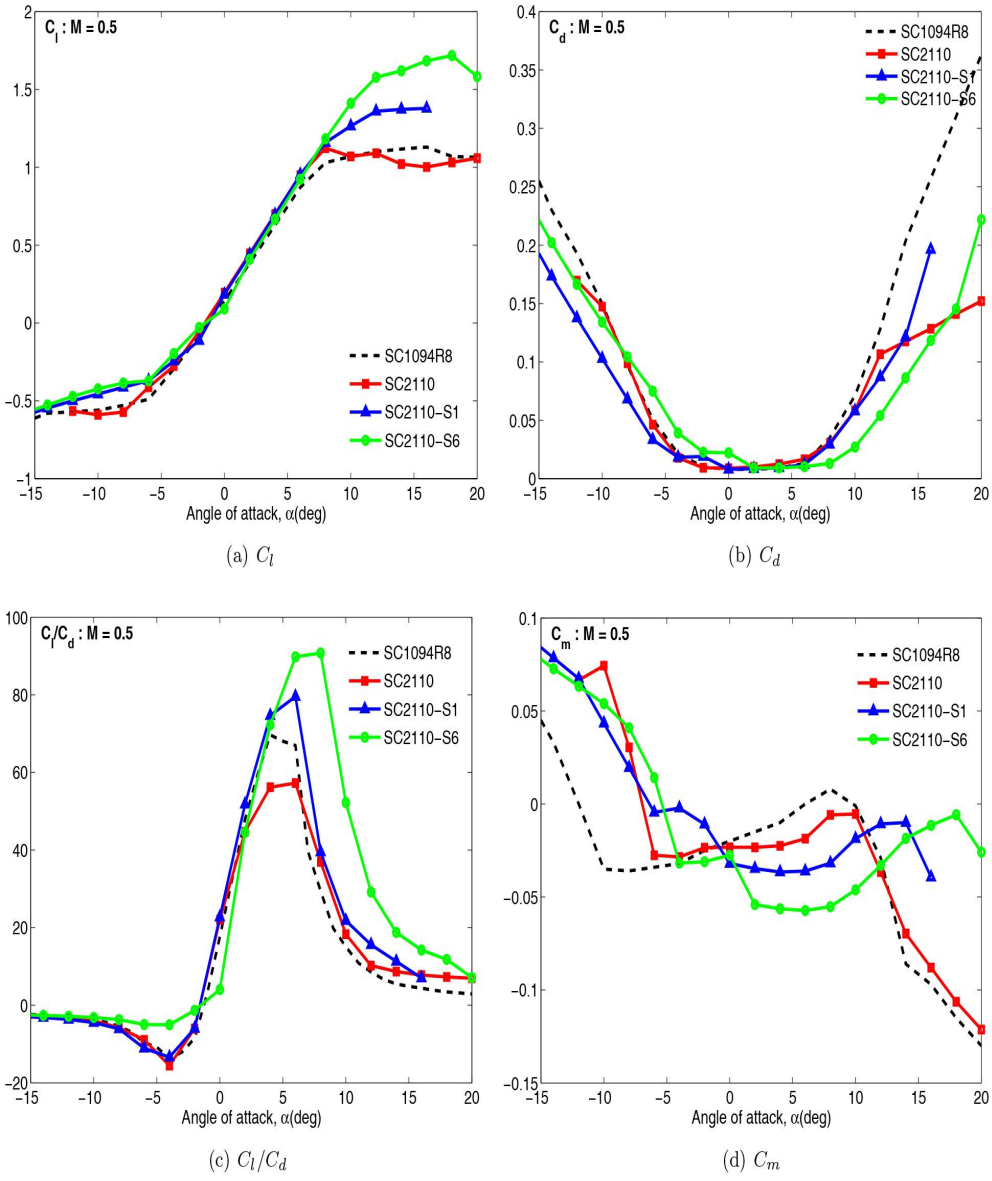

(a) C_l (b) C_d

(c) C_l/C_d (d) C_m

Figure 2. 2D CFD-generated airfoil characteristics (SC2110) with S1 and S6 slats, and SC1094R8 airfoil, at M = 0.5

Figure 2.30: 2D CFD-generated airfoil characteristics

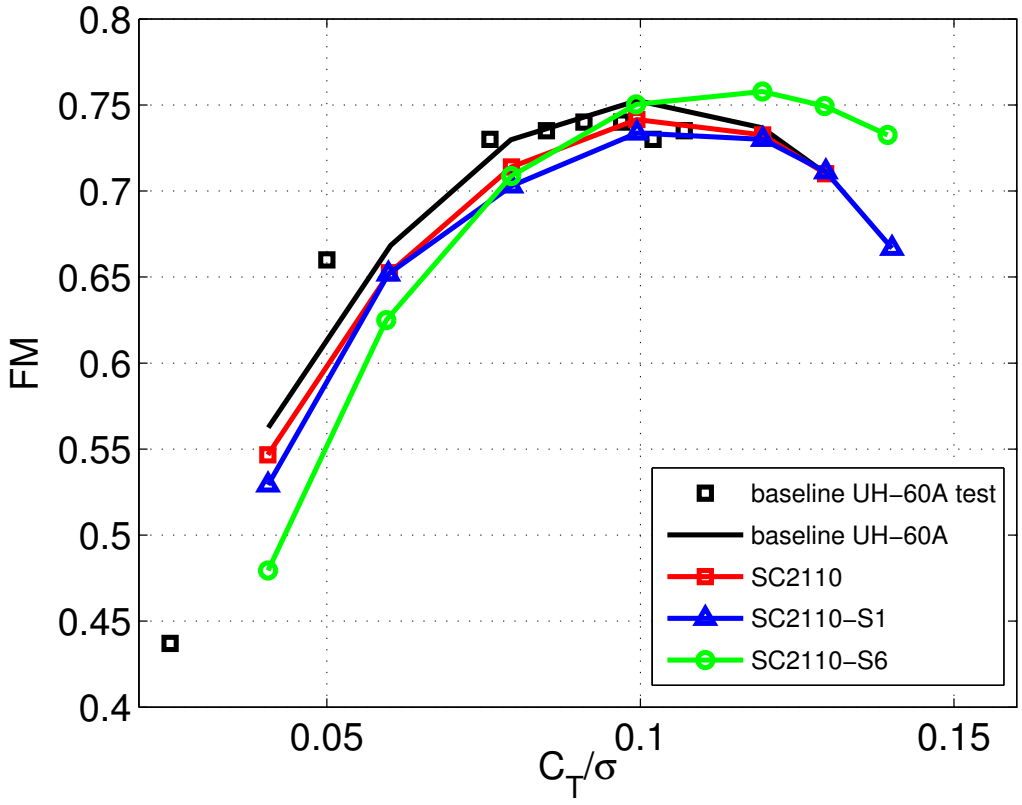

Figure 2.31: Hover performance with slatted airfoils

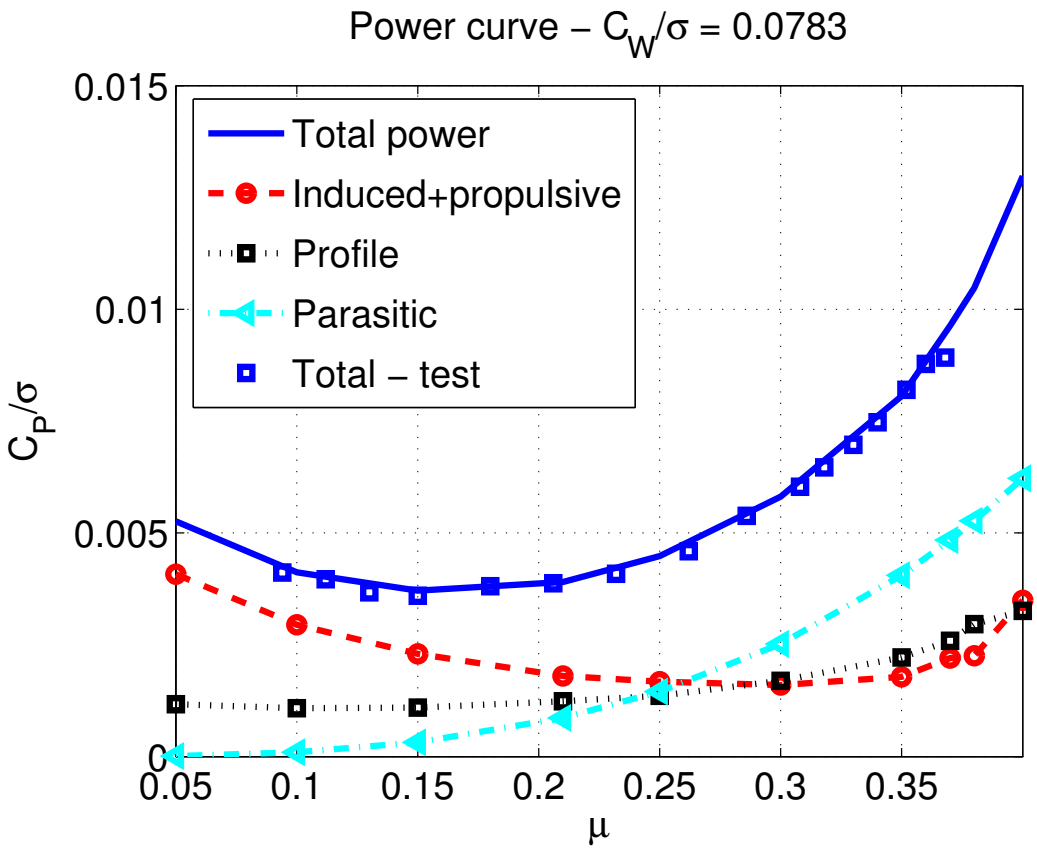

Figure 2.32: UH-60A main rotor power in forward flight(flight 85)

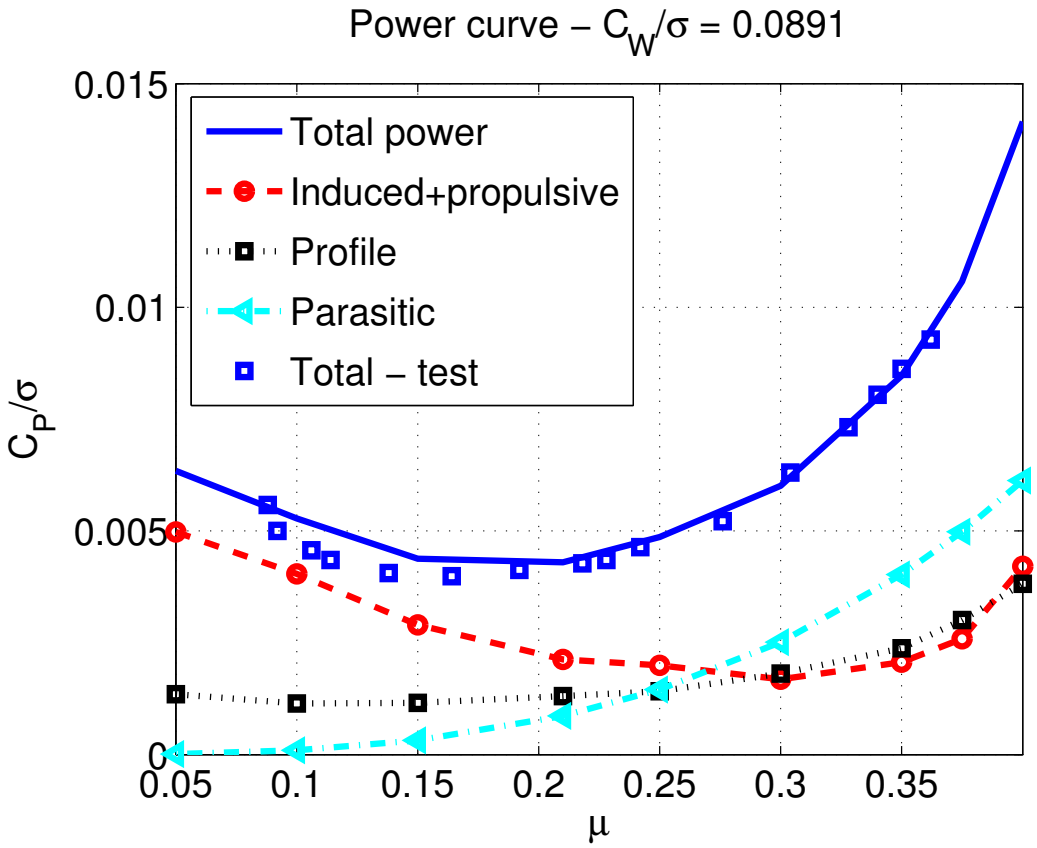

Figure 2.33: UH-60A main rotor power in forward flight(flight 84)

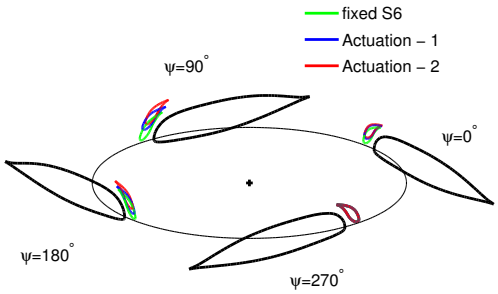

(a) Slat deployment across azimuth

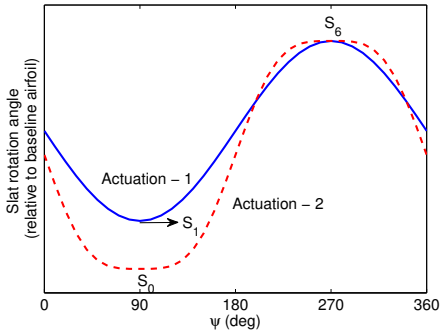

(b) Dynamic actuations 1 and 2

Figure 2.34: Slat actuations.Actuation 1 passes through S1 at $\psi = 90°$ and S6 at $\psi = 270°$, and Actuation 2 passes through S0 at $\psi = 90°$ and S6 at $\psi = 270°$

Chapter 3: Trailing-Edge Flaps

3.1 Results and discussion

In this chapter, the presentation of the results is organized so as to systematically build on the objectives of the study, namely, the effects of active control with TEFs on performance in terms of power consumption, vibration, and dynamic stall. First, hover performance is considered. Next, the level high speed, high vibration, moderate thrust flight condition C8534 from the UH-60A airloads program (Ref.([83])) is explored for vibration reduction and power reduction, and finally for simultaneous power and vibration reduction with TEFs. Next, the standard high altitude, high thrust flight condition C9017 is explored for power reduction, stall alleviation and vibration reduction with TEFs. This chapter concludes with a summary of key observations from the study.

The rotor properties,TEF geometry and standard flight conditions used in this study are listed in Table 2.1.

The UH-60A performance data shown here are computed by the University of Maryland Advanced Rotor Code (UMARC - Ref. [80]) and the results are validated with the available flight data from the UH-60 Airloads Program.

The validation of the baseline UH-60A hover performance with flight test data

from the airloads program was carried out with the shaft angles fixed to zero. Fig. 3.1 presents the main rotor figure of merit as a function of blade loading (C_T/σ).

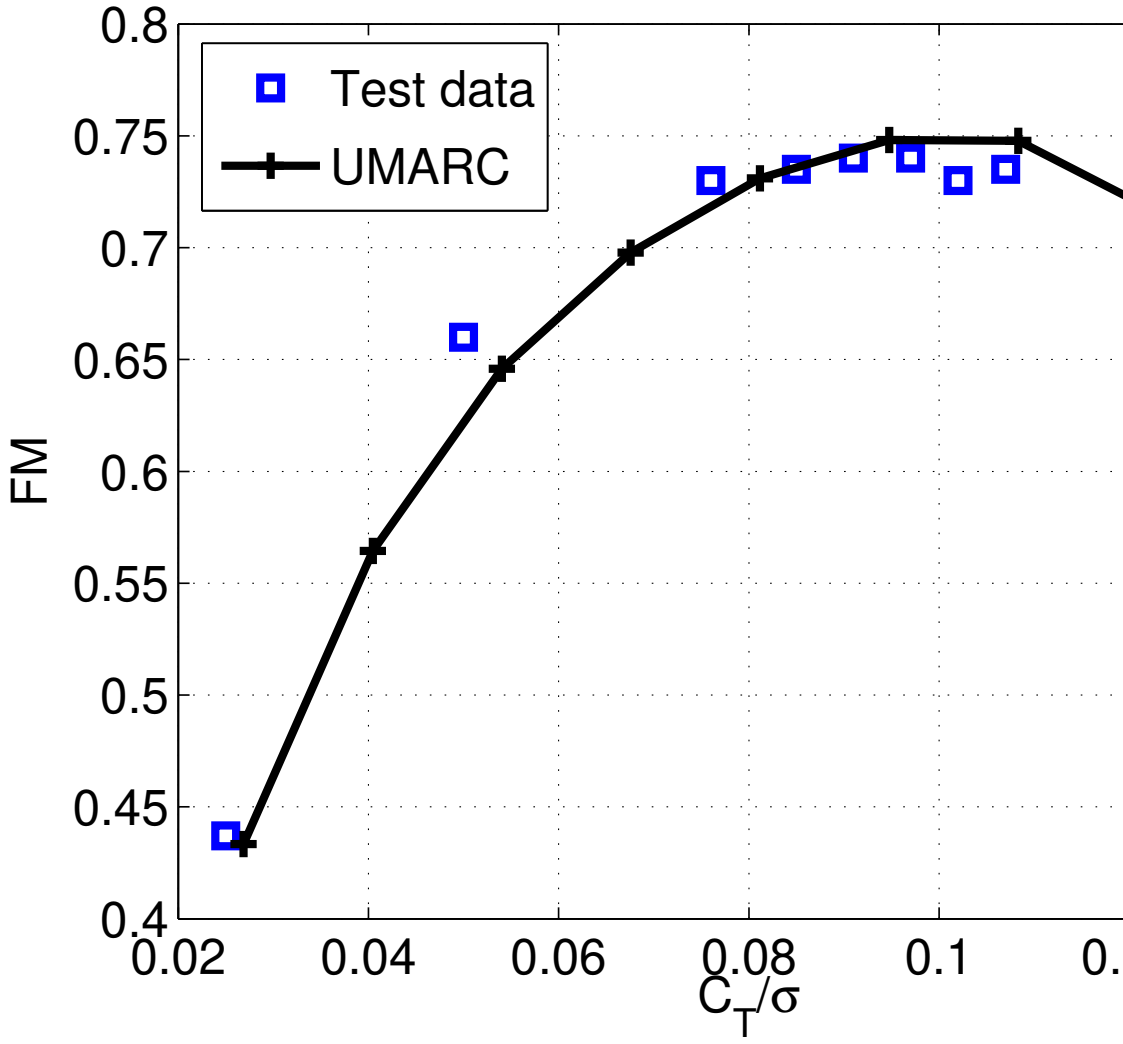

Figure 3.1: Baseline UH-60A hover performance

3.2 Blade torsional stiffness and TEF effectiveness

The TEF used in this study is a 'moment flap'.It operates by modifying the section pitching moments and inducing blade elastic twist in response to the moments.

A parameter that directly affects the blade twist, and therefore, the effectiveness of the TEF, is the torsional stiffness(GJ of the blade).As part of this study, the torsional stiffness of the blade was reduced by upto 50% to investigate any performance benefits from torsional softening of the blade. The rotor fan plots for the baseline blade and the soft blade(50% of the baseline blade GJ)are shown in Fig. 3.2. The effect of torsional stiffness is primarily on the blade first torsional mode:the 1st torsion frequency reduces from 4.3/rev for the baseline blade to 3.3/rev for the 50% stiff blade.This will be shown later to influence the vibratory loads.

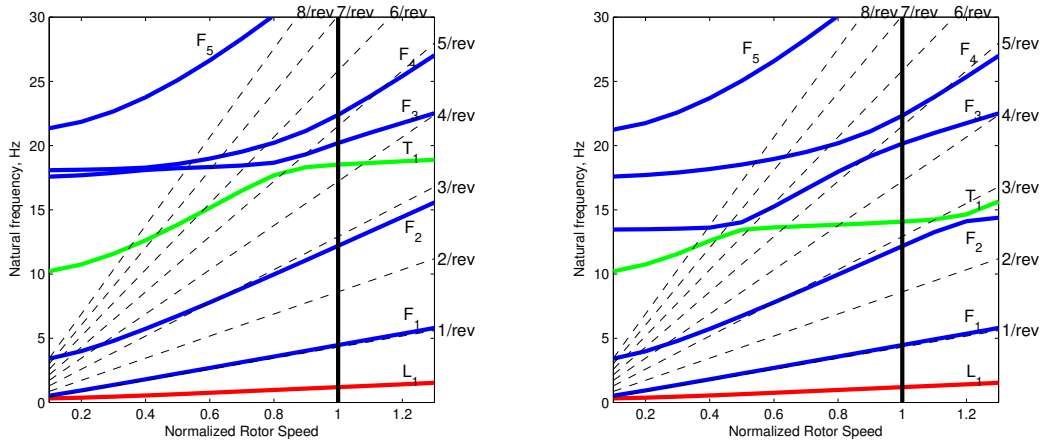

(a) Baseline (100%GJ) blade

(b) Baseline (50%GJ blade

Figure 3.2: Uh-60A rotor blade frequencies *in vacuo*;F:Flap, L:Lead-Lag,T:Torsion

3.3 Hover performance with TEFs

The impact of TEFs on hover performance was examined by estimating the UH-60A rotor figure of merit(FM) with different steady flap deflections ($-5°$, $0°$, $5°$, $10°$). The results with TEFs and/or hypothetical blade torsional stiffnesses indicate

the predicted trends only. UMARC FM changes should be considered qualitative only, as the flowfield model does not fully capture vortex interaction effects.

Fig. 3.3 compares the rotor figure of merit for the baseline blade with different steady flap deflections. A positive (downward) flap deflection improves the rotor performance, especially at higher thrust levels. The percent changes in power and the induced and profile power components from the no-flap condition are given in Fig. 3.4. A negative value indicates a reduction in the component of power from the corresponding value for the baseline blade at the same thrust level.

The effect of positive (downward)TEF deflections is to increase the nose-down elastic twist of the blade from root to tip, thus making the peak of the spanwise loading move inboard and hence reducing induced power. The power reductions with flap deflections is therefore largely attributable to the induced power. Since the flap analyzed(Table 1)operates by inducing blade twist,the effectiveness of the TEF with variation in blade torsional stiffness was also investigated.The rotor figure of merit for the baseline and 75% torsional stiffness blades without TEFs is compared in Fig. 3.5.The combined effect of reduced stiffness and steady flap deflections is illustrated in Fig. 3.6 which shows the improved figure of merit for the rotor with the 75% stiff blade and with 10° TEF deflections.

As an illustration of the benefits of both TEF deflections and softer blades, the spanwise elastic twist and loading of the blade are shown in Fig. 3.7, for the baseline (100% GJ) blade, 75% GJ blade and the 100% and 75% GJ blades with TEF deflection of 10°. Hence, there is a net increase in the blade elastic twist response as a result of either reduced stiffness or a positive TEF deflection, and the

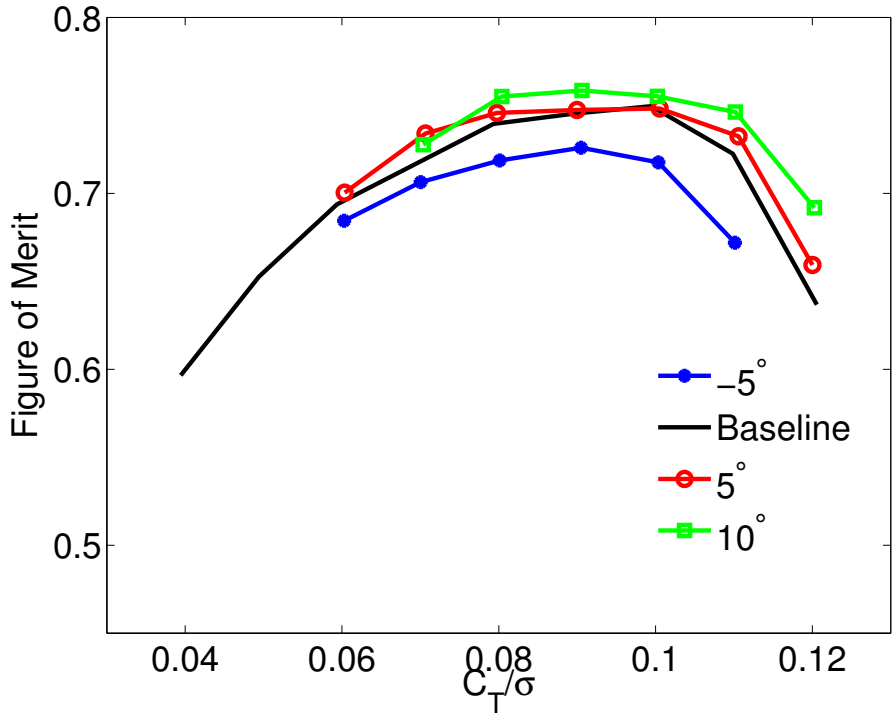

Figure 3.3: Effect of TEF (10%R, 15%c, midspan location at 65%R) deflection on baseline UH-60A rotor figure of merit; hover

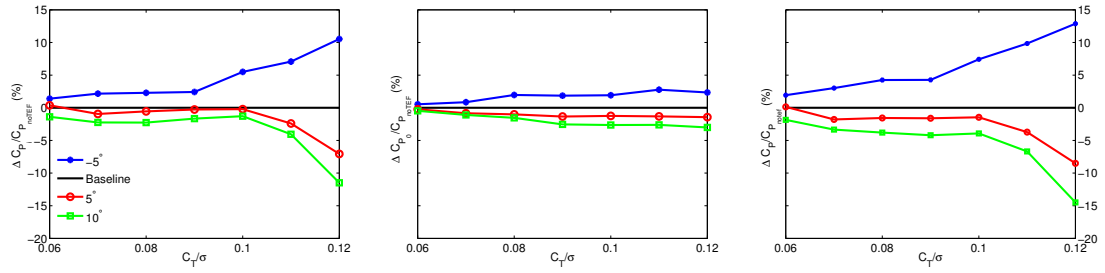

(a) Induced power (b) Profile power (c) Total power

Figure 3.4: Percent change in induced, profile and total power for UH-60A rotor in comparison to baseline for different TEF deflections; hover

spanwise loading gets redistributed inboard compared to the baseline blade. The integrated induced losses are thus reduced.

The improvements in FM are appreciable at high thrusts, both due to a reduction in torsional stiffness and TEF deflections. For instance, there is an increase of about 24% in figure of merit over the baseline blade when a 10° downward deflected TEF is used on a 75% torsionally stiff blade operating at a thrust level of $C_T/\sigma = 0.12$.

3.4 Rotor performance in high speed forward flight with TEFs

TEFs deployed at 1 or 2/rev are capable of redistributing the aerodynamic loads across the rotor disk, so that net performance gains can be realized. In general, the gains are attributed to the alleviation of the negative loading on the advancing blade, caused by the high negative pre-twist. Deflections of TEFs induce blade twisting, which in turn redistributes disk loads and minimizes negative loading. In this section, actuation requirements to achieve this objective are investigated.

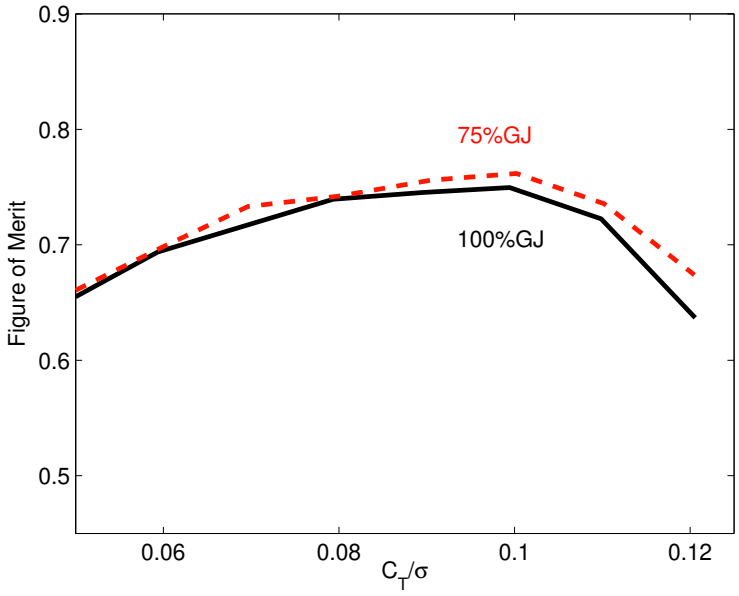

Figure 3.5: Effect of GJ with no TEF on baseline UH-60A rotor figure of merit; hover

Parametric sweeps of TEF actuations were carried out to determine suitable combinations of steady, 1/rev and 2/rev TEF inputs that yield overall power reductions. Actuation schedules were of the form $\delta = \delta_{steady} + \delta_{1p}\cos(\psi + \phi_{1p}) + \delta_{2p}\cos(2\psi + \phi_{2p})$, for varying amplitudes δ_{steady}, δ_{1p}, δ_{2p} and phase angles ϕ_{1p}, ϕ_{2p}. The cases were developed in the following stages:

1. $\delta = \delta_{steady} + \delta_{2p}\cos(2\psi + \phi_{2p})$: Different combinations of steady and 2/rev TEF inputs were prescribed, in order to obtain the trends of the actuations that had the best impact on performance. Two advance ratios, $\mu = 0.3$ and 0.4, were chosen for the study, and different thrust levels (in terms of C_W/σ) were investigated.

2. $\delta = \delta_{steady} + \delta_{1p}\cos(\psi + \phi_{1p}) + \delta_{2p}\cos(2\psi + \phi_{2p})$: Different 1/rev TEF inputs

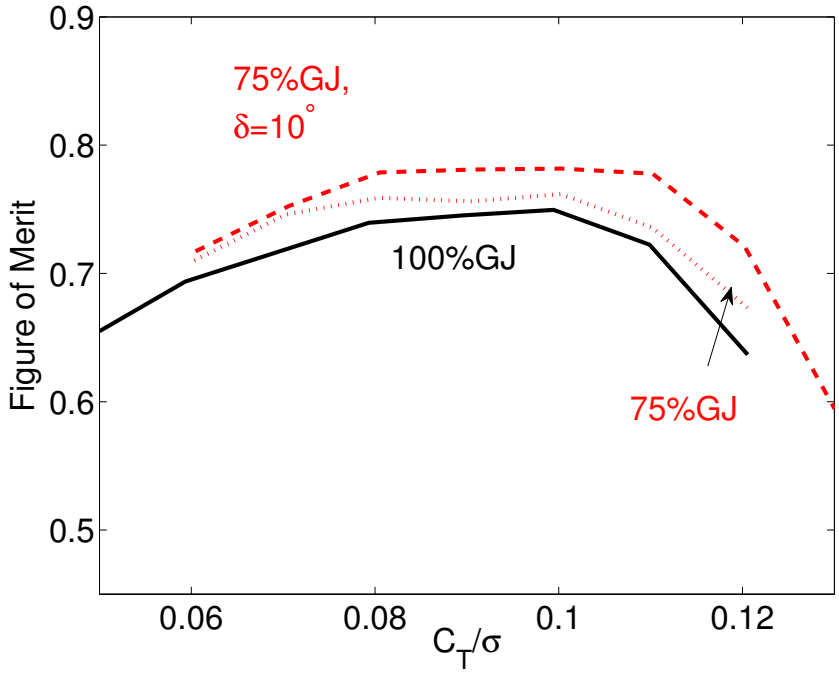

Figure 3.6: Effect of a 25% reduction in GJ and 10° TEF deflection on UH-60A rotor figure of merit; hover

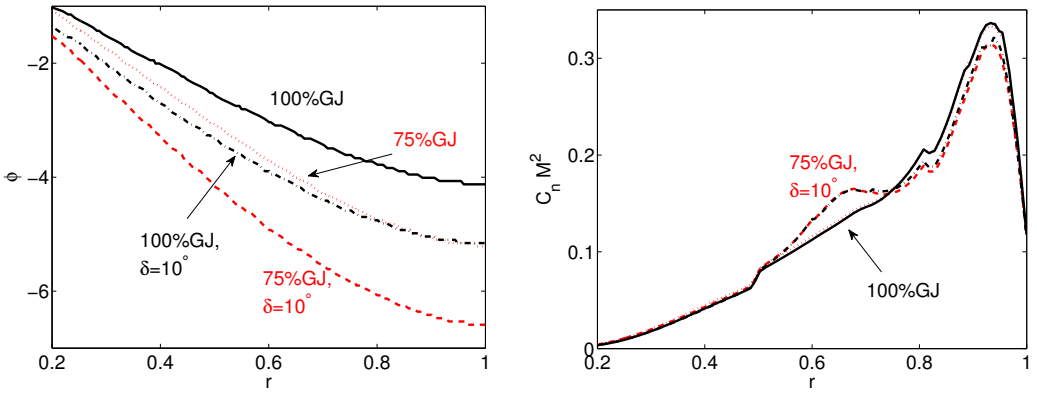

(a) Elastic twist

(b) Normal force $C_n M^2$

Figure 3.7: Effect of a 25% reduction in blade GJ and 10° TEF deflection on the spanwise variation of UH-60A rotor blade elastic twist and section normal force; hover, C_T/σ=0.12

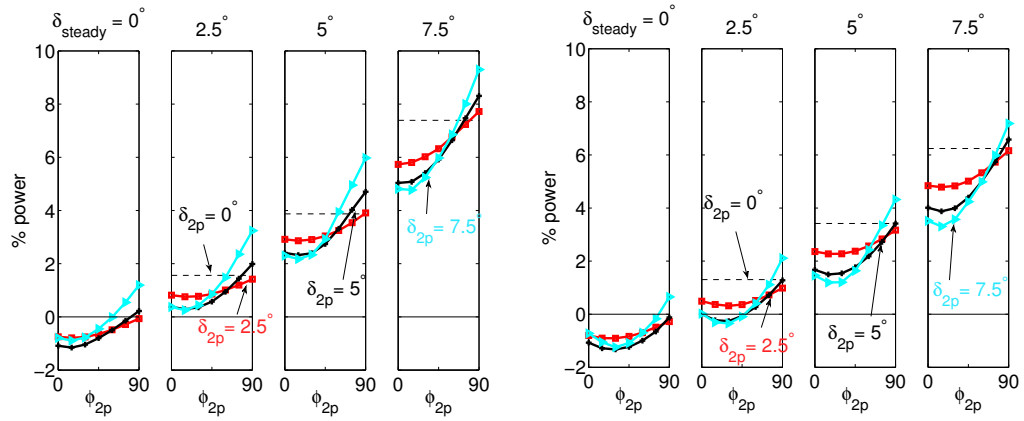

(a) $C_W/\sigma = 0.06$ (b) $C_W/\sigma = 0.08$

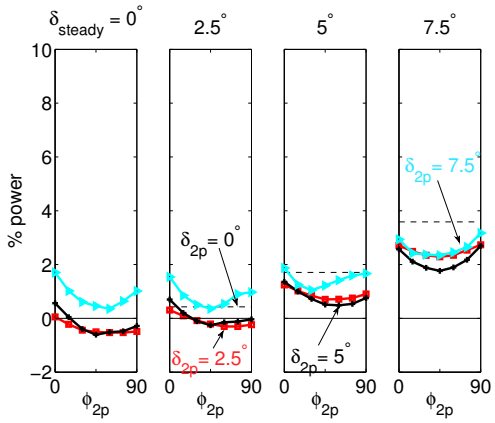

(c) $C_W/\sigma = 0.1$

Figure 3.8: Effect of 2/rev phasing of TEF (10%R, 15%c, midspan location at 65%R) inputs $\delta = \delta_{steady} + \delta_{2p}\cos(2\psi + \phi_{2p})$ on UH-60A rotor power for different weights; $\mu = 0.3$

were directly superimposed on specific steady plus 2/rev inputs from stage (i), that were most beneficial to power.

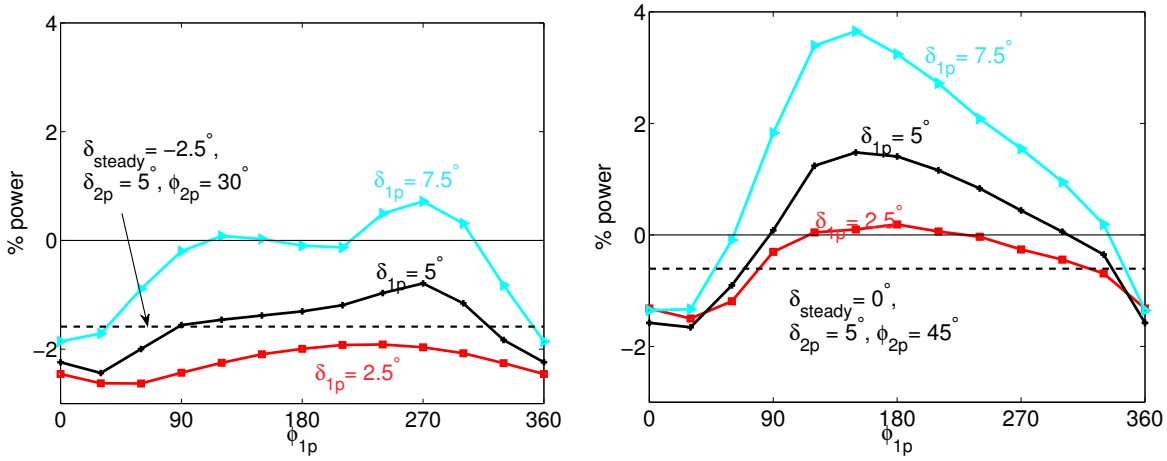

(a) $C_W/\sigma = 0.08$; (b) $C_W/\sigma = 0.1$;

Figure 3.9: Effect of 1/rev phasing of TEF (10%R, 15%c, midspan location at 65%R) inputs $\delta = \delta_{steady} + \delta_{1p}\cos(\psi + \phi_{1p}) + \delta_{2p}\cos(2\psi + \phi_{2p})$ on UH-60A rotor power for different weights; $\mu = 0.3$

3.4.1 Case I: Advance ratio $\mu = 0.3$

Steady plus 2/rev TEF input: Fig. 3.8 shows the percentage change in power for the flapped rotor operating at μ of 0.3 and weight coefficient C_W/σ between 0.06 and 0.1, from the respective baseline case (no flaps), with different combinations of steady and 2/rev inputs of amplitudes from 0° to 7.5°, in steps of 2.5°. Each column in the plot corresponds to a specific steady TEF input δ_{steady}, and each curve represents a 2/rev input of a specific amplitude δ_{2p} and varying phase ϕ_{2p}. A negative value is beneficial while a positive value means more power requirement.

The best gains are obtained with no steady input, and a phase ϕ_{2p} between 0° and 30°. This corresponds approximately to a negative TEF deflection on the

advancing and retreating sides, and a positive deflection on the front and rear. There is a nose-up pitching moment induced by the TEFs on the advancing side, increasing the lift by reducing the negative angles of attack. Consequently, the front and rear parts of the disk are offloaded due to smaller angles of attack, resulting in net power reduction.

Steady plus 2/rev plus 1/rev TEF input: Fig. 3.9 shows the percentage change in power for the flapped rotor operating at $\mu = 0.3$ and weight coefficient C_W/σ of 0.8 and 0.1 ,from the baseline case (no flaps), with different 1/rev inputs of amplitudes 2.5°, 5° and 7.5° and varying phase angles ϕ_{1p}, imposed on an actuation from Fig. 3.8 that yielded benefits with an addition of 1/rev inputs. The broken horizontal line indicates the power reduction for the baseline with steady+2/rev input in each case.

The 1/rev actuations with the best gains are at a phase ϕ_{1p} between 30° and 90°. This corresponds approximately to a negative TEF deflection on the advancing side and positive on the retreating side, inducing pitching moments that increase the angles (reduce negative angles) on the advancing blade while reducing them on the retreating blade. Overall, there is a modest benefit in combining TEF inputs at different frequencies at this speed. Power reductions of 2.6% at C_W/σ of 0.08 and 1.7% at C_W/σ of 0.1 were observed with the above parametric study.Also, reductions of 1.6% at C_W/σ of 0.07 and 1.3% at C_W/σ of 0.09 (not shown) were observed.

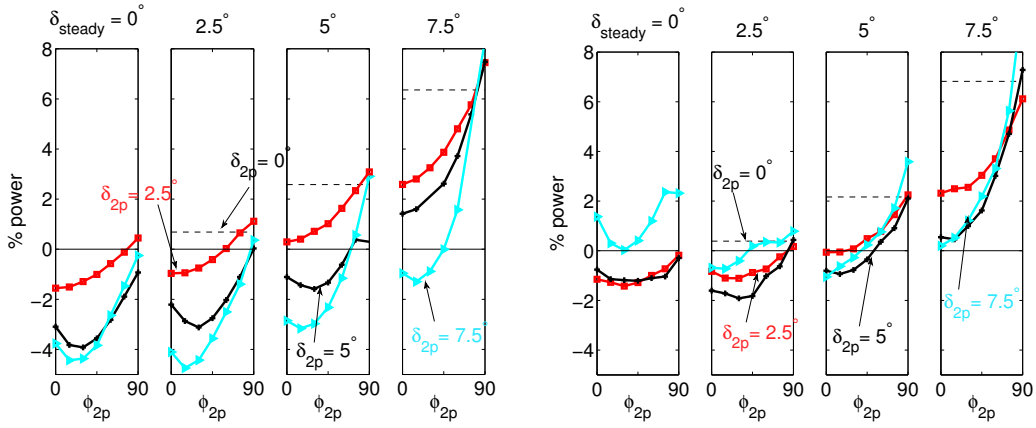

(a) $C_W/\sigma = 0.07$ (b) $C_W/\sigma = 0.085$

Figure 3.10: Effect of 2/rev phasing of TEF (10%R, 15%c, midspan location at 65%R) inputs $\delta = \delta_{steady} + \delta_{2p}\cos(2\psi + \phi_{2p})$ on UH-60A rotor power for different weights; $\mu = 0.4$

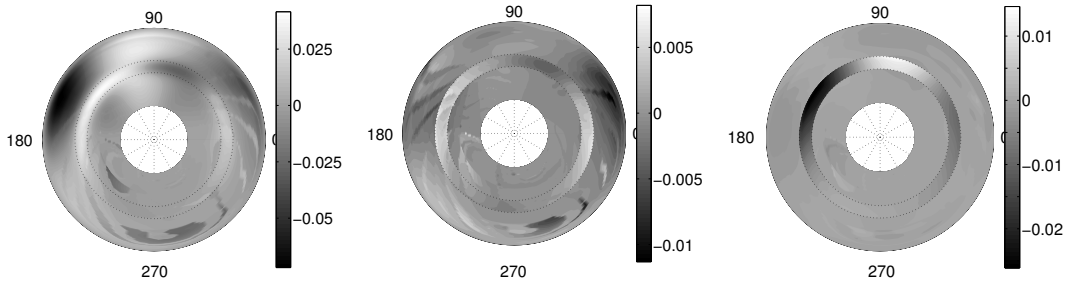

(a) Normal force C_nM^2 (b) Power $-r * C_cM^2$ (c) Pitching moment C_mM^2

Figure 3.11: Change in UH-60A rotor disk loading from baseline rotor, due to 2/rev TEF (10%R, 15%c, midspan location at 65%R) input $\delta = 2.5° + 5°\cos(2\psi + 30°)$; $\mu = 0.4$, $C_W/\sigma = 0.085$; Blue-decrease, Red-increase

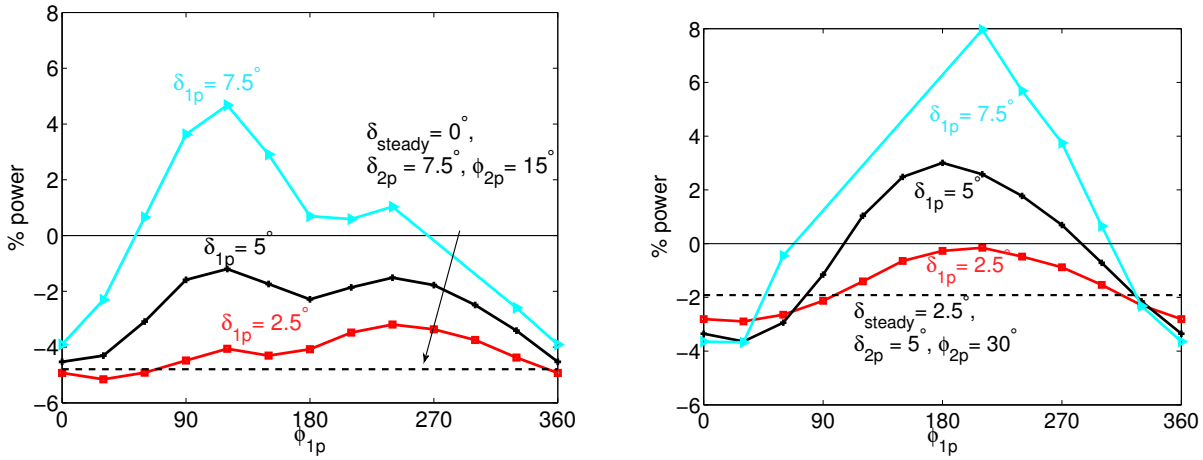

(a) $C_W/\sigma = 0.07$; δ_{steady}=0°,δ_{2p}=5°,ϕ_{2p}=15°

(b) $C_W/\sigma = 0.085$; δ_{steady}=2.5°,δ_{2p}=5°,ϕ_{2p}=30°

Figure 3.12: Effect of 1/rev phasing of TEF (10%R, 15%c, midspan location at 65%R) inputs $\delta = \delta_{steady} + \delta_{1p}\cos(\psi + \phi_{1p}) + \delta_{2p}\cos(2\psi + \phi_{2p})$ on UH-60A rotor power for different weights; $\mu = 0.4$

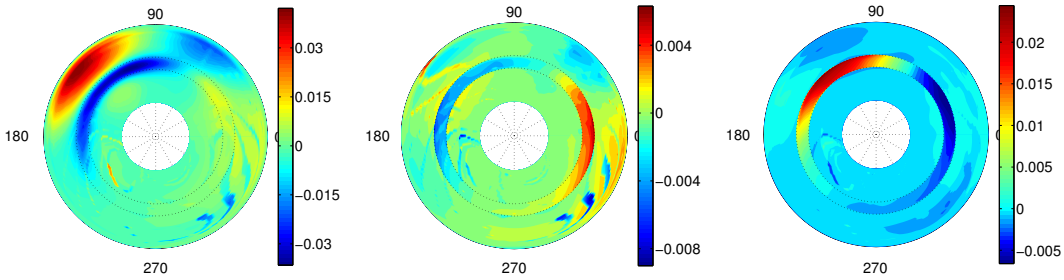

(a) Normal force C_nM^2

(b) Power $-r * C_cM^2$

(c) Pitching moment C_mM^2

Figure 3.13: Change in UH-60A rotor disk loading due to 1/rev TEF (10%R, 15%c, midspan location at 65%R) input $5°\cos(\psi + 30°)$ superimposed on 2/rev input $\delta = 2.5° + 5°\cos(2\psi + 30°)$; $\mu = 0.4$, $C_W/\sigma = 0.085$; Blue-decrease, Red-increase

3.4.2 Case II: Advance ratio $\mu = 0.4$

Steady plus 2/rev TEF input: Fig. 3.10 shows the percentage change in power for the flapped rotor operating at $\mu = 0.4$ and weight coefficient C_W/σ between 0.07

and 0.085 (close to the lift boundary at this speed), from the respective baseline case (no flaps), with different combinations of steady inputs between -2.5° to 7.5° and 2/rev inputs of amplitudes from 0 ° to 7.5°, in steps of 2.5°. Each column in the plot corresponds to a specific steady TEF input δ_{steady}, and each curve represents a 2/rev input of a specific amplitude δ_{2p} and varying phase ϕ_{2p}.

The actuations with the best gains are with a phase ϕ_{2p} between 0° and 30°, as can be seen from Fig. 3.10, but an additional small positive steady deflection is seen to reduce power slightly by reducing the angles further on the front and rear parts of the disk. Negative steady deflections (flap deflected upward) are seen to worsen performance at this speed.

At this high speed condition, the advancing blade is negatively loaded, while the majority of the thrust is generated on the front and rear, which consequently also dominate the contributions to the shaft torque.

The effect of the TEF deployment $\delta = 2.5° + 5°\cos(2\psi + 30°)$ is illustrated as the changes in section aerodynamic loads from the baseline rotor, in Fig. 3.11. There is a nose-up pitching moment induced by the TEFs on the advancing side (Fig. 3.11c), increasing the lift (Fig. 3.11a) by reducing the negative angles of attack. Consequently, the front and rear parts of the disk are offloaded due to smaller angles of attack, resulting in net power reduction (Fig. 3.11b).

Steady plus 2/rev plus 1/rev TEF input: Fig. 3.12 shows the percentage change in power for the flapped rotor operating at $\mu = 0.4$ and weight coefficients C_W/σ of 0.07, 0.08 and 0.085, from the baseline case (no flaps), with different 1/rev inputs of

amplitudes 2.5°, 5° and 7.5° and varying phase angles δ_{1p}, imposed on the best case actuations from Fig. 3.10. The broken horizontal line indicates the power reduction with the base steady+2/rev input in each case. Power reductions of 5.2% at C_W/σ of 0.07, 3.7% at C_W/σ of 0.085 were observed with the above parametric study.

The 1/rev actuations with the best gains are at a phase ϕ_{1p} between 0° and 30°to target the negative loading peak located in the ψ = 90-180° quadrant. The effects of the 1/rev TEF deployment 5°cos(ψ + 30°) superimposed on the 2/rev deployment δ = 2.5°+ 5°cos(2ψ+30°) (from Fig. 3.11) are illustrated as the changes in section aerodynamic loads, in Fig. 3.13. There is a nose-up pitching moment induced by the TEFs on the advancing side, increasing the lift by reducing the negative angles of attack. Consequently, the other parts of the disk are offloaded due to smaller angles, resulting in net power reduction.

Fig. 3.14 shows the percentage change in power with steady, 1 and 2/rev TEF inputs at advance ratios of 0.3 and 0.4, and weight coefficients C_W/σ of 0.08. For example, a flap input of 2.5 + 5° cos(ψ +30°) + 7.5° cos(2 ψ+15°) reduces power requirement by about 3.4% at μ of 0.4 and C_W/σ of 0.08.

However,the same actuation that yields performance benefits also leads to a significant increase in vibration levels,i.e., about 70% in the vibration index J_1, as shown if Fig.3.15 for the same cases as above.J_1 is defined as $J_1 = \mathbf{z}^T W_z \mathbf{z}$, where $\mathbf{z}$ is a vector containing the cosine and sine components of the non dimensional 4/rev fixed system hubloads F_x, F_y ,F_z,M_x, and M_y,and weighting matrix W_z is defined as follows:

The diagonal weighting matrix W_z was assumed to have the form

$$W_z = (1-\beta)\begin{bmatrix} 1/F_{x0}^2 & & & & & \\ & 1/F_{y0}^2 & & & & \\ & & 1/F_{z0}^2 & & & \\ & & & 1/M_{x0}^2 & & \\ & & & & 1/M_{y0}^2 & \end{bmatrix} \tag{3.1}$$

in order to target the hub F_x, F_y, F_z, M_x and M_y. The first three elements are weights for both components of the 3 hub shears and the final two elements are weights for both components of the hub moments. W_θ was assumed to be of the form $W_\theta = \beta I$.

$$W_\theta = \beta I \tag{3.2}$$

In the present study, $\beta = 0$ was used, so the controller attempts to minimize the hub loads without constraining the amplitude of the flap motion.

Fig. 3.16 shows the percentage change in effective rotor L/D due to a combination of steady, 1/rev and 2/rev TEF inputs at advance ratios of 0.3 and 0.4, and weight coefficient C_W/σ of 0.08. Rotor L/D is defined as the ratio of rotor thrust to rotor drag,

$$L/D = \frac{T}{P/V_\infty - D_v}$$

D_v being the vehicle drag. For example, a flap input of $2.5° + 5°\cos\psi + 7.5°\cos(2\psi + 15°)$ improves rotor L/D by about 6.9% at μ of 0.4 and C_W/σ of 0.08.

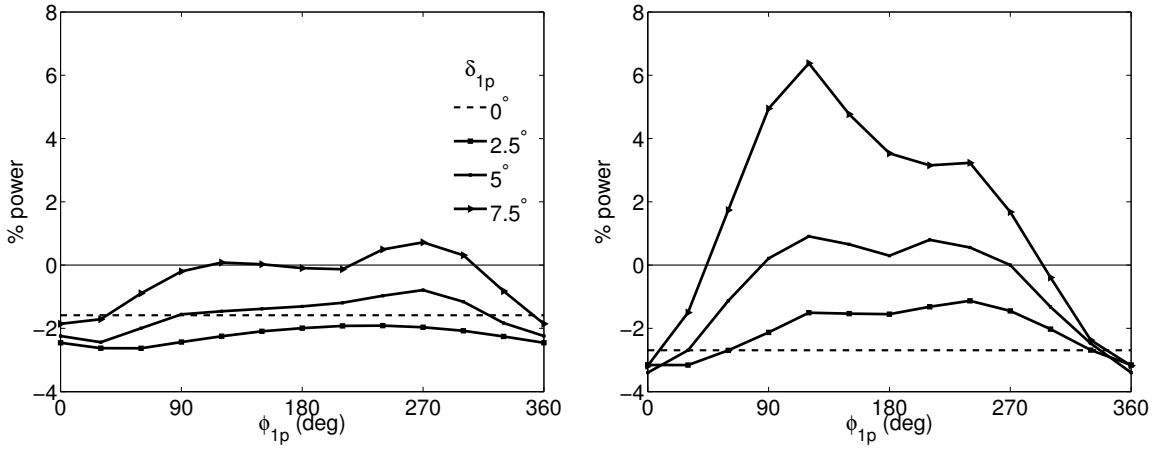

(a) $\mu = 0.3$; $\delta_{steady} = -2.5°$, $\delta_{2p} = 5°$, $\phi_{2p} = 30°$ (b) $\mu = 0.4$; $\delta_{steady} = 2.5°$, $\delta_{2p} = 7.5°$, $\phi_{2p} = 15°$

Figure 3.14: Effect of 1/rev phasing of TEF (10%R, 15%c, midspan location at 65%R) inputs $\delta = \delta_{steady} + \delta_{1p}\cos(\psi + \phi_{1p}) + \delta_{2p}\cos(2\psi + \phi_{2p})$ on UH-60A rotor power for $C_W/\sigma = 0.08$.

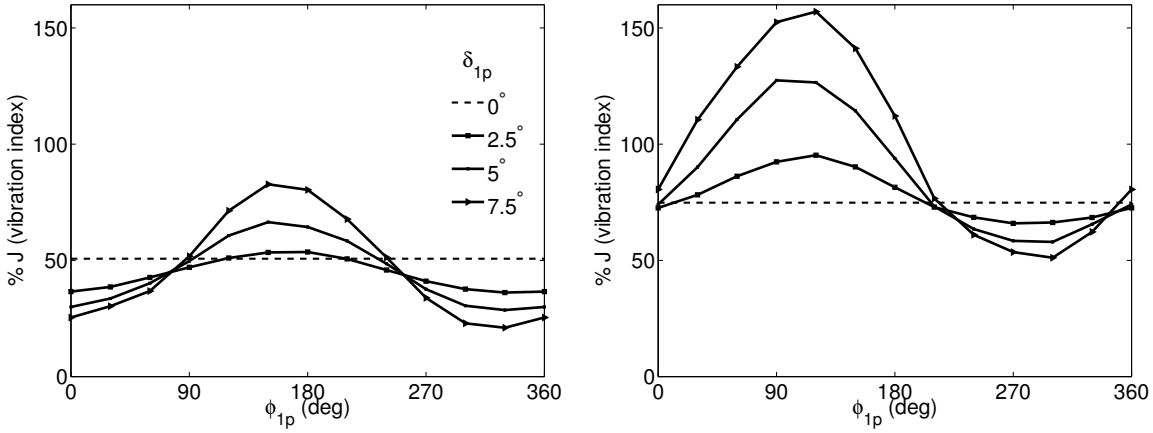

(a) $\mu = 0.3$; $\delta_{steady} = -2.5°$, $\delta_{2p} = 5°$, $\phi_{2p} = 30°$ (b) $\mu = 0.4$; $\delta_{steady} = 2.5°$, $\delta_{2p} = 7.5°$, $\phi_{2p} = 15°$

Figure 3.15: Effect of 1/rev phasing of TEF (10%R, 15%c, midspan location at 65%R) inputs $\delta = \delta_{steady} + \delta_{1p}\cos(\psi + \phi_{1p}) + \delta_{2p}\cos(2\psi + \phi_{2p})$ on vibration index J_1 for UH-60A rotor; $C_W/\sigma = 0.08$.

3.5 Rotor vibration reduction with TEFs : High speed flight condition (C8534) - μ=0.368, C_W/σ=0.0783

This is a high speed, moderate thrust condition, characterized by high vibration levels.

Results obtained for vibration reduction investigated for this flight using TEFs are presented here. The target hub loads were the 4/rev hub longitudinal, lateral and vertical shears, rolling moment and pitching moment (F_x, F_y, F_z, M_x and M_y). The analysis used free-flight trim.

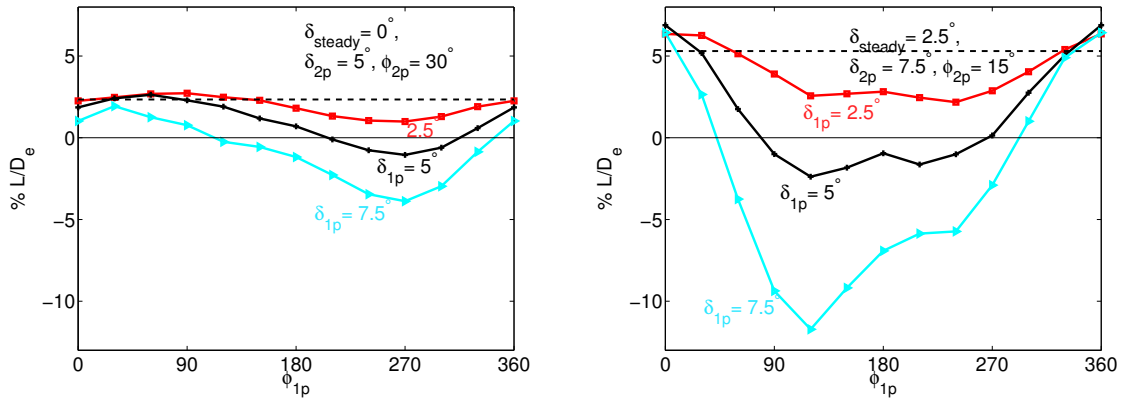

(a) $\mu = 0.3$; δ_{steady}=0°,δ_{2p}=5°,ϕ_{2p}=30°

(b) $\mu = 0.4$; δ_{steady}=2.5°,δ_{2p}=7.5°,ϕ_{2p}=15°

Figure 3.16: Effect of 1/rev phasing of TEF (10%R, 15%c, midspan location at 65%R) inputs $\delta = \delta_{steady} + \delta_{1p}\cos(\psi + \phi_{1p}) + \delta_{2p}\cos(2\psi + \phi_{2p})$ on UH-60A rotor L/D for $C_W/\sigma = 0.08$

3.5.1 Contours of vibratory loads:

The TEF input harmonics used for 4/rev vibration control are 3–5/rev, since these are the frequencies of the rotating frame loads that contribute to the hub loads. Initially, open loop vibration characteristics of the blade with TEFs were examined in order to gain insight into the sensitivity of vibration to various TEF input harmonics, amplitudes and phases. Any one harmonic has different effects

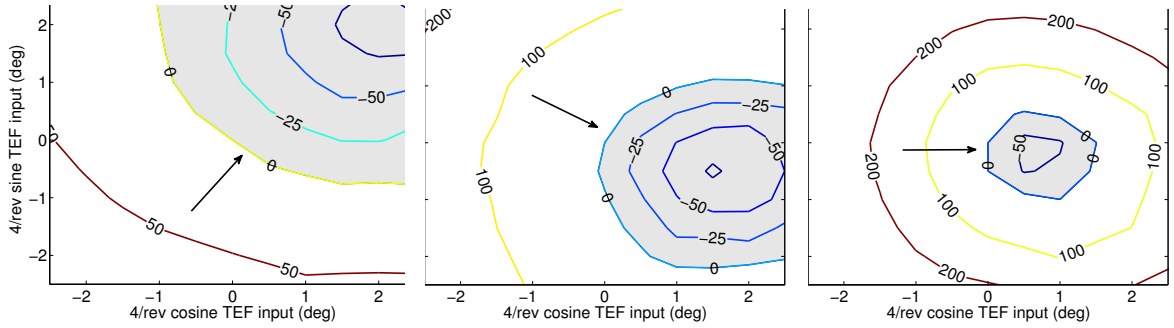

(a) F_x (b) F_y (c) F_z

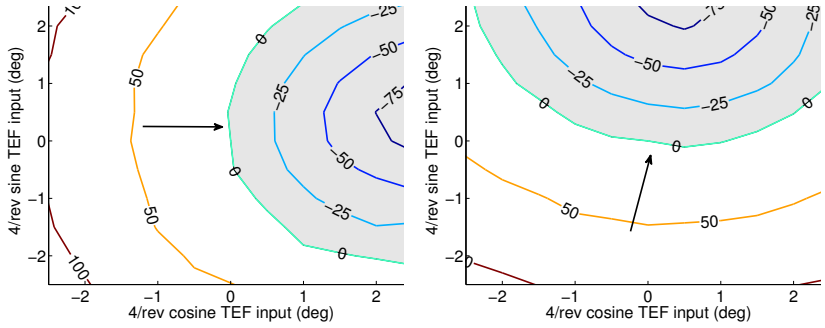

(d) M_x (e) M_y

Figure 3.17: UH-60A 4/rev hub loads with 4/rev TEF inputs; high speed forward flight (C8534: μ=0.368, C_W/σ=0.0783). Values shown are % changes in vibratory amplitude relative to the baseline (no flaps). The highlighted region corresponds to reduction of the respective vibratory load.

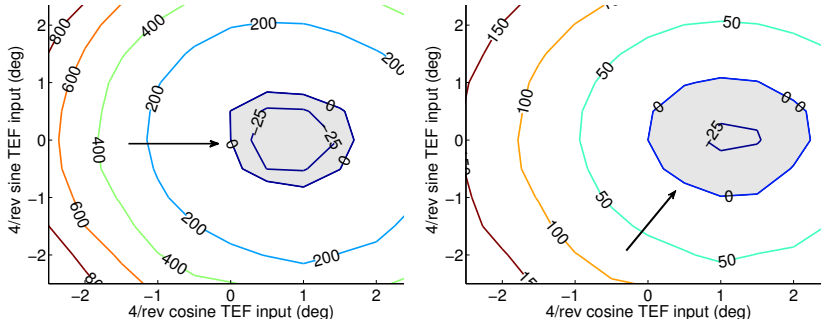

(a) Vibration objective function J_1 (b) Vibration Intrusion Index

Figure 3.18: Vibration objective function J_1 and Vibration Intrusion Index with 4/rev TEF inputs; UH-60A rotor in high speed forward flight (C8534). Values shown are % changes relative to the baseline (no flaps). The highlighted regions correspond to reduction of the respective vibratory index.

on the different vibratory loads. This is illustrated in Fig. 3.17, which maps the % changes in each of the 5 hub loads from the baseline values, as a function of 4/rev sine and cosine TEF deflections. Deflections with sine and cosine components upto $\pm 2.5^\circ$ are shown. Each point corresponds to a particular 4/rev cosine and sine deflection, or equivalently, a particular amplitude and phase of actuation. Each contour line corresponds to a specific value of the % change in the vibratory load from its baseline value, as a result of 4/rev TEF deflections.

It is clear that the specific actuations that cause the largest reductions in any particular load are quite different, and could even lead to an increase in the other loads. Contours of 2 consolidated vibration indices are also plotted in Fig. 3.18 as a % change from the baseline value, due to 4/rev TEF deflections. The indices are as follows:

1. Index J_1:

   $J_1 = \mathbf{z}^T \; W_z \; \mathbf{z}$

2. Index J_2: A load-based Vibration Intrusion Index, defined only using the 4/rev non-dimensional vibratory shears, a $\sqrt{(0.5\ F_x)^2 + (0.75\ F_y)^2 + F_z^2}$, assigning weights to the 3 shears as per the ADS-27A standard,

where $\mathbf{z}$ is a vector containing the cosine and sine components of the non-dimensional N_b/rev fixed system hub loads F_x, F_y, F_z, M_x and M_y, and the weighting matrix W_z is defined in Equation (1).

This procedure was used to estimate the actuations at individual harmonics for reduction of different target loads, and the multicyclic feedback controller methodology was validated by comparing its predictions with those obtained from the parametric studies. All subsequent results for vibration reduction were obtained by applying the multicyclic control algorithm.

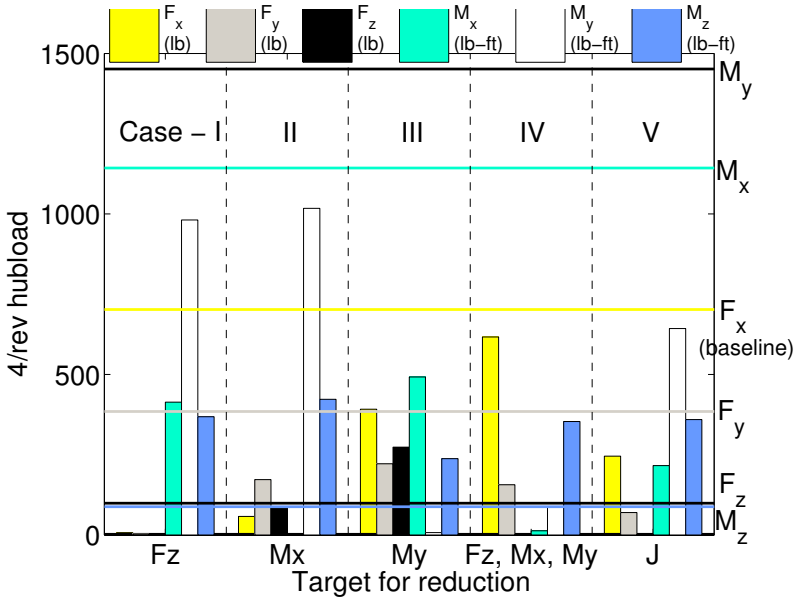

Figure 3.19: UH-60A rotor baseline (no flap) and reduced 4/rev vibratory loads for different targets for reduction using the multicyclic control algorithm; high speed forward flight (C8534). F_x: longitudinal shear, F_y: lateral shear, F_z: vertical shear, M_x: rolling moment, M_y: pitching moment, J: target F_x, F_y, F_z, M_x and M_y. The horizontal lines indicate the baseline vibratory hub loads (uncontrolled).

3.5.2 Multicyclic Controller - different targets:

It was possible to reduce the vibration objective function by upto 80% using a combination of 3–5/rev flap inputs. As an illustration of the working of the multicyclic algorithm, four cases were considered. The first three cases used the algorithm to minimize a single load (F_z - case 1, M_x - case 2, M_y - case 3), the fourth case targeted F_z, M_x and M_y alone and the fourth case targeted all three hub shears and rolling and pitching moments, corresponding to the objective function J defined earlier, simultaneously. Figure 3.19 shows the changes obtained in the six hub loads

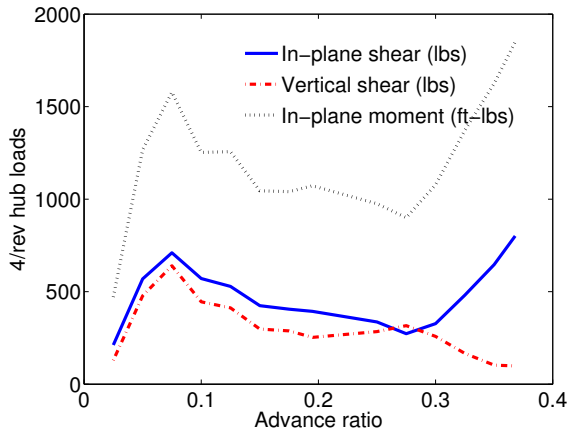

(a) Baseline 4/rev hub loads

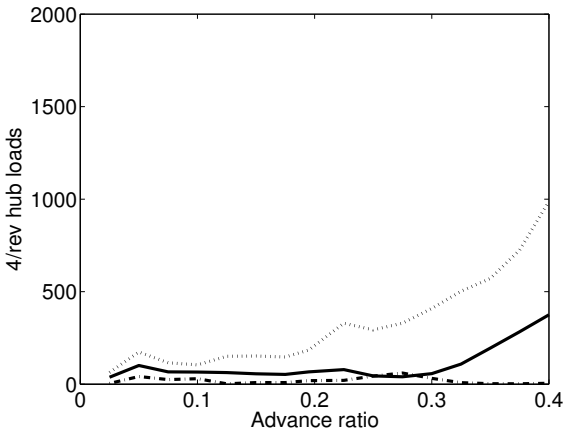

(b) Reduced(with TEFs) 4/rev hub loads

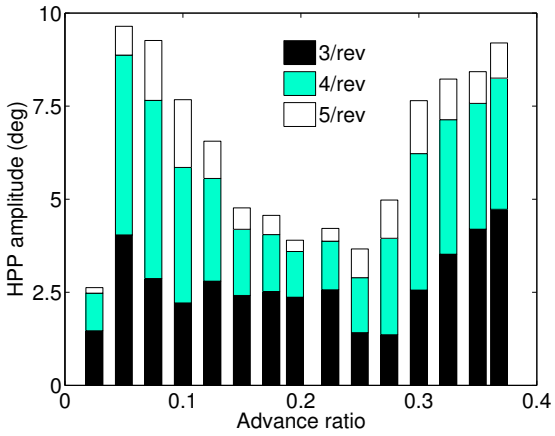

(c) HPP optimal TEF deflections for vibration reduction

Figure 3.20: UH-60A rotor baseline (no flap) vibratory loads and optimal TEF actuation amplitudes for various speeds; moderate thrust forward flight (Flight 85), C_W/σ=0.0783

F_x, F_y, F_z, M_x, M_y and M_z in each of these five cases. The horizontal lines represent the levels of the baseline vibratory hub loads. The five targets of reduction, namely F_z, M_x, M_y, all three and vibration objective function J, are along the x-axis, and the values of the six vibratory hub loads with the optimal actuation in each case

constitute the five bars.

This figure shows that a reduction in a particular hub load may be accompanied with an increase in the other hub loads. For instance, targeting only M_y (case 3) resulted in near-100% reduction of M_y, but there were only modest reductions in the levels of F_y, F_z and M_x. It also indicates that some loads are more sensitive to small TEF deflections than others. The results that follow target the vibration index J (hub loads F_x, F_y, F_z, M_x and M_y) for reduction.

3.5.3 Vibration reduction at various speeds:

The TEF is capable of vibration suppression at different flight speeds, requiring higher deflections in the high vibration regimes. The highest vibrations occur at transition speeds and at high speeds, as shown in the overall vibratory levels indicated by the hub in-plane shear ($\sqrt{{F_x}^2 + {F_y}^2}$), vertical shear F_z and in-plane moment ($\sqrt{{M_x}^2 + {M_y}^2}$), as shown in Fig. 3.20a, for a constant weight coefficient C_W/σ=0.0783 (termed Flight 85). Flight C8534 corresponds to the highest speed in this case. High-speed vibration is due to unsteady pitching moments, which cause large elastic twist deformations. Low speed vibration, on the other hand, is caused by blade-vortex interactions. Figure 3.20c shows the flap actuation amplitudes required to suppress combined F_x, F_y, F_z, M_x and M_y at different forward speeds. The fractions of the actuations corresponding to the individual frequencies (3, 4 and 5/rev) are indicated as well.

High thrust flight condition (C9017): μ=0.237, C_W/σ=0.1325

This is a high altitude, high thrust flight condition used to study dynamic stall events. First, vibration reduction for C9017 flight condition using TEFs is addressed. Then, the effect of 1 and 2/rev TEF inputs on power is discussed, and inputs for dynamic stall alleviation are presented. Finally, the possibility of combining benefits in vibration, power and stall is explored.

Vibration reduction

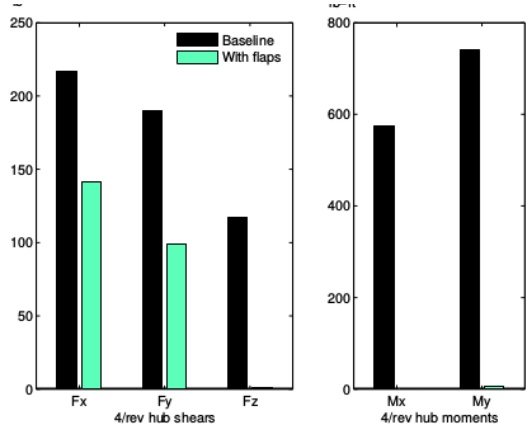

Figure 3.21: UH-60A rotor baseline (no flap) and reduced vibratory loads; high thrust forward flight (C9017: μ=0.237, C_W/σ=0.1325). F_x: longitudinal shear, F_y: lateral shear, F_z: vertical shear, M_x: rolling moment, M_y: pitching moment. The loads targeted for reduction were F_z, M_x and M_y.

The target hub loads were, as before, the 4/rev hub vertical shear, rolling moment and pitching moment (F_z, M_x and M_y). Fig. 3.21 shows a comparison of the baseline and reduced vibratory load levels. The optimal HPP TEF amplitude

for vibration reduction was 3°.

3.5.4 Effect of torsional stiffness on vibration reduction:

A torsionally softer blade was earlier shown to improve performance at hover. In order to determine if reducing the blade torsional stiffness leads to smaller flap actuation requirements for vibration suppression at C8534, the torsional stiffness of the blade was reduced by up to 50% and the optimal actuation requirements in each hypothetical case were estimated.

Fig. 3.22 shows the baseline loads and reductions obtained with the optimal flap actuations, for blades of different torsional stiffnesses. The baseline vibrations (uncontrolled) increase steadily with a reduction in blade stiffness. This can be explained by examining the rotating and fixed frame loads, and the natural response characteristics of the blade, as stiffness is reduced. Fig. 3.23 shows the 3, 4 and 5/rev components of the blade root shears f_x, f_y and f_z, and torsion and flapwise bending moments m_x and m_y. The 3/rev component is clearly the most dominant one, and increases as the torsional stiffness is reduced. Indeeed, the blade response, particularly the elastic twist, contains a large 3/rev component which increases for the softer blades. The blade 1st torsion frequency approaches 3/rev as the torsion stiffness is reduced. Consequently, the 3/rev components of the blade response and section loads increase rapidly, resulting in larger 4/rev hub loads (Fig. 3.22).

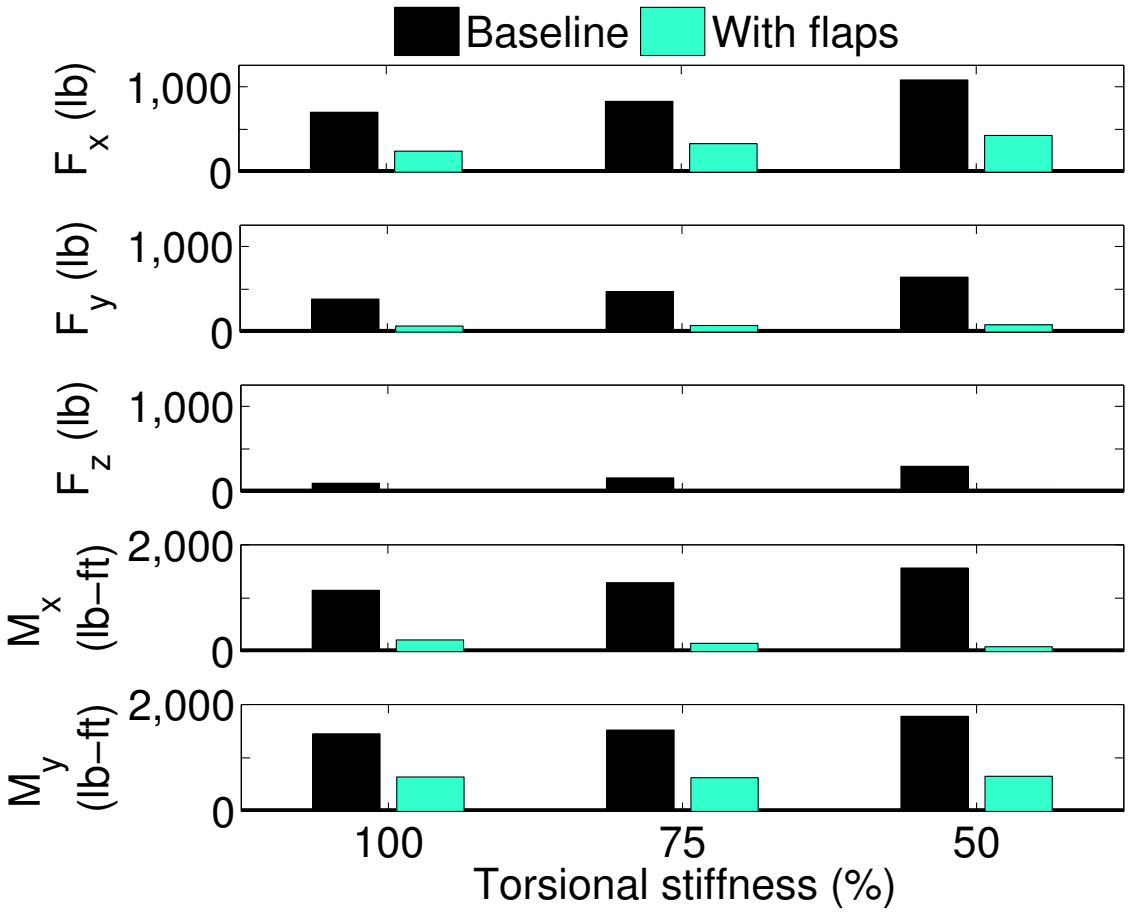

Figure 3.22: UH-60A rotor baseline (no flap) and reduced vibratory loads for different blade torsional stiffnesses (GJ); high speed forward flight (C8534). F_x: longitudinal shear, F_y: lateral shear, F_z: vertical shear, M_x: rolling moment, M_y: pitching moment. The loads targeted for reduction were F_x, F_y, F_z, M_x and M_y.

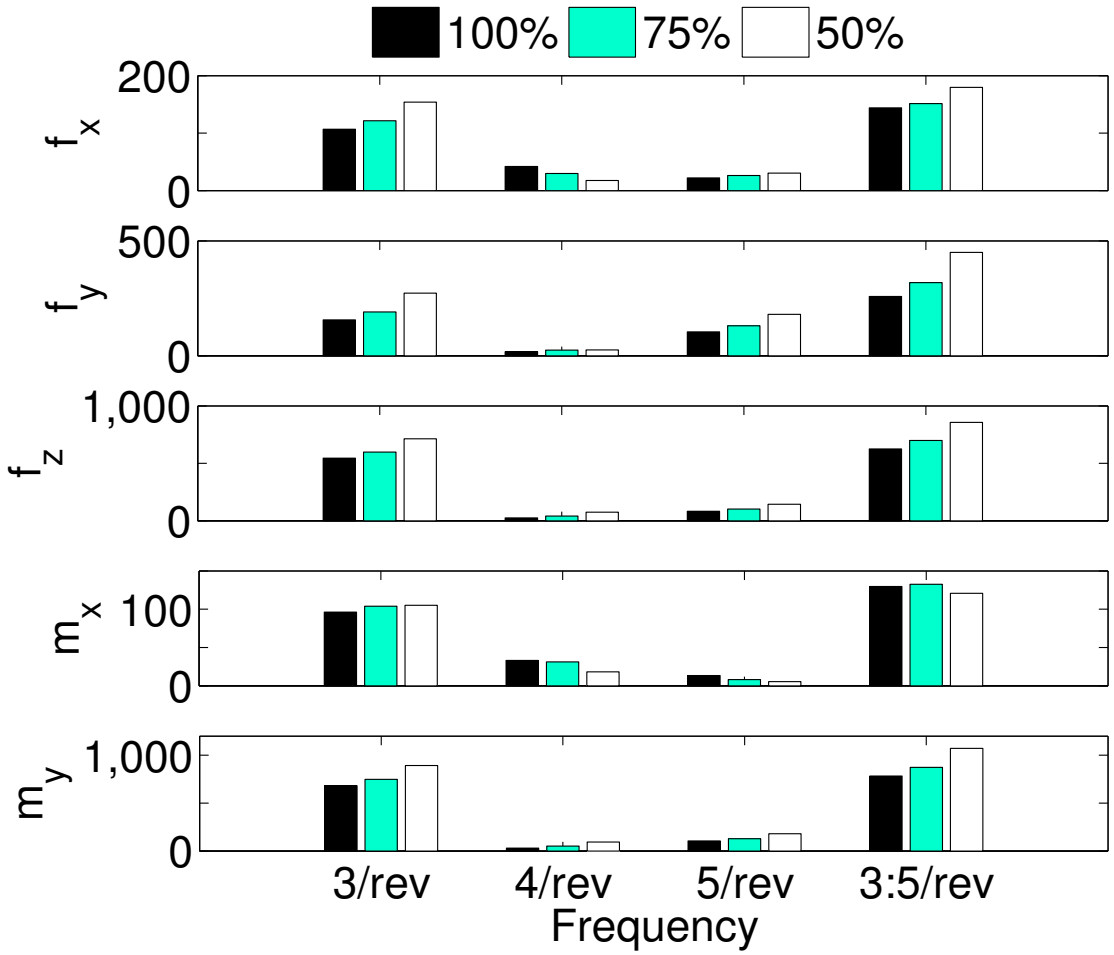

Figure 3.23: Components of UH-60A rotor baseline (no flap) HPP blade root loads for different blade torsional stiffnesses (GJ); high speed forward flight (C8534). f_x: lateral shear, f_y: longitudinal shear, f_z: vertical shear, m_x: torsion bending moment, m_y: flapwise bending moment

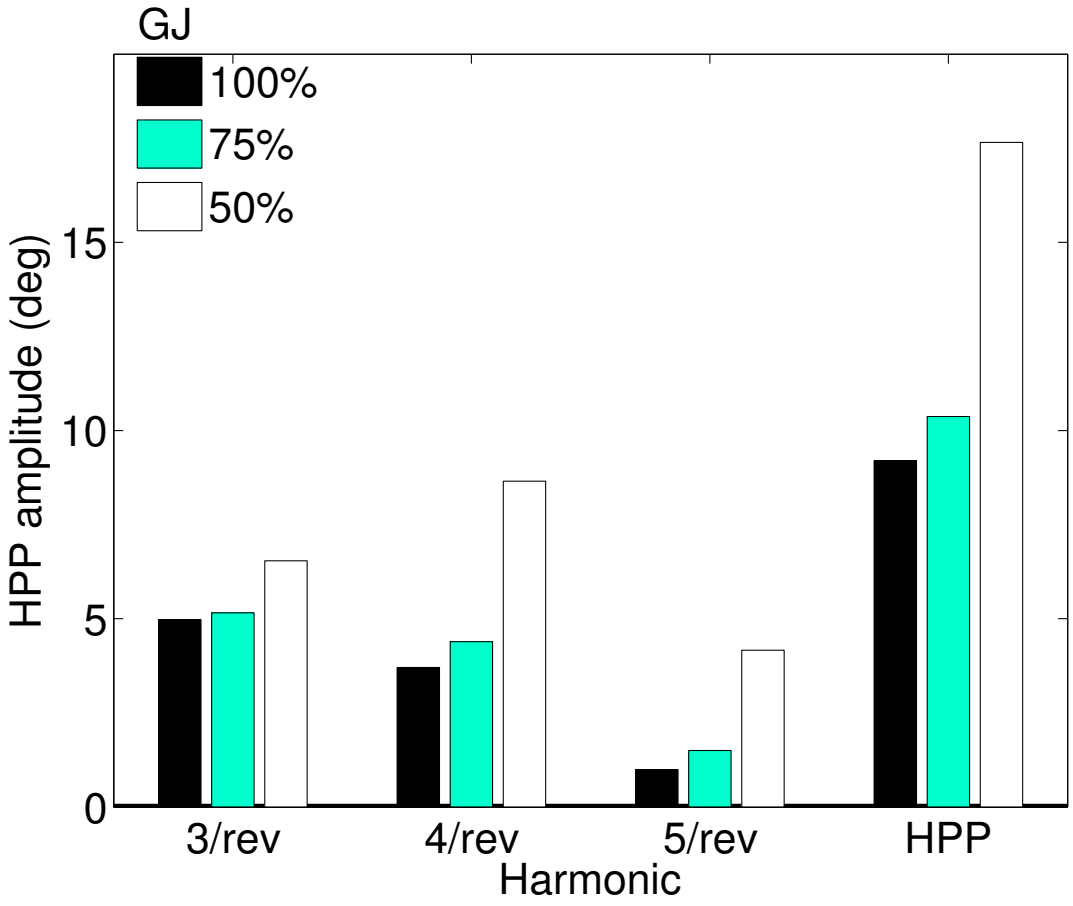

Figure 3.24: Flap deflection amplitudes for UH-60A vibration reduction for different blade torsional stiffnesses (GJ); high speed forward flight (C8534). HPP: half peak-to-peak amplitude of optimal actuation

Hence, any improvements in the effectiveness of the flap at altering the twist response with torsionally softer blades were offset by the increase in the baseline vibratory loads themselves, resulting in larger flap deflection requirements for vibration control. Milgram and Chopra ([91]) also reported a decrease in vibration reduction effectiveness with a reduction in blade torsional stiffness. Fig. 3.24 compares the TEF amplitudes of the 3–5/rev and combined HPP (Half Peak-to-Peak) flap deflections obtained from the optimization procedure, for blades of different torsional stiffnesses. These are the optimal actuations used to obtain the vibration reduction shown in Fig. 3.22. The 3/rev deflection component is the largest, due to the frequency distribution of the blade loads.

3.5.5 Effect of not using 5/rev TEF inputs for vibration reduction:

The 5/rev component of the actuation is small compared to 3 and 4/rev for the baseline (100% GJ) blade. It is desirable to avoid high frequency actuations from a practical standpoint. Therefore, the potential vibration reduction with only 3 and 4/rev deflections was determined using the multicyclic control methodology. Figure 3.25 shows the baseline and reduced vibratory loads and optimal control actuations for vibration control with 3–5/rev and only 3 and 4/rev inputs. The target loads were F_z, M_x and M_y. From Fig. 3.25a, the reductions in the target loads were still appreciable (99% in F_z, 85% in M_x and 91% in M_y), although the hub moments were reduced to a slightly smaller extent. This is expected, since the 3 and 5/rev components of the root bending moments contribute to the 4/rev vibratory hub moments, and the 5/rev TEF input is necessary to target the 5/rev blade loads. Nevertheless, this demonstrates that it is possible to achieve large reductions in vibration without the high frequency 5/rev TEF inputs.

3.5.6 Stall alleviation with TEFs - 'down-only' 1/rev TEF inputs

TEFs excited at a suitable phasing and amplitude can reduce the magnitude of dynamic stall events occurring in high thrust forward flight. Thus, it is possible to push the rotor operational envelope to higher operational thrust levels using trailing-edge flaps. To this end, 1/rev flap inputs (hereafter referred to as "down-only" 1/rev inputs) were prescribed to the TEF, chosen so that the flap deflection is maximum on the retreating side, ensuring reductions in section angles of attack due to the

increased nose-down pitching moment, and as small as possible on the advancing side, for minimum drag penalties. The general form of the actuation was $\delta = \delta_0 + \delta_0 \cos(\psi - \phi)$. Note that an actuation of this type attains its maximum positive (downward) TEF deflection at an azimuth equal to ϕ. It was found that with such a deployment, it is possible to reduce the stall loads and achieve power reductions simultaneously. Fig. 3.26a shows the normal force and pitching moment at select radial sections for the baseline C9017 case and with actuations of $3° + 3°\cos(\psi - 270°)$ and $5° + 5°\cos(\psi - 270°)$. The pitching moment stall events outboard of $80\%R$ are reduced with the down-only TEF deployment (see Fig. 3.26b).

The metric used to quantify the stall level, C_{Tors}, is defined as the HPP higher harmonic ($\geq$4/rev) blade root torsional moment (m_x), since dynamic stall is characterized by a sudden increase in airfoil nose-down pitching moment, affecting the

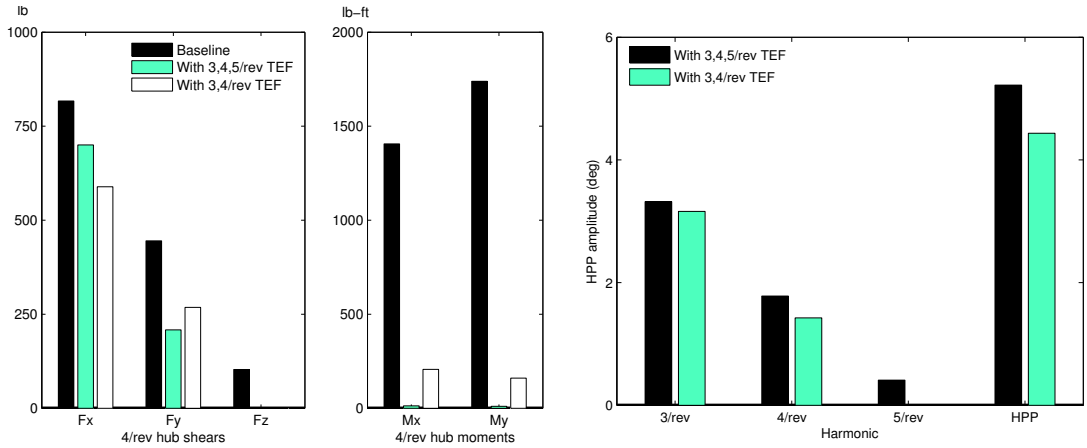

(a) Baseline (no flap) and reduced 4/rev hub loads (b) Optimal TEF deflections for vibration reduction

Figure 3.25: Comparison of UH-60A vibration reduction obtained with 3–5/rev TEF deflections and only 3 and 4/rev deflections; high speed forward flight (C8534)

blade torsional loads. Fig. 3.26 shows the reduction in the rotor power and stall loads, with down-only 1/rev TEF inputs of amplitudes 1°, 3° and 5°, from the baseline C9017 value. The inputs are shown in terms of the azimuth ϕ at which the maximum downward flap deflection is attained. In general, the inputs phased to attain their peak downward deflections on the retreating side yield the best reductions in the stall metric, while power reductions of the order of 7-8% were achievable with a HPP amplitude of 5°. For example, a down-only TEF input of amplitude 5° and attaining a maximum at 270° azimuth, reduces the stall metric by about 45%, power by about 7.6% and allows the rotor to operate at a 5% higher thrust, which would normally not be achievable due to stall-related losses.

Fig. 3.28 shows the vibratory hub loads with down-only 1/rev TEF inputs of amplitudes 1°, 3° and 5°. These inputs do not affect vibration adversely, even causing reductions in the vibratory loads.

3.6 Simultaneous power, vibration and stall reduction with 'down-only' 1/rev TEF inputs: High thrust flight condition(C9017)

Fig. 3.27a shows the actuations required for vibration and power reduction, with a down-only 1/rev input amplitude of 5°, at the optimum phase of 270°. The HPP actuation requirement for vibration reduction is 3.0° for the baseline case and 2.5° with the 1/rev input. The net actuation HPP amplitude is 6.6°, yielding a 7.5% reduction in power and 42% in C_{Tors}/σ from baseline C9017, in conjunction with reductions in all three 4/rev hub shears and the hub 4/rev roll and pitch moments

(31% in F_x, 82% in F_y, 83% in F_z, 87% in M_x and 83% in M_y). The amplitudes of each of the input harmonics: 1, 3, 4 and 5/rev, are shown in Fig. 3.27b.

This demonstrates that the TEF is capable of vibration control as well as performance improvement, combining stall mitigation and power reduction at high thrust conditions.

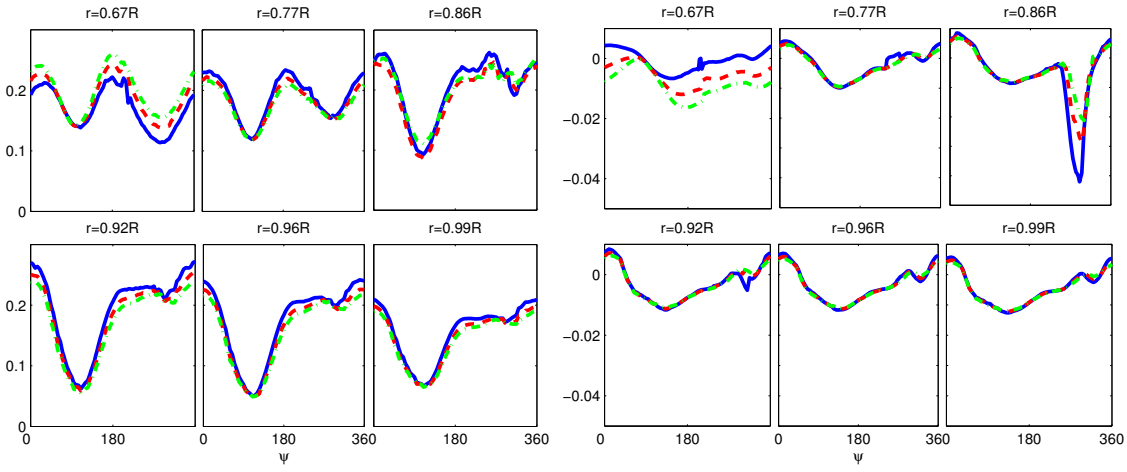

(a) Section normal force

(b) Section pitching moment

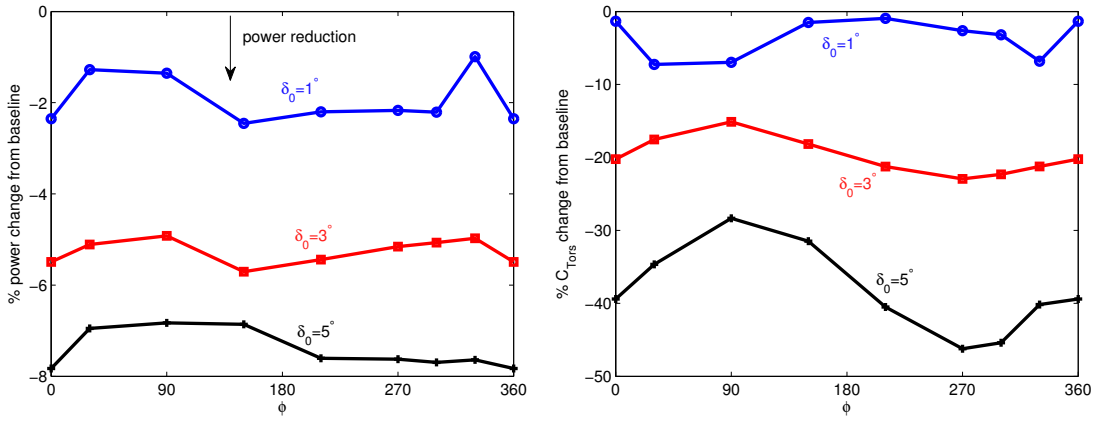

(a) Power (b) C_{Tors}/σ

Figure 3.26: Effect of phasing of down-only 1/rev TEF inputs $\delta = \delta_0 + \delta_0 \cos(\psi - \phi)$ on UH-60A rotor power and stall metric C_{Tors}; high thrust forward flight (C9017). ϕ is thus the azimuth for maximum positive (downward) TEF deflection.

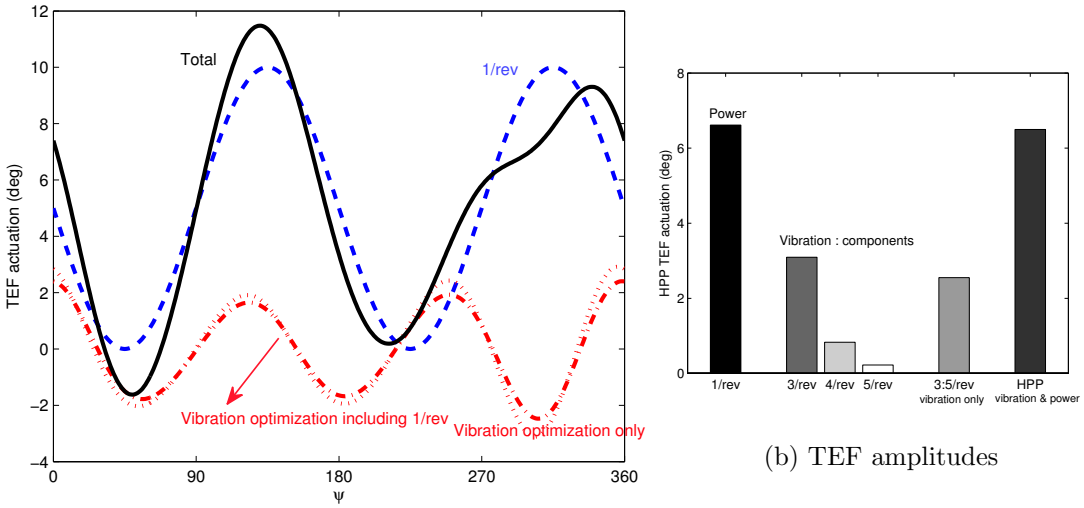

(a) TEF actuations (b) TEF amplitudes

Figure 3.27: TEF actuation combining inputs for UH-60A power, vibration and stall reduction; high thrust forward flight (C9017). The individual components for vibration reduction and power/stall reduction are also shown.

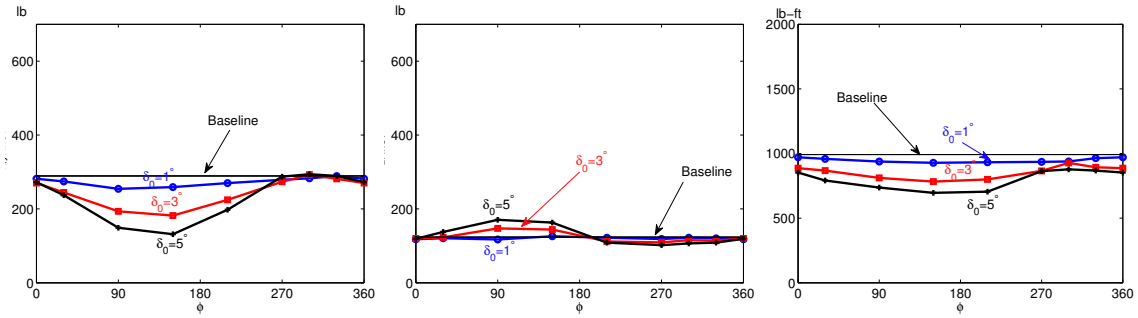

(a) 4/rev hub in-plane shear (b) 4/rev hub vertical shear (c) 4/rev hub in-plane moment

Figure 3.28: Effect of phasing of down-only 1/rev TEF inputs $\delta = \delta_0 + \delta_0 \cos(\psi - \phi)$ on UH-60A vibratory loads; high thrust forward flight (C9017). ϕ is thus the azimuth for maximum positive (downward) TEF deflection.

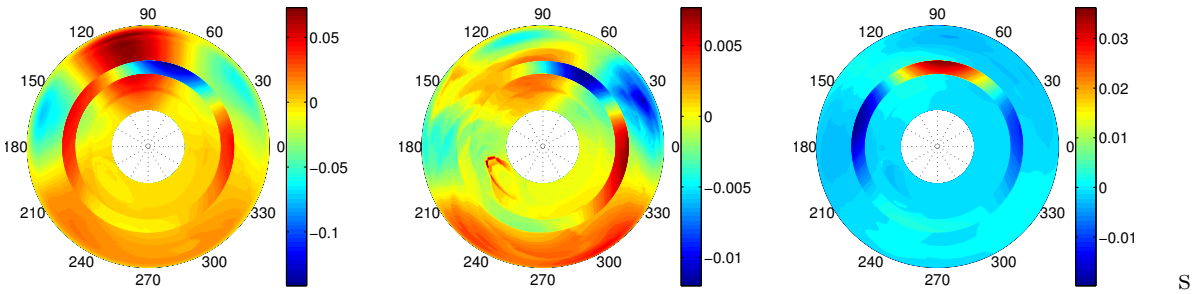

(a) Lift (b) Drag (c) Pitching moment (positive nose up)

S

Figure 3.29: Change in UH-60A rotor disk loading from baseline, due to 2/rev TEF input $\delta = 5°\cos(2\psi + 15°)$; high speed forward flight (C8534); Blue-decrease, Red-increase

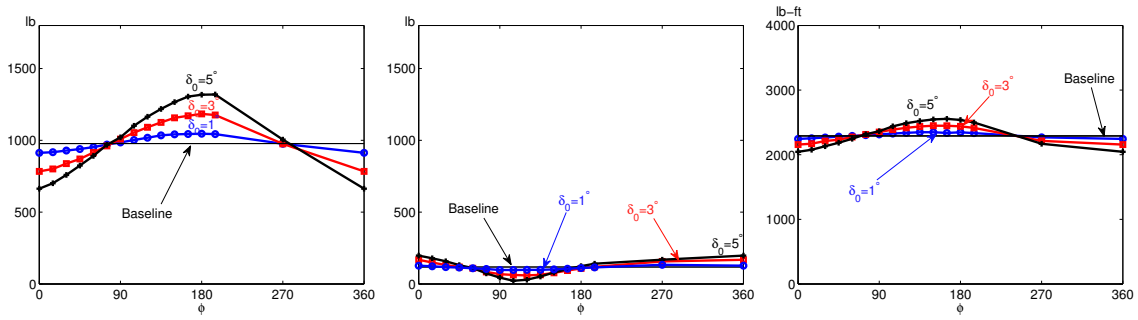

(a) 4/rev hub in-plane shear (b) 4/rev hub vertical shear (c) 4/rev hub in-plane moment

Figure 3.30: Effect of phasing of 1/rev TEF inputs $\delta = \delta_0 \cos(\psi + \phi)$ on UH-60A vibratory loads; high speed forward flight (C8534)

3.7 Power reduction with 1,2/rev TEF inputs:High speed flight condition (C8534)

Fig. 3.29 shows the rotor disk loading with the flap actuated at $\delta = 5°\cos(2\psi + 15°)$, in terms of the change in the section aerodynamic loads from the baseline C8534 condition. The baseline condition has the advancing blade operating at negative angles of attack. The TEF causes nose-up pitching moments and twist on the advancing blade, increasing the angles of attack in the sections producing negative lift. Thus the advancing side produces more lift without an associated drag penalty. The other parts of the disk are offloaded slightly and their drag contribution is reduced.

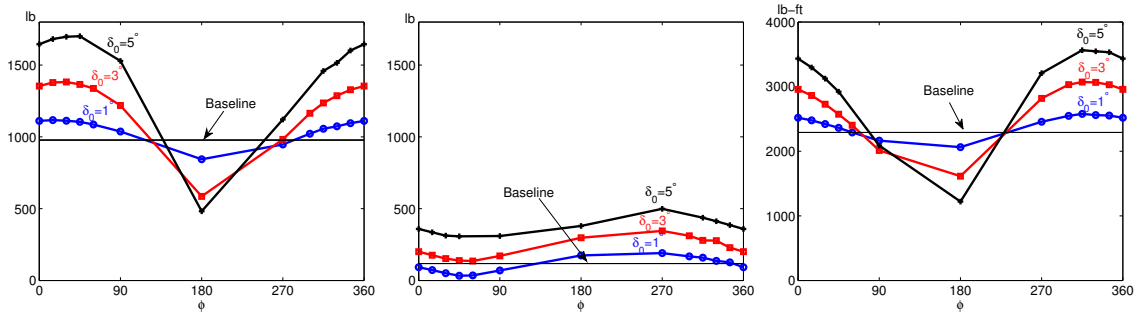

(a) 4/rev hub in-plane shear (b) 4/rev hub vertical shear (c) 4/rev hub in-plane moment

Figure 3.31: Effect of phasing of 2/rev TEF inputs $\delta = \delta_0 \cos(2\psi + \phi)$ on UH-60A vibratory loads; high speed forward flight (C8534)

Note that the 1/rev inputs with power benefits do not have a significant adverse effect on the vibratory loads (4/rev hub in-plane and vertical shears, and in-plane moment), as seen in Fig. 3.30. The baseline vibration levels are indicated by the

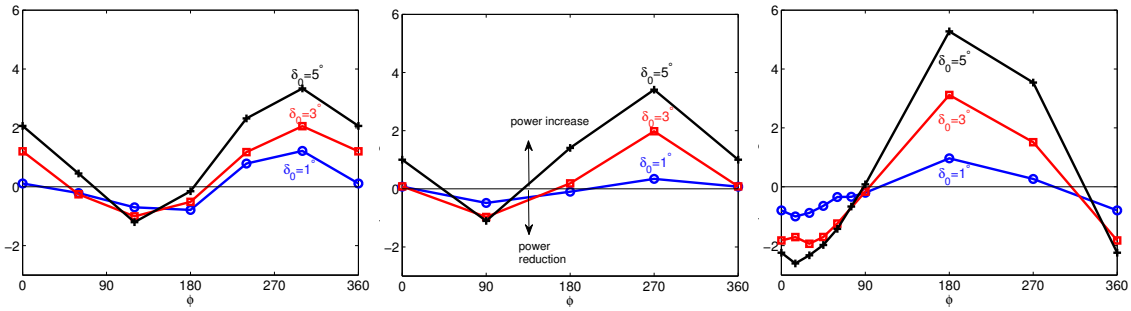

(a) $\mu = 0.1$ (b) $\mu = 0.2$ (c) $\mu = 0.3$

Figure 3.32: Effect of phasing of 2/rev TEF inputs $\delta = \delta_0 \cos(2\psi + \phi)$ on UH-60A rotor power (% change from baseline); moderate thrust forward flight (Flight 85), C_W/σ=0.0783

horizontal lines. However, the 2/rev deflections that result in performance gains affect the vibration levels adversely, as seen in Fig. 3.31. Of the target loads, F_z in particular increases by a large fraction of the baseline value.

Therefore, 2/rev TEF deployment has power benefits at the C8534 condition. However, it also has a negative effect on the vibration levels. A performance improvement that worsens vibration is less desirable, hence one of the goals of this study is to ascertain if the TEF is capable of yielding a net performance improvement while also reducing vibration. This shall be discussed in the following section. The mechanism for power reduction with 2/rev TEF inputs at high forward speeds is to affect the loading on the advancing disk producing negative lift. However, at lower speeds, there is little or no negative loading, so the mechanism of any power reductions effected by the TEF is expected to be different. Figure 3.32 shows the % change in power from the respective baselines, for the rotor operating at a weight coefficient C_W/σ of 0.0783 (termed Flight 85), and advance ratios of 0.1, 0.2 and

0.3. At lower forward speeds, the optimum phasing of the TEF input moves towards increasing the loading on the front and rear parts of the disk i.e. towards a phase of $\phi = 180°$.

Power reduction with 1, 2/rev harmonic TEF inputs

C9017 was investigated for possible power reductions using 1 and 2/rev TEF deflections. Actuation schedules of the form $\delta = \delta_0 \cos(n\psi + \phi)$, $n = 1, 2$, for varying amplitudes and phases ϕ were prescribed to the flap defined in Table 2.1. Fig. 3.33 shows the percent change in power for the flapped rotor operating at C9017, from the baseline case (no flaps), with 1 and 2/rev inputs, respectively. It is clear that the performance gains with flap amplitudes upto 5° are less than half (maximum gains of the order of 1% reduction in power) compared to the high speed C8534 condition. This is because there are no sections of the disk producing negative lift, hence the power reductions (with 2/rev TEF inputs) occur due to offloading of the advancing and retreating blades and there is not a significant improvement in the section L/Ds on the advancing side, as was identified for high-speed flight.

The 1/rev inputs with power benefits do not have a significant adverse effect on the vibratory loads (4/rev hub in-plane and vertical shears, and in-plane moment), as seen in Fig. 3.34. The baseline vibration levels are indicated by the horizontal lines. However, the 2/rev deflections that result in performance gains affect the vibration levels adversely, as seen in Fig. 3.35.

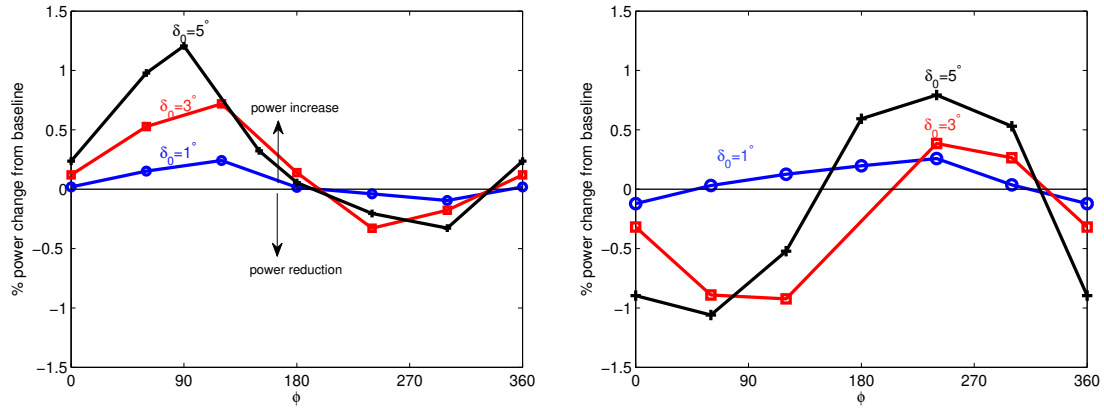

(a) 1/rev TEF inputs ($n = 1$): $\delta = \delta_0 \cos(\psi + \phi)$ (b) 2/rev TEF inputs: $\delta = \delta_0 \cos(2\psi + \phi)$

Figure 3.33: Effect of phasing of 1 and 2/rev TEF inputs on UH-60A rotor power; high thrust forward flight (C9017)

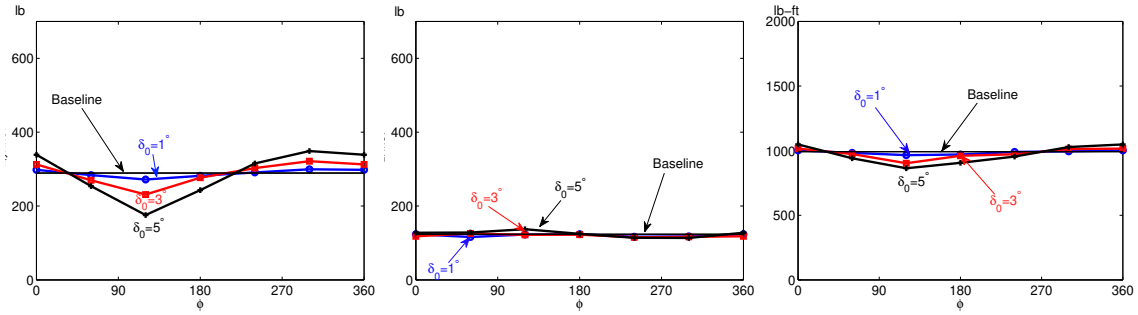

(a) 4/rev hub in-plane shear (b) 4/rev hub vertical shear (c) 4/rev hub in-plane moment

Figure 3.34: Effect of phasing of 1/rev TEF inputs $\delta = \delta_0 \cos(\psi + \phi)$ on UH-60A vibratory loads; high thrust forward flight (C9017)

3.8 Simultaneous power and vibration reduction with TEFs : High speed flight condition (C8534)

It was observed that it was possible to reduce vibratory loads with suitable 3–5/rev TEF deflections, while suitable combinations of steady, 1/rev and 2/rev

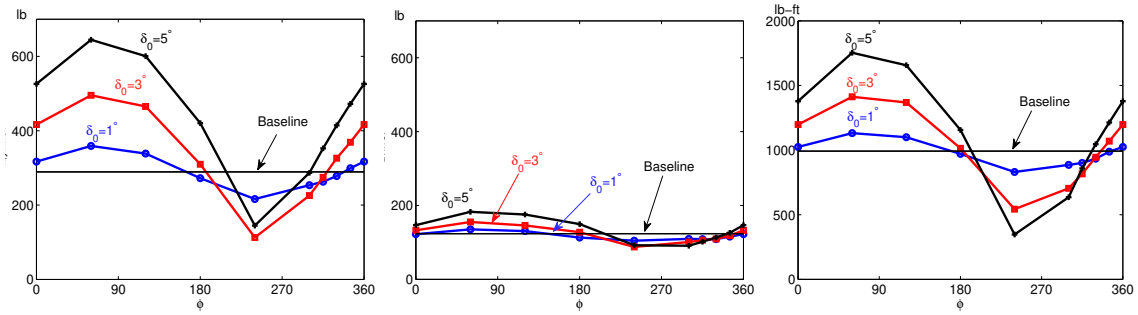

(a) 4/rev hub in-plane shear (b) 4/rev hub vertical shear (c) 4/rev hub in-plane moment

Figure 3.35: Effect of phasing of 2/rev TEF inputs $\delta = \delta_0 \cos(2\psi + \phi)$ on UH-60A vibratory loads; high thrust forward flight (C9017)

deflections yielded power reductions. However, a reduction of power consumption is accompanied by an increase in vibration, while the flap actuations for vibration reduction increase the power requirements. Hence, revised actuations are necessary for reducing the vibration that comes with power benefits.

For the purpose of this discussion, the C8534 high speed flight condition is considered. From a parametric sweep of different steady and 2/rev inputs, the actuation $3° \cos(2\psi + 30°)$ was chosen and 1/rev inputs of amplitude 3° were superimposed on this actuation for further power reduction.

Figs. 3.36 and 3.37 summarize the power and vibration benefits as a function of the phase ϕ_{1p} of the 1/rev input. Fig. 3.36 shows the changes in power effected by (i) only 1/rev inputs of amplitude 3° superimposed on the actuation $3° \cos(2\psi+30°)$, (ii) superimposition of 1, 2/rev inputs on the baseline optimal actuation for vibration reduction only and (iii) combination of 1, 2/rev inputs and the revised optimal actuation for vibration reduction. The actuation for vibration reduction only results

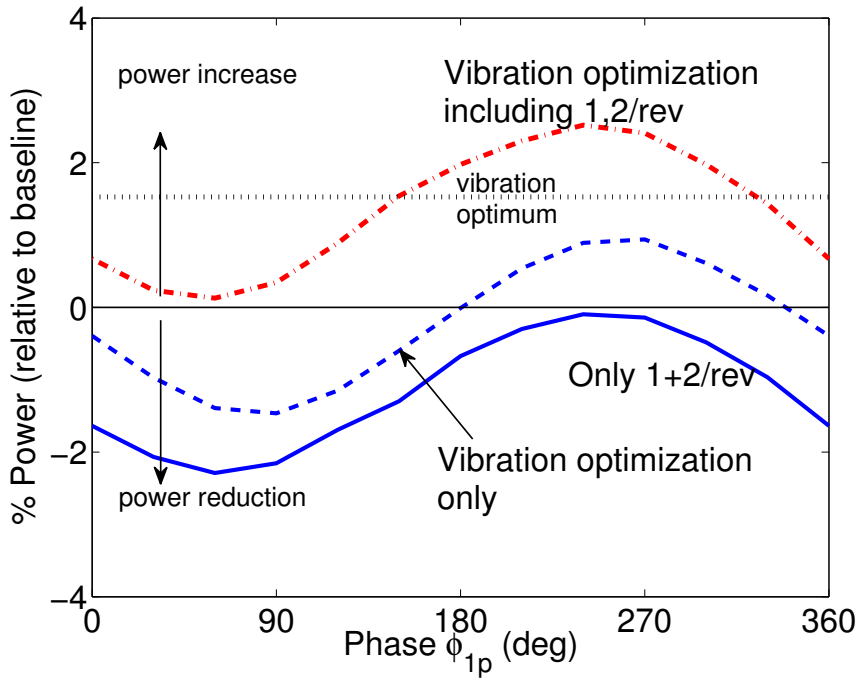

Figure 3.36: Separate and combined effects of 1 plus 2/rev TEF input $\delta = 3°\cos(\psi + \phi_{1p}) + 3°\cos(2\psi + 30°)$ on UH-60A rotor power, for three cases: (i) only 1, 2/rev, (ii) only vibration optimization and (iii) vibration optimization including 1, 2/rev; high speed forward flight (C8534); vibration objective function: J_1.

in 1.5% higher power requirement. The best power reduction using 1, 2/rev inputs only was 2.3% at a phase of 60°. Superimposing 1, 2/rev inputs on the optimal vibration actuation yielded a maximum power reduction of 1.5% at a phase of 90°. Fig. 3.37 shows that of the resultant vibratory hub loads, the vertical shear loads increase by up to 50% even though the inplane shear and moment were still reduced by about 50%. The controller predicted a revised actuation for vibration control at this stage, with the final power requirement nearly the same as the baseline condition. This means that it was possible to reduce vibration levels with a net power reduction.

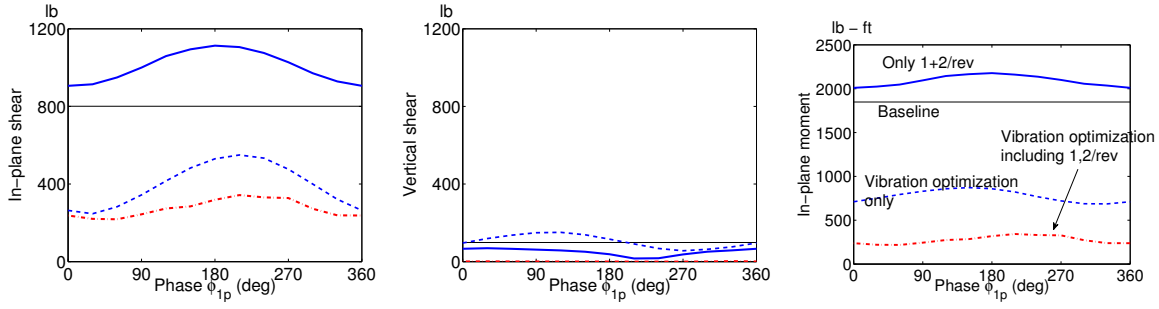

(a) In-plane shear (b) Vertical shear (c) In-plane moment

Figure 3.37: Separate and combined effects of 1 plus 2/rev TEF input $\delta = 3°\cos(\psi + \phi_{1p}) + 3°\cos(2\psi + 30°)$ on UH-60A vibratory hub shears and moments, for three cases: (i) only 1, 2/rev, (ii) only vibration optimization and (iii) vibration optimization including 1, 2/rev; high speed forward flight (C8534); vibration objective function: J_1.

3.9 Concluding remarks

The rotor performance was improved in hover with a combination of torsionally softer blades and positive TEF deflections which contribute to a favorable elastic twist response and reduced induced losses. In high-speed forward flight(C8534),a combination of steady,1 and 2/rev inputs reduced the negative loading on the advancing blade and thus off-loaded the front and rear parts of the disk,improving performance.

2/rev TEF inputs were shown to alter the disk loding to reduce power consumption at high speed (C8534)without significantly altering the trim control settings. A 2.73% power reduction was obtained with a TEF actuation $\delta = 5°cos(2\psi + 15°)$,which reduces the negative loading on the advancing blade.

The loads were redistributed for power benefits using HPP deflections of about 10°. Softening the blades in torsion to improve the effectiveness of the TEF increases the vibratory loads at high speeds,resulting in larger flap actuation requirements for vibration reduction.

Targeting both vibration and power reduction was made possible by a combination of 2,3,4 and 5/rev TEF inputs,resulting in a reduction of power of 1.9% and in-plane vibratory loads of more than 70% at high speed(C8534).The deflection requiements were higher than for separate reductions in power or vibration.

A TEF, with a 1/rev actuation, with a constant downward deflection, was shown to be effective at altering the section angles of attack so as to reduce the severity of retreating blade stall at high thrust (C9017) and in the process reduced

power consumption.The optimal phasing was the one that resulted in maximum downward deflection on the retreating blade and zero deflection on the advancing blade.A combination of 1,2,3, and 5/rev inputs resulted in a power reduction of 7.5%,while also reducing the vibratory loads by 80%,and the severity of the dynamic stall. The 1/rev deflections did not affect the vibration adversely.

Chapter 4: Leading-Edge Slats

4.1 Results and discussion

The effect of leading-edge slats on rotor maximum lift, power requirement and vibratory hub loads is examined in the following sections. The study uses propulsive free flight trim. Vehicle weight and speed are prescribed and the rotor control angles, tail rotor collective and fuselage attitude angles are obtained to maintain force and moment equilibrium about three axes.

4.2 Lift Boundary

Leading-edge slats help increase the maximum lift generated by airfoil sections and are thus capable of pushing the rotor maximum lift boundary above the baseline level for the rotor without slats. Additionally the dynamic behavior of slatted airfoils, in terms of delaying boundary layer separation from the airfoil surface, is better than airfoils without slats. The current results include unsteady corrections to the airloads due to airfoil dynamic properties, as modelled by Leishman and Beddoes. The parameters for the Leishman-Beddoes dynamic stall model (used in UMARC) were modified for the slatted airfoils using the static data obtained from

2D-CFD calculations.

Mishra et al.[7] showed by means of coupled CFD-CSD simulations (without modifications to the baseline structural dynamics) that both static and dynamic stall actuations on a slatted UH-60A blade are highly effective in mitigating the severity of the dynamic stall at the high speed flight condition C9017. This is accompanied by a significant reduction in the peak-to-peak pitch link loads. The improved performance of the blade sections in dynamic stalled flight conditions contributes to an effective increase in the maximum rotor lifting capability in forward flight.

The slat positions used in the analysis are S0, S1 and S6. S0 is a low drag position that is approximated by using the S1 lift and moment characteristics, and the SC1094R8 drag characteristics. The 'no slats' baseline case has the SC2110 airfoil section in place of the UH-60A airfoil sections in the corresponding radial positions. Dynamic actuations considered are :

I. Actuation - 1: a 1/rev motion that passes through S1 at $\psi = 90°$ and S6 at $\psi = 270°$.

II. Actuation - 2: a combination of a 1/rev and 3/rev motion that passes through SI, S0 at $\psi = 90°$ and S6 at $\psi = 270°$.

Figure 2.34a is a graphic of the slat orientation across azimuth in comparison to the fixed S6 case, and figure 2.34b shows the variation of the orientation of the slat element with respect to the main element, as a function of azimuth for each of these dynamic actuations.

Figure 4.1 shows the maximum lift boundary of the rotor without and with

static slats SI and S6 spanning 50-90% R. The McHugh's lift boundary was obtained for a model rotor from wind tunnel testing. The high-lift slatted airfoils S6 increase the maximum rotor C_T/σ by about $15-30\%$ at moderate to high speeds, with the low drag airfoils SI providing about $10-20\%$ more lift than unslatted blades.

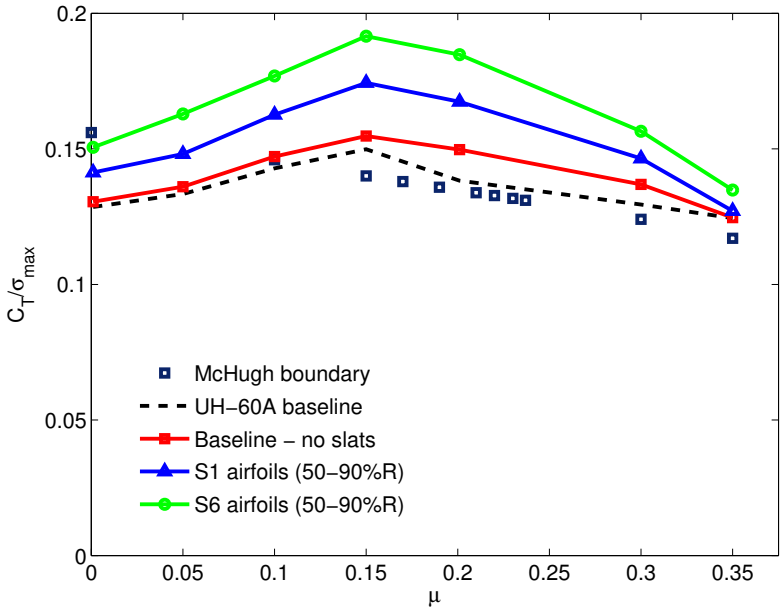

Figure 4.1: UH-60A rotor lift boundary with and without fixed (S1,S6) slats from 50-90%R

In the following sections, the benefits of prescribing dynamic slat actuations to power requirements will be discussed. The dynamic actuations are chosen to retain the high lift benefits of the slats while seeking to minimize profile drag penalties over regions of the rotor disk operating at lower angles of attack i.e. the advancing side.Fig. 4.2 shows the rotor maximum lift boundary with the active slat actuations 1 and 2. Because these configurations pass through the maximum lift position on the retreating side, where the slats have the best benefits, the maximum rotor thrust

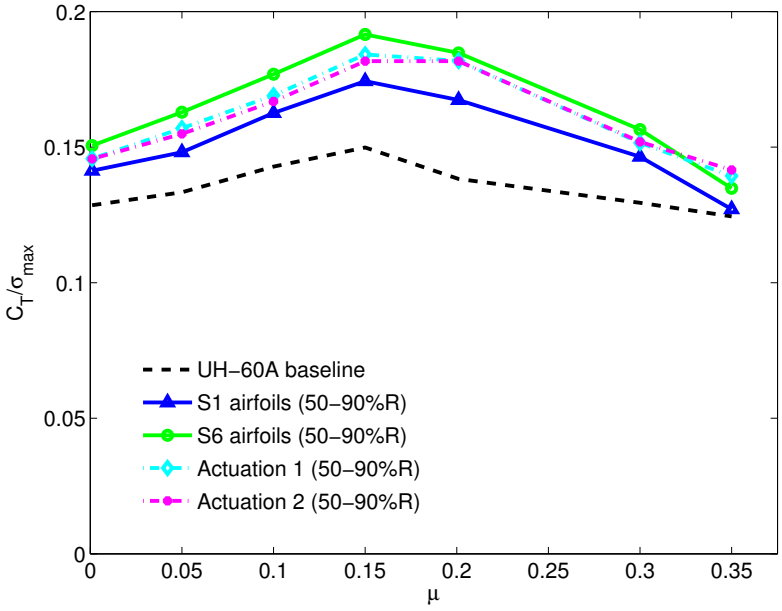

Figure 4.2: UH-60A rotor lift boundary with and without active slats from 50-90%R ; Actuations 1 & 2: dynamic actuations between low drag positions on advancing side and high lift position on retreating side

achievable with them is close to that of the static S6 case, which is highly desirable when combining the benefits in performance and rotor lifting capability.

The effects of accounting for the dynamic properties of airfoil sections are illustrated in Fig.4.3, which shows the maximum predicted rotor thrust from UMARC assuming fully attached flow versus dynamic stalled flow wherever applicable. Thus, the maximum lifting capabilities of the rotor are enhanced when accounting for dynamic characteristics of the airfoil sections. As an example, the predicted maximum lift of the baseline UH-60A rotor is about 15-20% higher with dynamic stall effects.

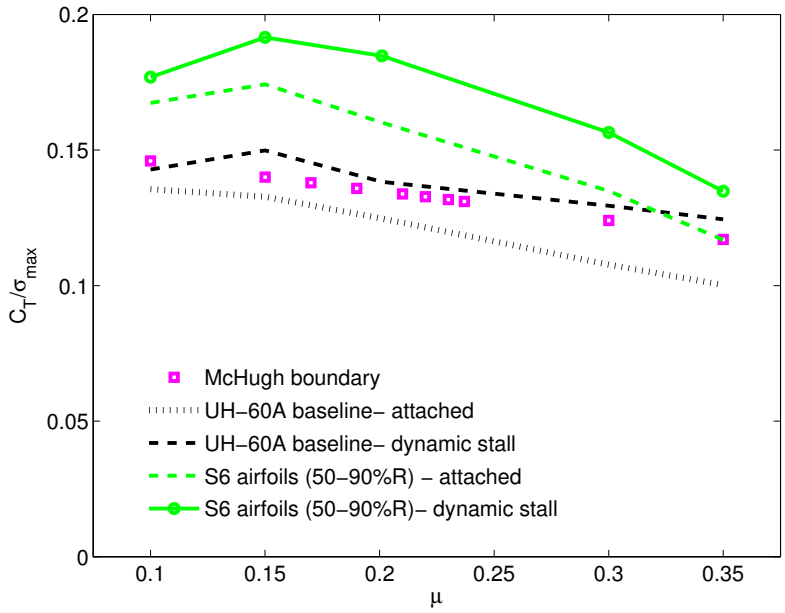

Figure 4.3: UH-60A rotor lift boundary with attached flow assumption and dynamic stall model: baseline rotor and with fixed S6 slats from 50-90%R

4.3 Visualising maximum lift flight condition

Identifying stall is a key step to defining the aerodynamic capability of a rotor. Determination of the maximum achievable thrust numerically requires the use of performance metrics that capture the essence of the rotor loading in high thrust conditions. To this end, two stall-based metrics were considered and monitored to evaluate whether the numerical limit was indeed a satisfactory prediction of the maximum rotor lift limit:

1. A static indicator, namely the extent of static airfoil pitching moment stall.

2. A dynamic indicator - C_{mx}/σ. The higher harmonic ($\geq$ 4/rev) torsion moment at the blade root, mx, in non-dimensional form, C_{mx}, is defined as HPP moment/$(m_0)(\Omega R)^2 R$). Lorber et al.[6] used this definition for a quantitative measure of the strength of the retreating blade stall.

1. **Static indicator:**

   One method of capturing the limit of the rotor's lifting ability is to examine the extent of the rotor disk that is stalled as the operating thrust level increases. Fig.4.4 shows the areas of the baseline UH-60A rotor disk where blade sections are operating at angles beyond the values for (2-D) pitching moment stall at the corresponding local Mach numbers. The flight conditions considered for this purpose are $\mu = 0.3$ and weight coefficients from 0.07 through the maximum achievable value at this forward speed. The sections below the local stall angle are white, while the stalled sections are denoted by black.

It can be seen that blade sections are likely to stall even before the lift limit is actually reached and the 'stalled'regions of the rotor disk gradually increase in size as the maximum lift limit is approached. In this case, in going from C_w/σ of 0.08 to the maximum thrust condition at this speed i.e. C_w/σ of 0.1325 (Fig.4.5e), the percentage of the rotor with stalled blade sections increases from 2.5% to 20.2%.

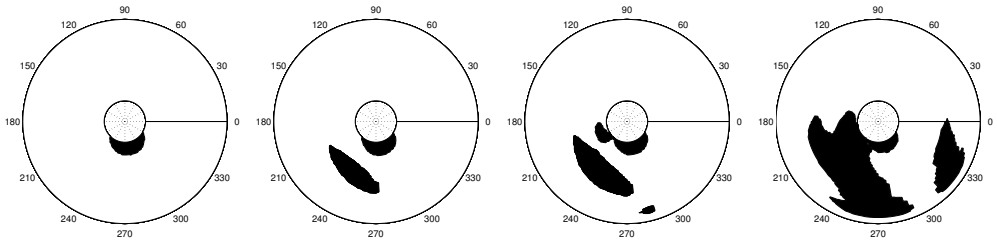

(a) $C_W/\sigma = 0.08$ (b) $C_W/\sigma = 0.1$ (c) $C_W/\sigma = 0.12$ (d) $C_W/\sigma = 0.1325$ (limit)

Figure 4.4: Baseline UH-60A rotor: stalled blade sections for different operating thrust levels, $\mu = 0.3$

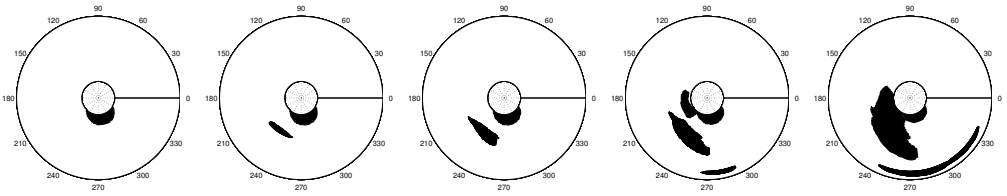

(a) $C_W/\sigma = 0.08$ (b) $C_W/\sigma = 0.1$ (c) $C_W/\sigma = 0.12$(d) $C_W/\sigma = 0.14$(e) $C_W/\sigma = 0.16$ (limit)

Figure 4.5: UH-60A rotor with fixed S6 slats from 50-90%R: stalled blade sections for different operating thrust levels, $\mu = 0.3$

The effect of having the S6 slats from 50-90% R on rotor blade stall is shown in figure 4.5. In this case, going from C_w/σ of 0.08 (figure 4.5a) to the maximum thrust condition at this speed i.e. C_w/σ of 0.16 (figure 4.5e), the percentage of the rotor with stalled blade sections increases from 2.5% to 13.7%. As compared to the baseline UH-60A rotor, the slatted rotor achieved 21% increase in maximum thrust capability. The stalled regions of the disk are smaller at

the same operating weight.

Fig. 4.6 shows the percentage of the rotor disk that is stalled, as a function of operating thrust (C_T/σ) for the UH-60A baseline rotor and with fixed slats from 50-90% R, at advance ratios of 0.2 and 0.3. Slatted blade sections need to operate at lower angles of attack to achieve the same thrust, due to increased lifting characteristics. They are also able to operate till higher angles of attack before the onset of flow separation and stall. These factors contribute to the higher achievable maximum rotor lift with leading-edge slats.

2. **Dynamic indicator:**

The choice of this metric is motivated by the increase in torsion loads as a result of pitching moment stall. Since the 1/rev as well as higher frequency content (due to the stall spike) of the loads increase with thrust, only the higher harmonics ($\geq$ 4/rev) are retained. Fig. 4.9 shows the variation of the dynamic indicator C_{mx}/σ as a function of blade loading/thrust level C_T/σ for two forward flight advance ratios, 0.2 and 0.3. There is a steep rise in the moment loads as thrust is increased, and again with the slatted sections, the metric is lower than for the baseline rotor at high speed and high thrust levels.

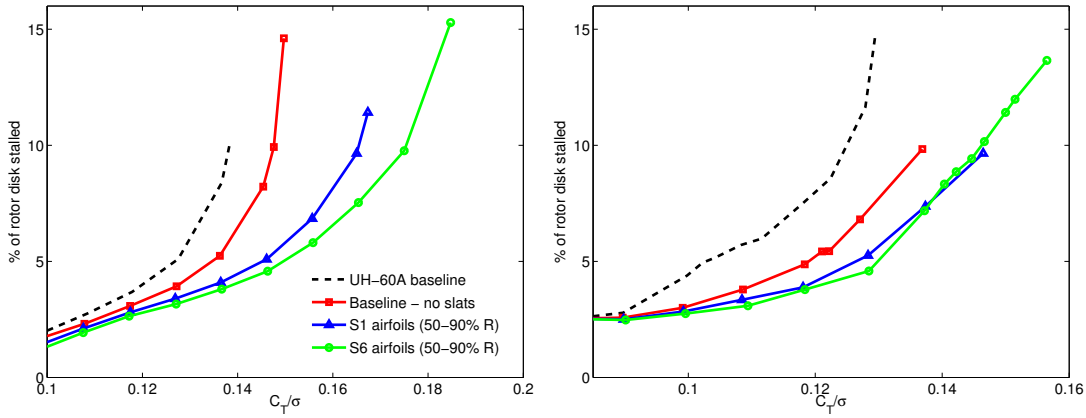

(a) $\mu = 0.2$ (b) $\mu = 0.3$

Figure 4.6: UH-60A rotor without and with fixed slats from 50-90%R: % of rotor disk with stalled airfoil sections

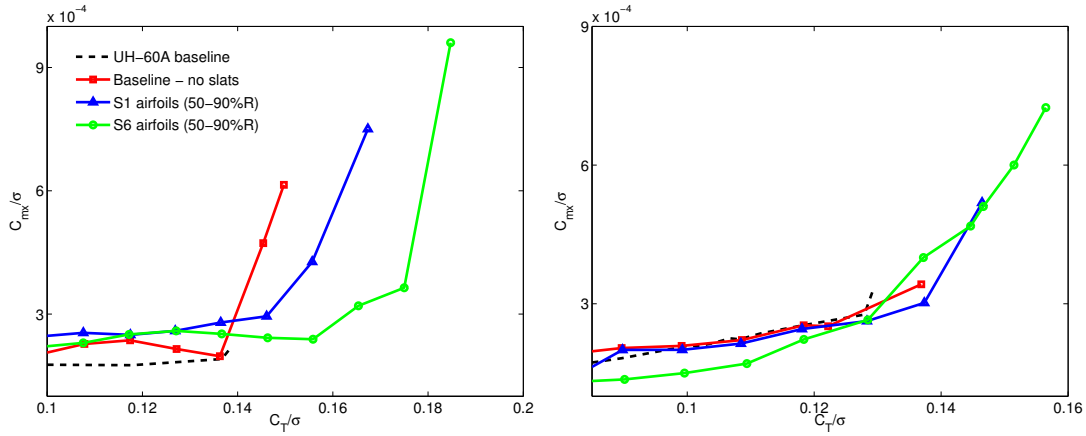

(a) $\mu = 0.2$ (b) $\mu = 0.3$

Figure 4.7: UH-60A rotor without and with fixed slats from 50-90%R: dynamic indicator of rotor stall C_{mx}/σ

4.4 Power requirement with Leading-Edge Slats

In the previous sections, the lift-enhancing benefits of leading-edge slats were discussed. In addition to these benefits, it may be possible to achieve a decrease in power requirement by prescribing dynamic actuations that take advantage of the lift-enhancing properties of the slat on the retreating side, while trying to minimize the drag penalty on the advancing side by means of low-drag slat configurations.

Figs. 4.10-4.13 show the power requirement and break-up of power (induced and profile) with increasing thrust at advance ratios of 0, 0.1, 0.2 and 0.3, for the rotor without and with slats fitted to the blades from 50-90% R. The cases considered are fixed S1 and S6 slats, and dynamic actuations 1 and 2 from 50-90% R. In hover ($\mu = 0$), the induced power is a dominant component, and therefore, the slat has a

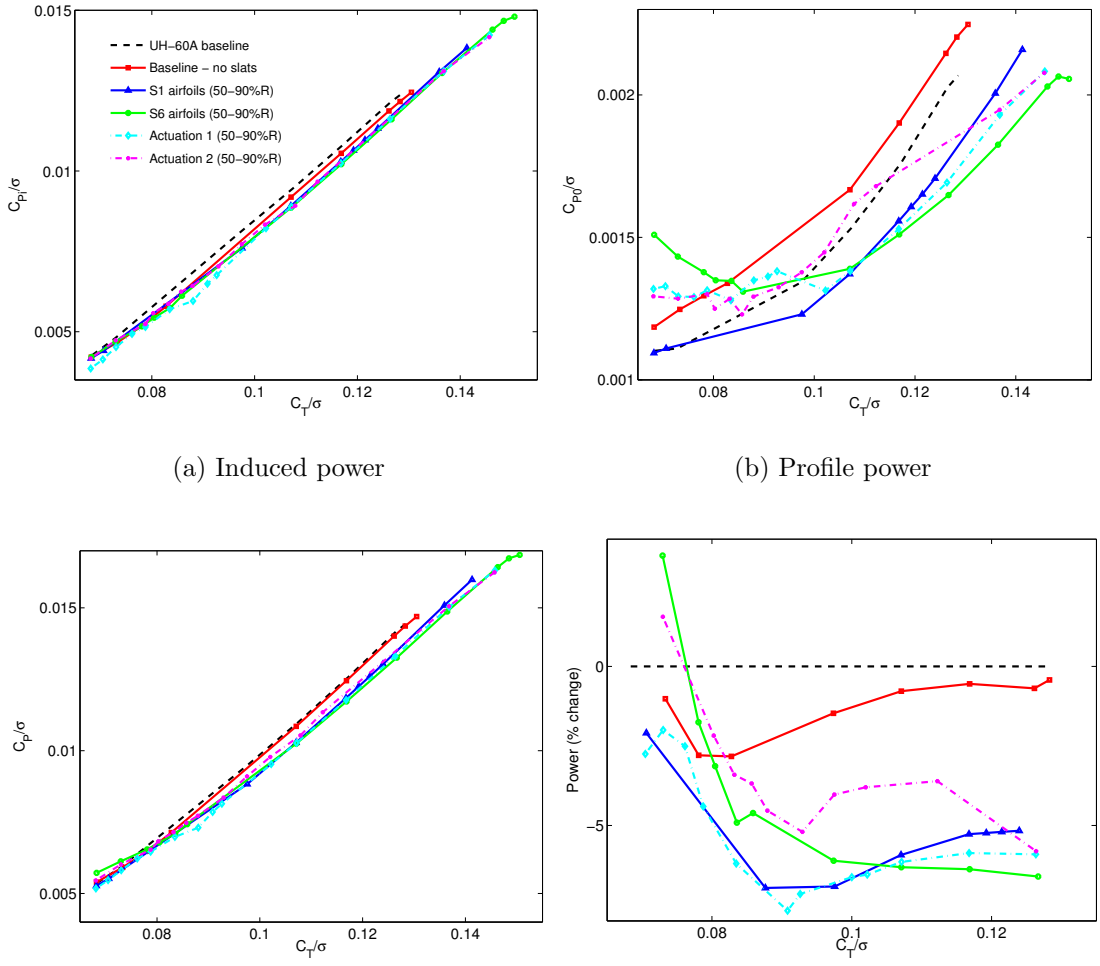

(a) Induced power

(b) Profile power

(c) Total power

(d) % change in power from baseline

Figure 4.8: UH-60A components of rotor power vs thrust at $\mu = 0$, without and with slats from 50-90%R ; Actuations 1 & 2: dynamic actuations between low drag positions on advancing side and high lift position on retreating side

smaller effect on total power. On the other hand, at higher speeds, the slat plays a more important role. For example, figure 4.12d shows that at $\mu = 0.3$, static S6 deployed from 50-90% R reduces power consumption for $C_T/\sigma > 0.12$, while dynamic actuation 2 reduces power consumption for $C_T/\sigma > 0.105$. The benefits

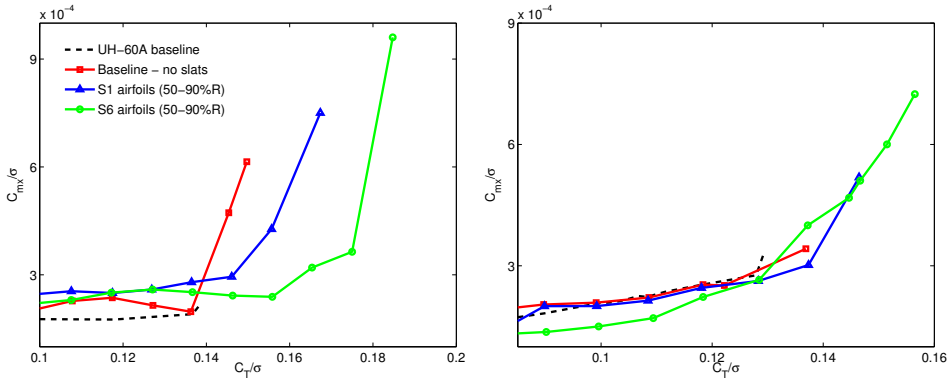

(a) $\mu = 0.2$ (b) $\mu = 0.3$

Figure 4.9: UH-60A rotor without and with fixed slats from 50-90%R: dynamic indicator of rotor stall C_{mx}/σ

are seen in both induced power and profile power. At lower thrust levels, where the operating angles of attack are low, blades with slats do not benefit from the lift-enhancing properties of slats and high profile power penalties are incurred. This leads to increased power requirements at low thrust levels and low advance ratios. The performance benefits of leading-edge slats are most appreciable at high thrust flight conditions. The active deployments 1 and 2 perform better than the fixed slats (S6) at low thrusts because the slat is retracted back over the baseline airfoil on the advancing side (positions S0 and S1). Using actuation 2, power reductions of about 10-15% are predicted at the maximum baseline rotor operating thrust at different forward speeds.

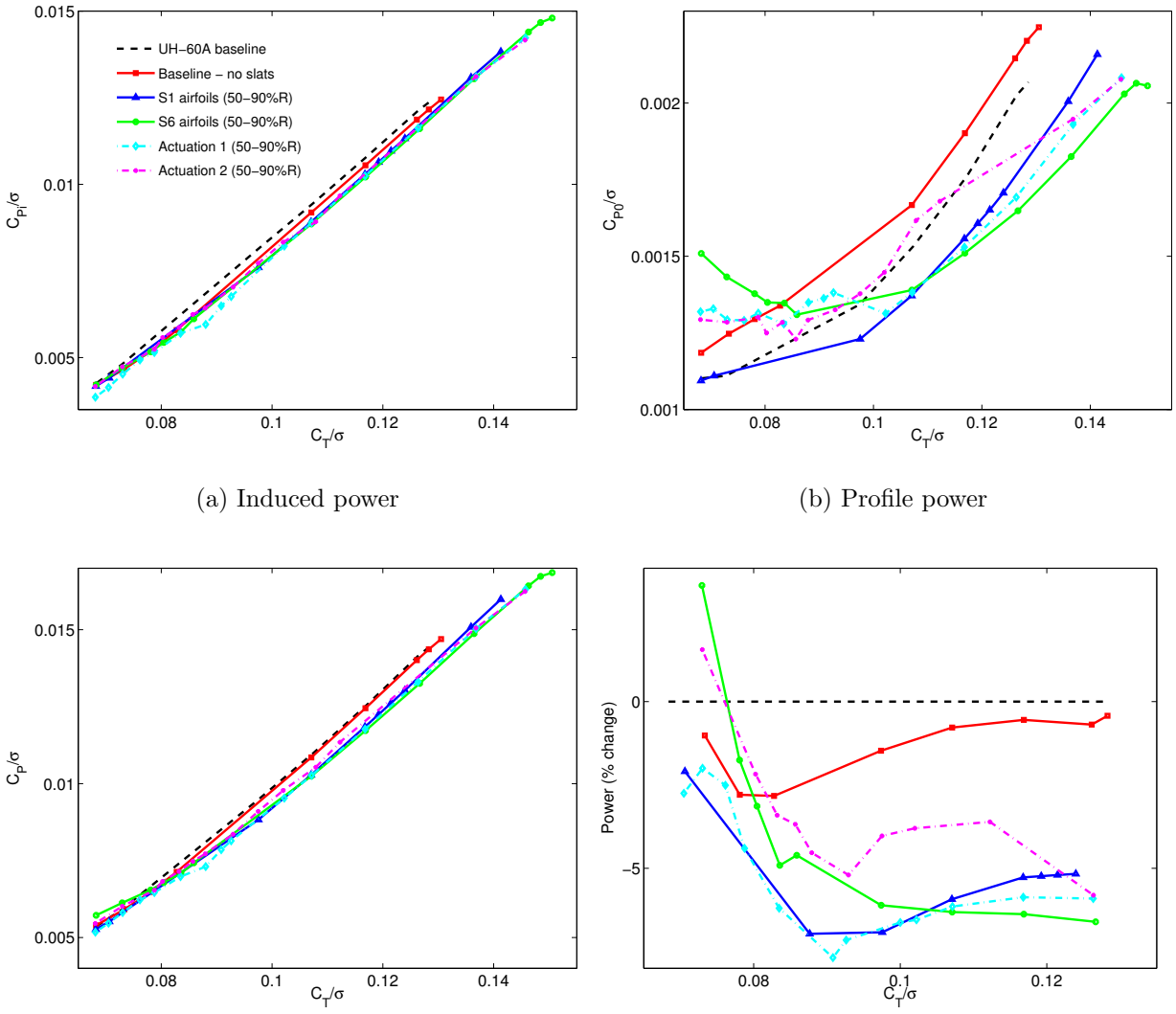

(a) Induced power

(b) Profile power

(c) Total power

(d) % change in power from baseline

Figure 4.10: UH-60A components of rotor power vs thrust at $\mu = 0$, without and with slats from 50-90%R ; Actuations 1 & 2: dynamic actuations between low drag positions on advancing side and high lift position on retreating side

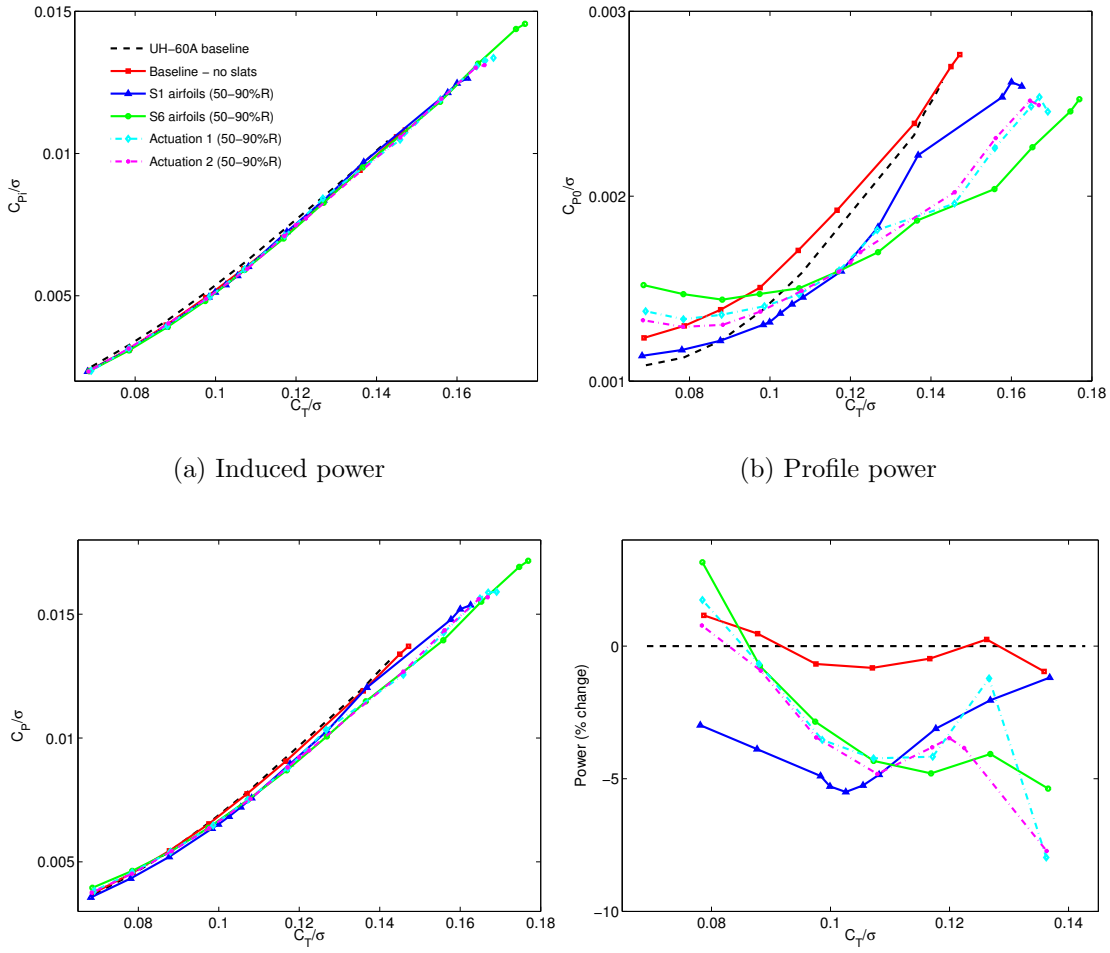

(a) Induced power

(b) Profile power

(c) Total power

(d) % change in power from baseline

Figure 4.11: UH-60A components of rotor power vs thrust at $\mu = 0.1$, without and with slats from 50-90%R ; Actuations 1 & 2: dynamic actuations between low drag positions on advancing side and high lift position on retreating side

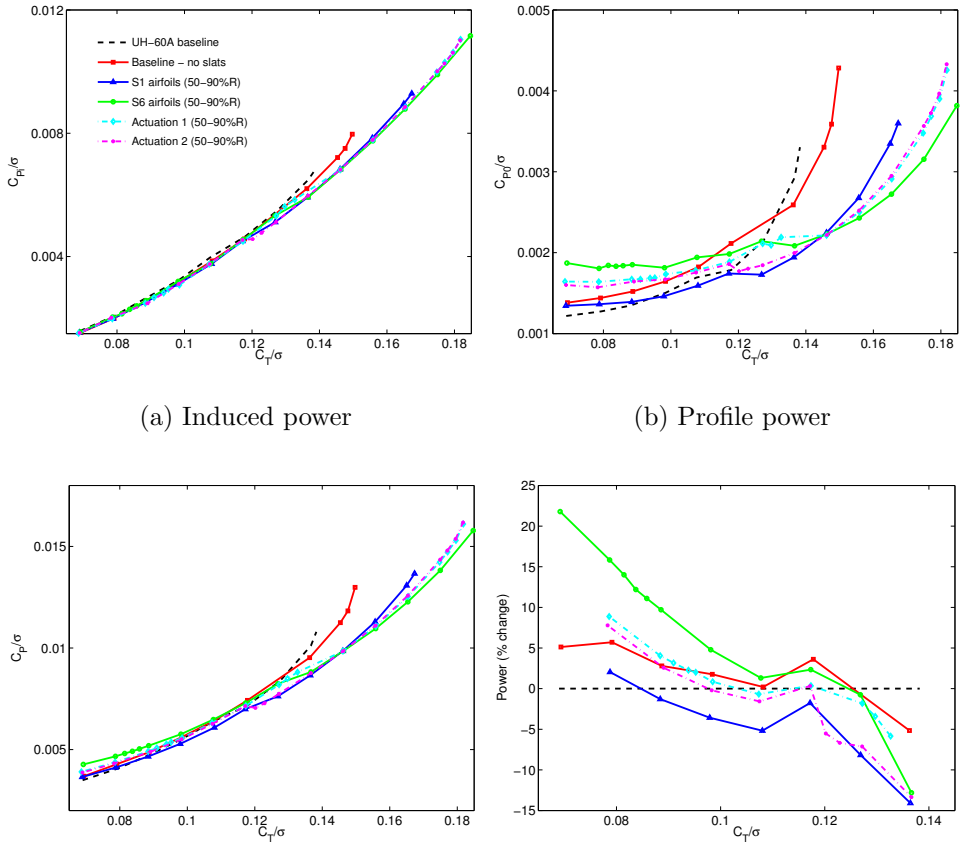

(a) Induced power

(b) Profile power

(c) Total power

(d) % change in power from baseline

Figure 4.12: UH-60A components of rotor power vs thrust at $\mu = 0.2$, without and with slats from 50-90%R ; Actuations 1 & 2: dynamic actuations between low drag positions on advancing side and high lift position on retreating side

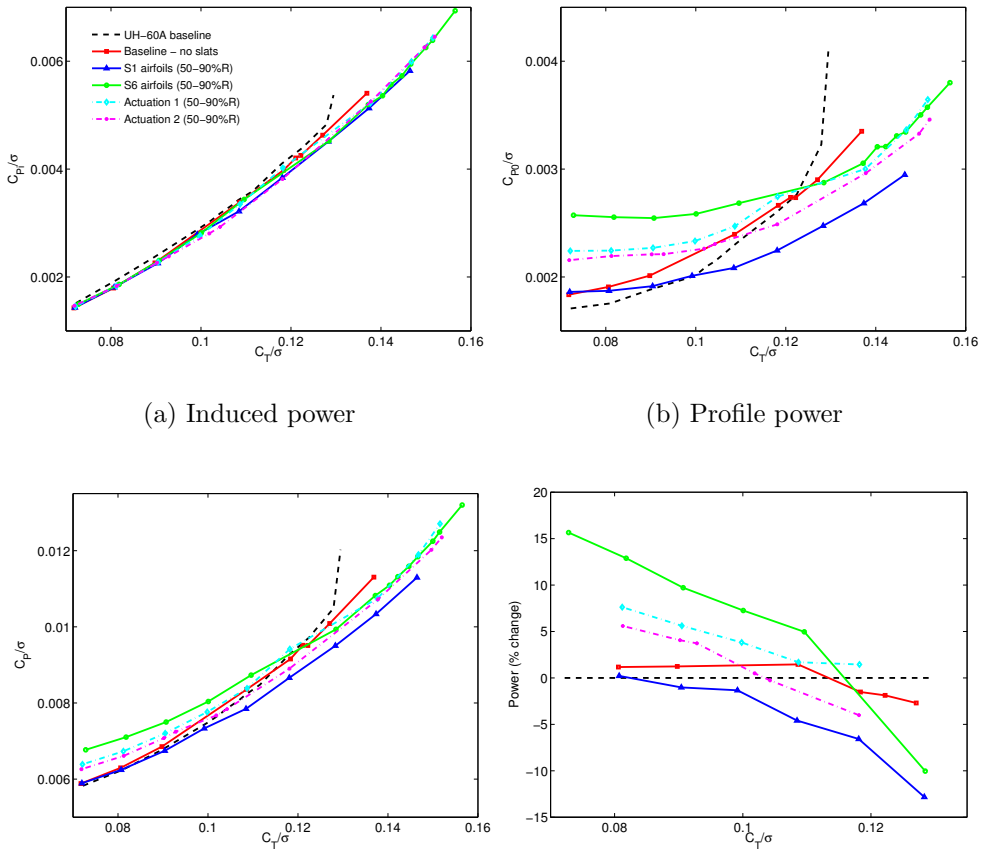

(a) Induced power

(b) Profile power

(c) Total power

(d) % change in power from baseline

Figure 4.13: UH-60A components of rotor power vs thrust at $\mu = 0.3$, without and with slats from 50-90%R ; Actuations 1 & 2: dynamic actuations between low drag positions on advancing side and high lift position on retreating side

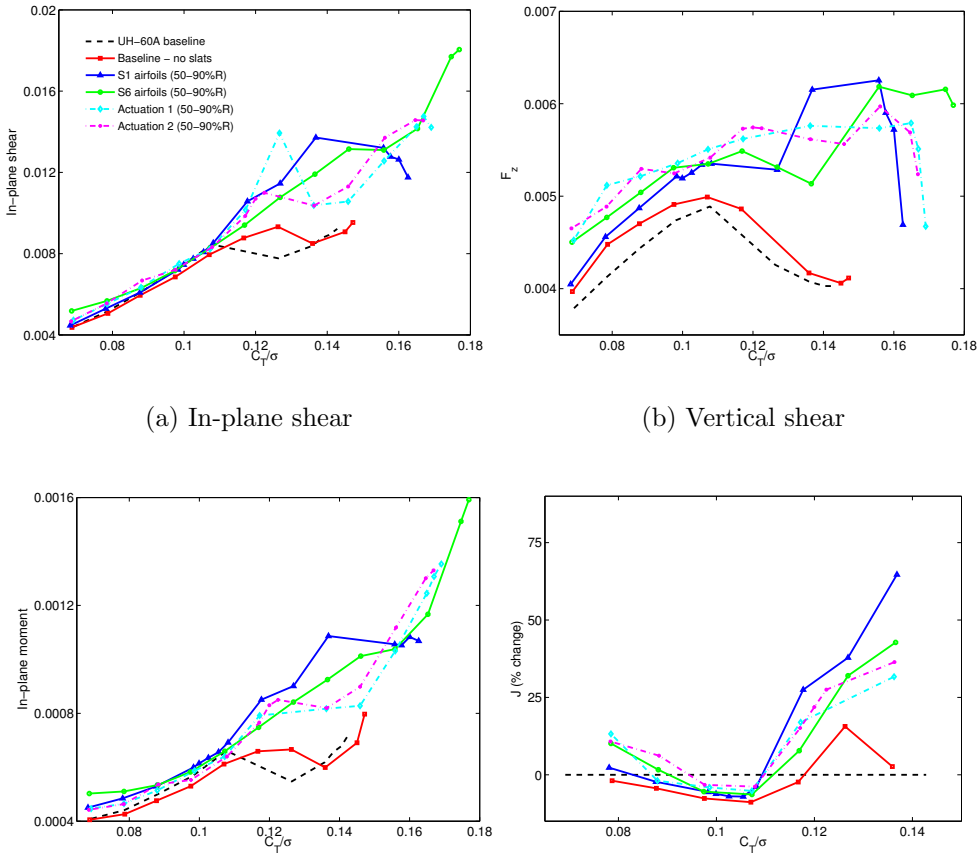

(a) In-plane shear

(b) Vertical shear

(c) In-plane moment

(d) Vibration index J

Figure 4.14: UH-60A hub vibratory loads vs thrust at $\mu = 0.1$, without and with slats from 50-90%R ; Actuations 1 & 2: dynamic actuations between low drag positions on advancing side and high lift position on retreating side

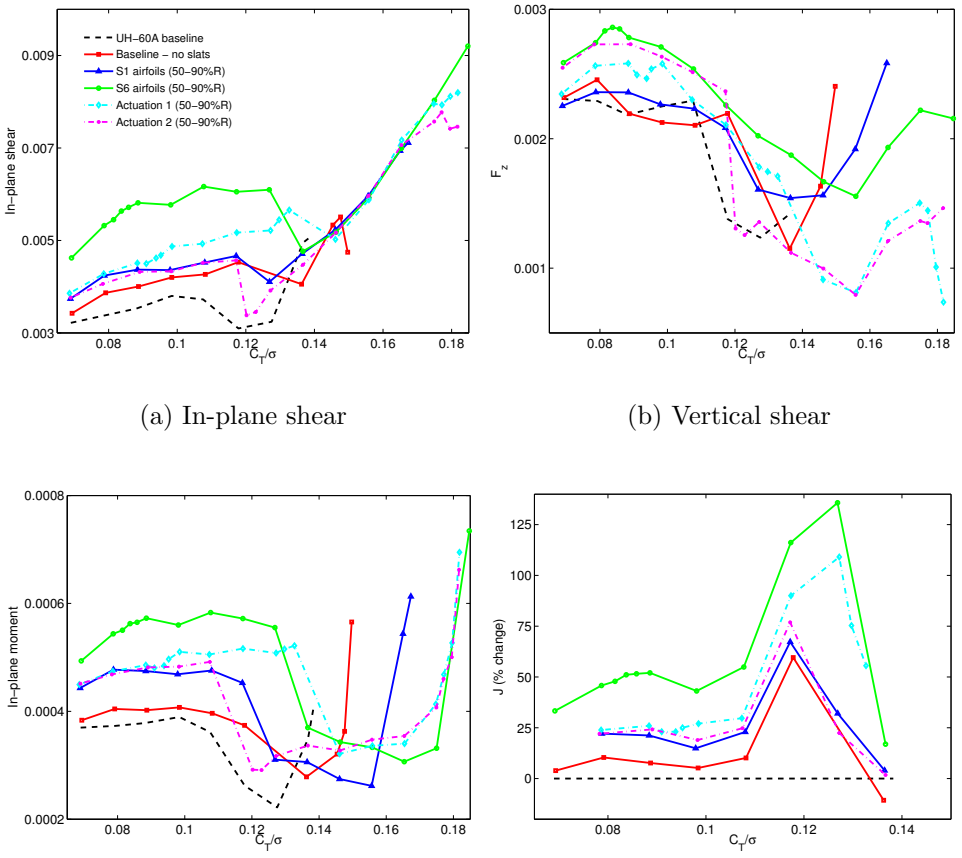

(a) In-plane shear

(b) Vertical shear

(c) In-plane moment

(d) Vibration index J

Figure 4.15: UH-60A hub vibratory loads vs thrust at $\mu = 0.2$, without and with slats from 50-90%R ; Actuations 1 & 2: dynamic actuations between low drag positions on advancing side and high lift position on retreating side

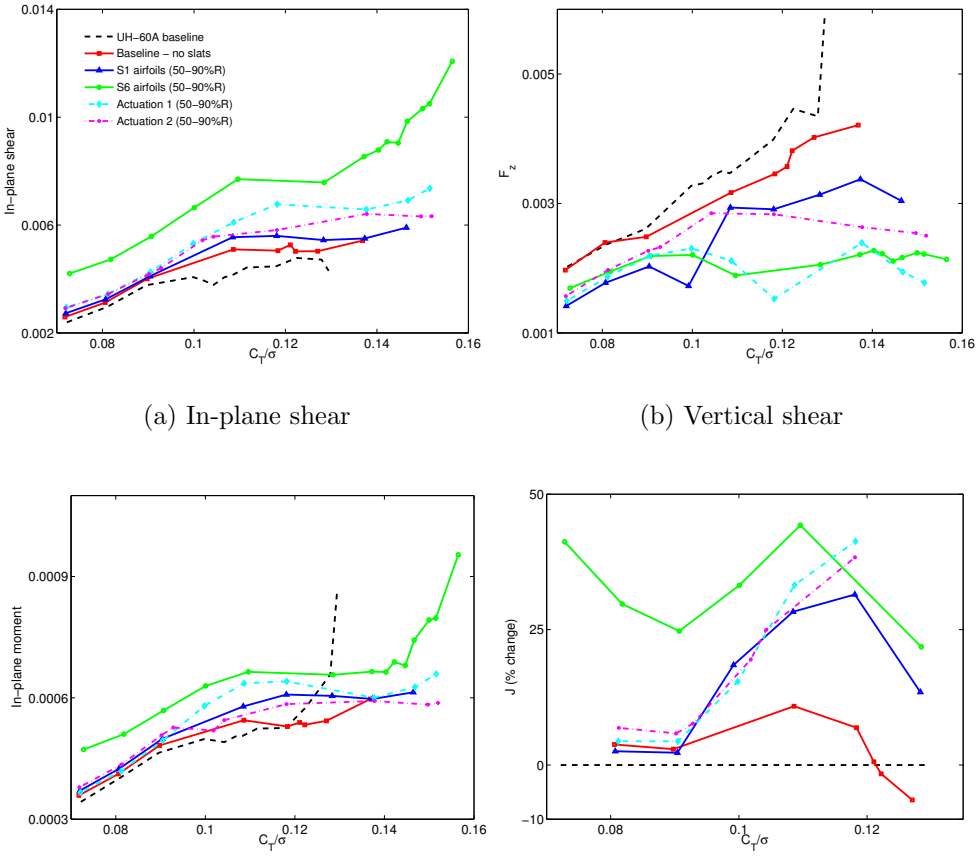

(a) In-plane shear

(b) Vertical shear

(c) In-plane moment

(d) Vibration index J

Figure 4.16: UH-60A hub vibratory loads vs thrust at $\mu = 0.3$, without and with slats from 50-90%R ; Actuations 1 & 2: dynamic actuations between low drag positions on advancing side and high lift position on retreating side

In the following sections, the benefits of prescribing dynamic slat actuations to power requirements will be discussed. The dynamic actuations are chosen to retain the high lift benefits of the slats while seeking to minimize profile drag penalties over regions of the rotor disk operating at lower angles of attack i.e., the advancing side. Figure 4.2 shows the rotor maximum lift boundary with the active slat actuations 1 and 2. Because these configurations pass through the maximum lift position on the retreating side, where the slats have the best benefits, the maximum rotor thrust achievable with them is close to that of the static S6 case, which is highly desirable when combining the benefits in performance and rotor lifting capability.

The effects of accounting for the dynamic properties of airfoil sections are illustrated in figure 4.3, which shows the maximum predicted rotor thrust from UMARC assuming fully attached flow versus dynamic stalled flow wherever applicable. Thus, the maximum lifting capabilities of the rotor are enhanced when accounting for dynamic characteristics of the airfoil sections. As an example, the predicted maximum lift of the baseline UH-60A rotor is about 15-20% higher with dynamic stall effects.

4.5 Vibratory hub loads with Leading-Edge Slats

Figs.(4.14-4.16) show the 4/rev vibratory hub loads with increasing thrust at advance ratios of 0.1, 0.2 and 0.3, for the rotor without and with slats fitted to the blades from 50-90% R The shear and moment hub loads are respectively non-dimensionalized by the quantities $(m_0\Omega R)^2$ and $(m_0\Omega R)^2 R$. The vibratory load metrics compared here are:

1. 4/rev hub in-plane shear

2. 4/rev hub vertical shear

3. 4/rev hub in-plane moment

4. Vibration index J, defined as

$$J = \sqrt{(F_x/F_{x,0})^2 + (F_y/F_{y,0})^2 + (F_z/F_{z,0})^2 + (M_x/M_{x,0})^2 + (M_y/M_{y,0})^2}$$

where the subscript '0' denotes the quantities for the corresponding baseline (UH-60A) case.

In general, the vibratory hub loads are seen to increase from the baseline levels in the presence of leading-edge slats, particularly the in-plane shear loads (Figs. 4.14a,4.15a,4.16a). It is observed that the dynamic active deployments 1 and 2 (50-90% R) perform better than the fixed slats S1 and S6 [Fig.4.14a] and the increase in in-plane shear loads at $\mu = 0.1$ and $C_T/\sigma = 0.12$ and $C_T/\sigma = 0.14$ is in the range of 10-15%. At higher forward speeds, there is a reduction in the hub vertical shear and in-plane moments at high thrust levels (Figs. 4.16b-4.16c). Comparison of the vibration index J with the baseline UH-60A rotor shows that up to 75% increase in vibration results from the use of leading-edge slats. The penalties are less severe at low speeds and thrust levels.

Overall, the dynamic actuations appear to be a good compromise between enhancing performance and impacting vibration the least. The possibility of vibration reduction using higher frequency actuation (2-5/rev) of leading-edge slats is a topic of future studies.

4.6 Varying span-size of Leading-Edge Slats

The spanwise extent of the leading-edge slats used earlier, namely 50-90%, was chosen to completely replace the SC1094R8 airfoil sections on the UH-60A blade. In this section, trade-offs in power requirement and vibratory hub loads with varying spanwise lengths are examined. The different leading-edge slat sizes used are:

I 20% R : 50-70% R, 60-80% R, 70-90% R

II. 30% R : 40-70% R, 50-80% R, 60-90% R

III. 40% R : 40-80% R, 50-90% R

The dynamic slat actuation Actuation 2 is chosen for this parametric study, because it has been shown to offer the best compromise in enhanced lift, reduction of power requirement and changes in vibratory load levels.

Fig. 4.17 shows the power requirement, break-up of power (induced and profile) , and rotor lift-to-drag ratio L/D_e ($\mathrm{L}/D_e = \mathrm{T}/(\mathrm{P}/V_\infty - \mathrm{D}_v)$, D_v being the vehicle drag at an operating weight coefficient C_w/σ of 0.08 and as a function of advance ratio, for the rotor without and with slats of varying lengths fitted to the blades and actuated as per the previously defined Actuation 2. Fig. 4.18 shows the effect of the varying span lengths on the vibratory hub loads. Figs. 4.19 and 4.20 show the same quantities at an operating weight coefficient of 0.1.

From a performance standpoint, the slats are less effective when located outboards (70-90% R, 60-90% R, 50-90% R) where the dynamic pressure is higher, because blade angles of attack are lower and profile drag penalties are higher due to slats, as shown in figures 4.17b and 4.19b for the two weights. The rotor L/D_e

is lower and power requirement is consequently higher, as shown in figures 4.17d , 4.19d and 4.17c , 4.19c respectively.

At the lower weight,the slats are seen not to offer much benefit and in fact impact the performance (upto 10% decrease in L/D_e) and vibration adversely (upto 25%) at high speeds, but at the higher weight, an improvement of up to 14% in maximum L/D with the 40% span slats is predicted with an accompanied penalty of nearly 30% in vibratory hub loads, while a modest 10% improvement in L/D with a smaller increase (20% at high speeds) or decrease in the vibratory loads is seen with the 20% span slat from 70-90%R.

4.7 Forward flight speed limit with Leading-Edge Slats

Having pushed the maximum lift of the rotor at all forward speeds with leading-edge slats, it is expected that the vehicle with a slatted rotor ought to be able to operate at higher speeds than the baseline. To this end, the slatted rotor was trimmed at a nominal thrust level C_T/σ of 0.08 to determine the highest forward speeds the rotor could operate at.

Fig. 4.21 shows the power requirement, break-up and rotor L/D for the rotor without and with slats fitted to the blades from 50-90% R. Fixed slats S1 and S6 as well as dynamic actuations 1 and 2 are considered here. The highest advance ratio the baseline UH-60A rotor could be trimmed to was 0.45, while the slatted rotors could be trimmed up to an advance ratio of 0.49. As expected, the power requirement is generally higher with slats at this moderate thrust level, although

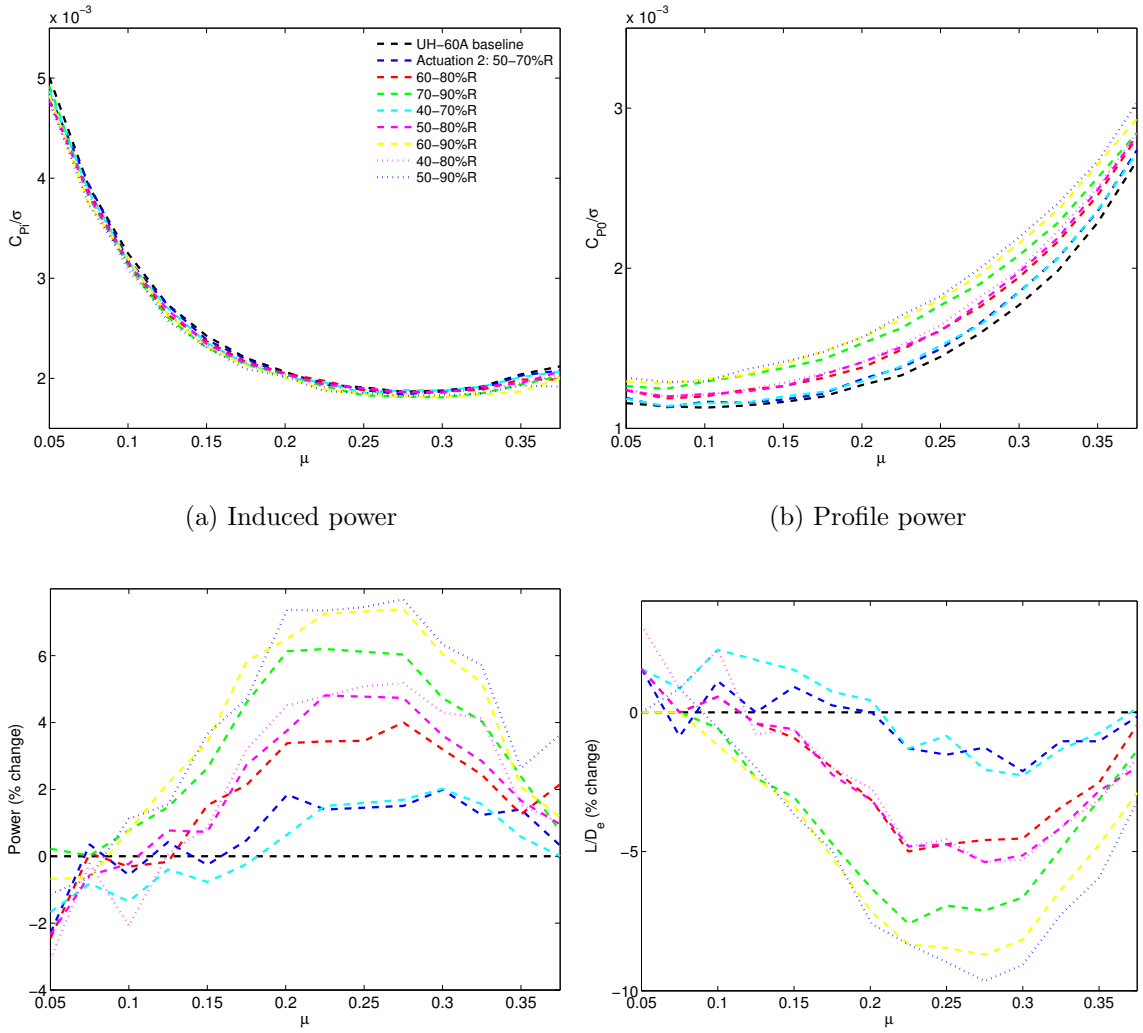

(a) Induced power

(b) Profile power

(c) % change in power from baseline

(d) % change in rotor L/D_e from baseline

Figure 4.17: UH-60A components of rotor power vs thrust at $C_W/\sigma = 0.08$, without and with slats of varying spanwise lengths; Actuation 2: dynamic actuation between low drag positions on advancing side and high lift position on retreating side

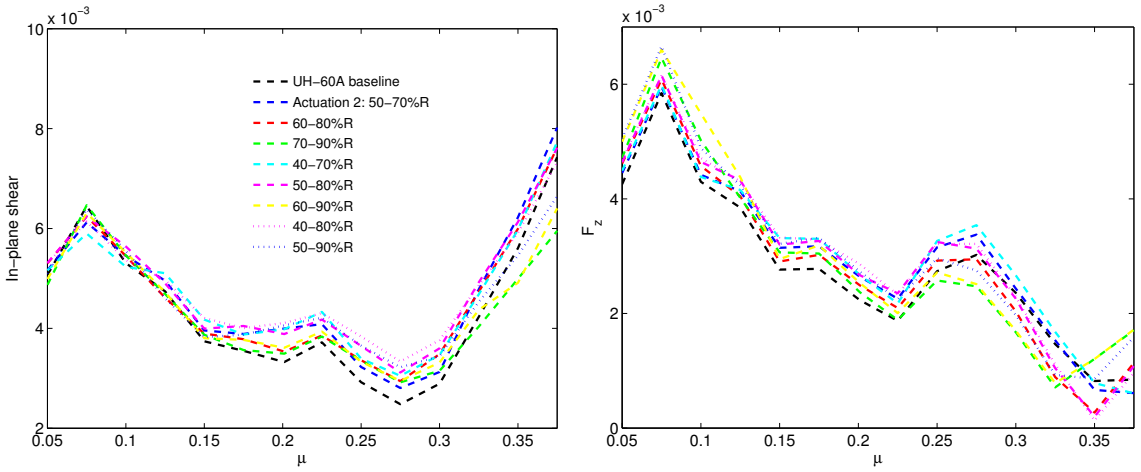

(a) In-plane shear

(b) Vertical shear

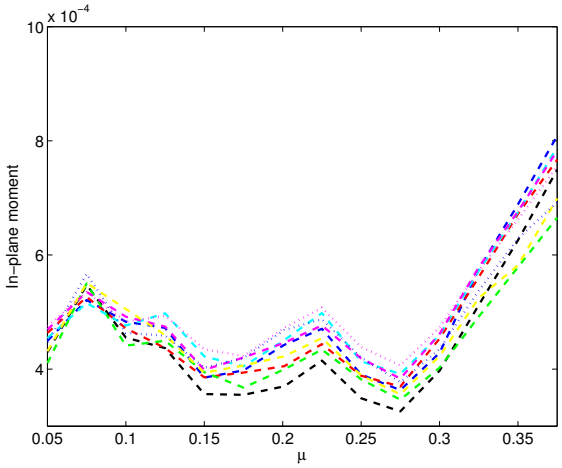

(c) In-plane shear

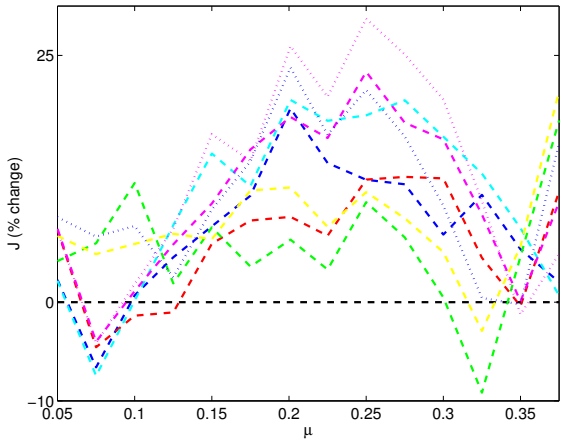

(d) Vibration index J

Figure 4.18: UH-60A vibratory hub loads vs thrust at $C_W/\sigma = 0.08$, without and with slats of varying spanwise lengths; Actuation 2: dynamic actuation between low drag positions on advancing side and high lift position on retreating side

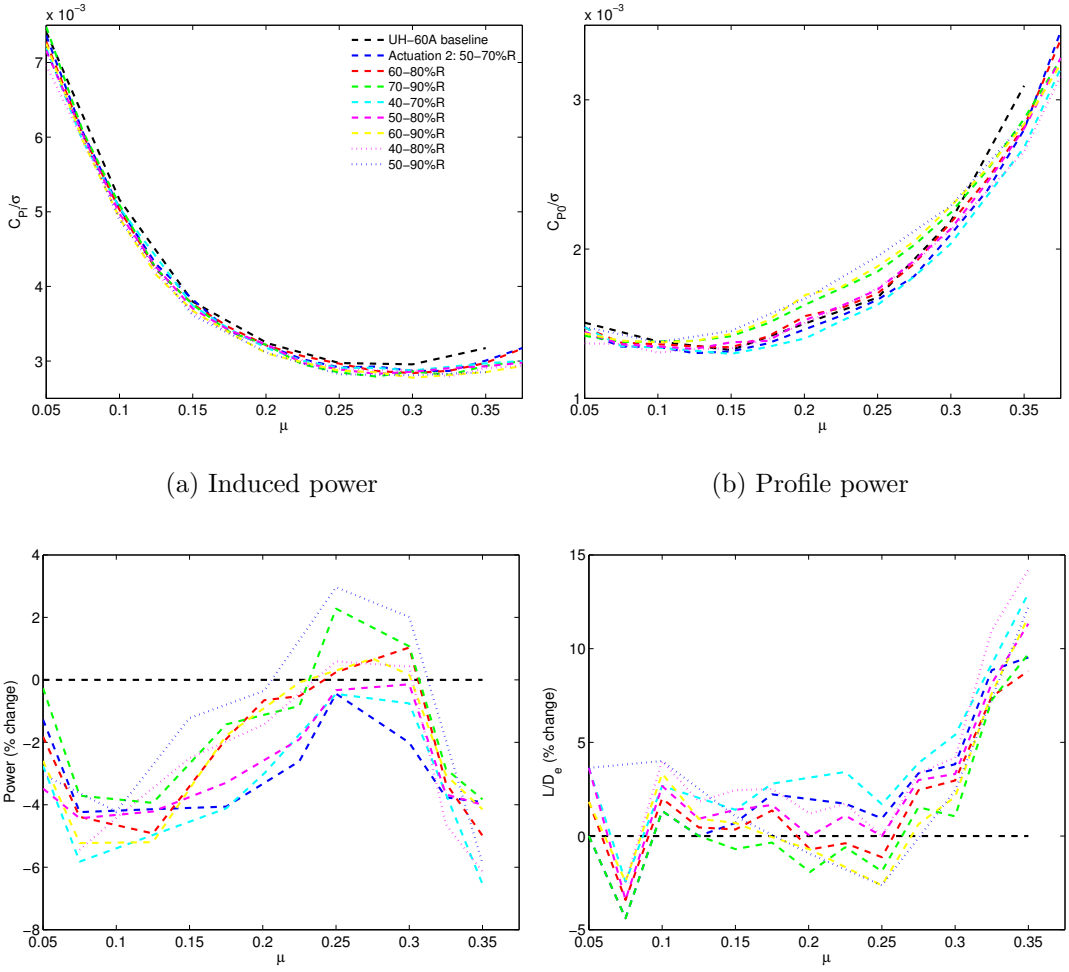

(a) Induced power

(b) Profile power

(c) % change in power from baseline

(d) % change in rotor L/D_e from baseline

Figure 4.19: UH-60A components of rotor power vs thrust at $C_W/\sigma = 0.1$, without and with slats of varying spanwise lengths; Actuation 2: dynamic actuation between low drag positions on advancing side and high lift position on retreating side

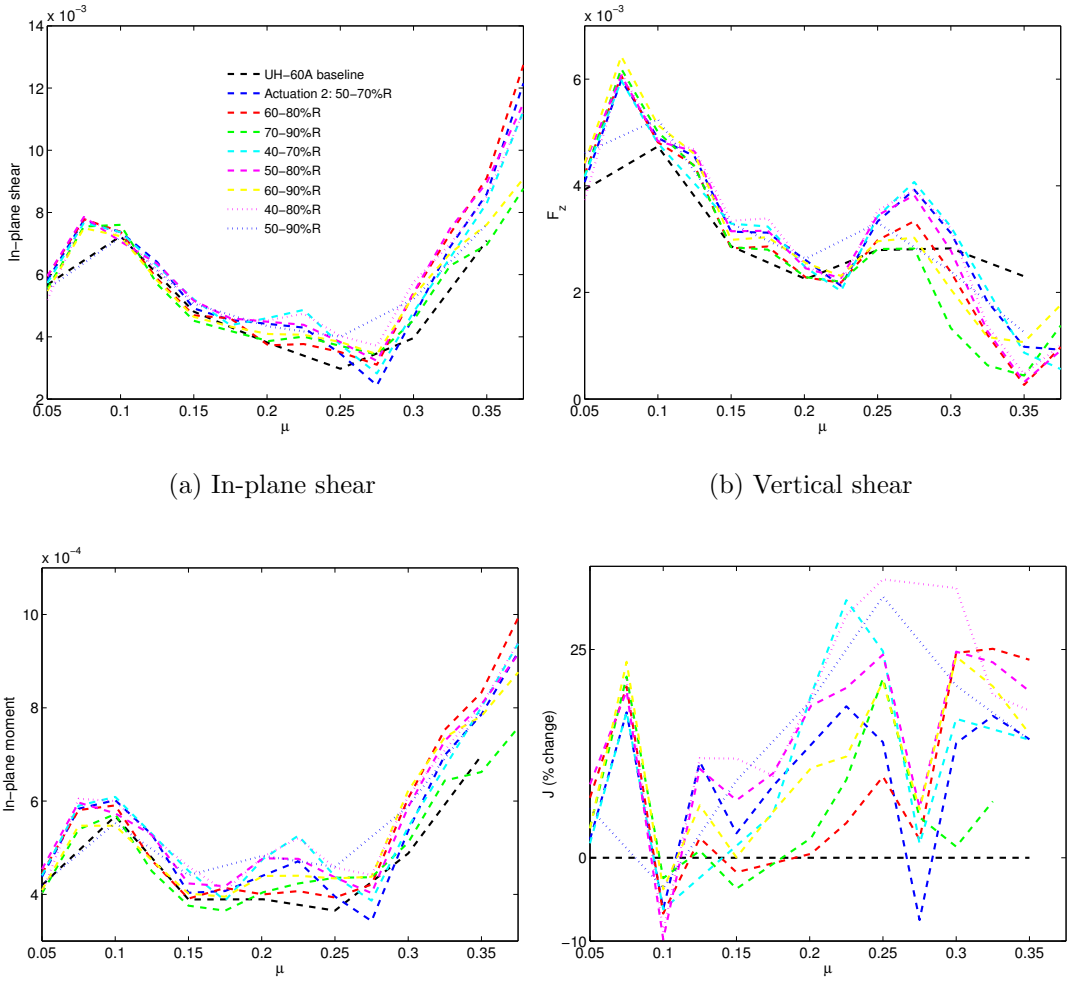

(a) In-plane shear

(b) Vertical shear

(c) In-plane moment

(d) Vibration index J

Figure 4.20: UH-60A vibratory hub loads vs thrust at $C_W/\sigma = 0.1$, without and with slats of varying spanwise lengths; Actuation 2: dynamic actuation between low drag positions on advancing side and high lift position on retreating side

the fixed S1 slats appear to be a good compromise, offering some power reductions even at this operating thrust.

Fig. 4.22 shows the power required to maintain trimmed flight between μ =0.4 and 0.5,for the baseline UH-60A and the slatted rotor.S6 and S1 fixed-slat configurations could be trimmed upto μ =0.49,which is 20 knots faster than the maximum trim speed of the baseline UH-60A rotor.The S6 fixed-slat configuration achieves an incrementally higher trimmed V_{max} than the corresponding S1 configuration with a 20% additional power penalty.

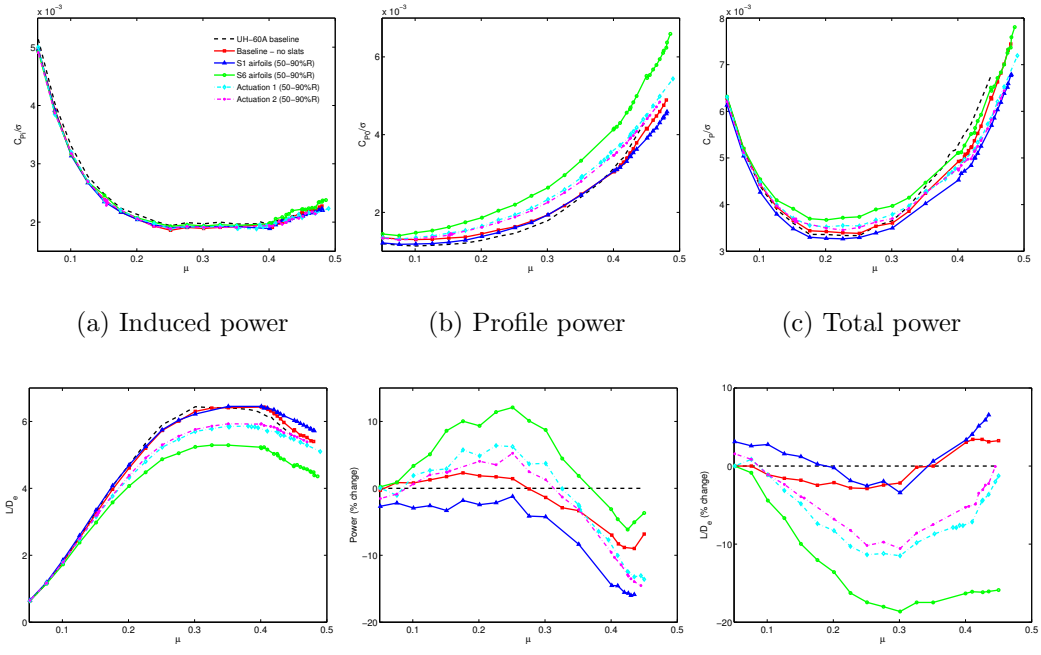

(a) Induced power (b) Profile power (c) Total power

(d) Rotor L/D_e (e) % change in power from baseline (f) % change in rotor L/D_e from baseline

Figure 4.21: UH-60A components of rotor power vs thrust at $C_T/\sigma = 0.08$, without and with slats from 50-90%R ; Actuations 1 & 2: dynamic actuations between low drag positions on advancing side and high lift position on retreating side

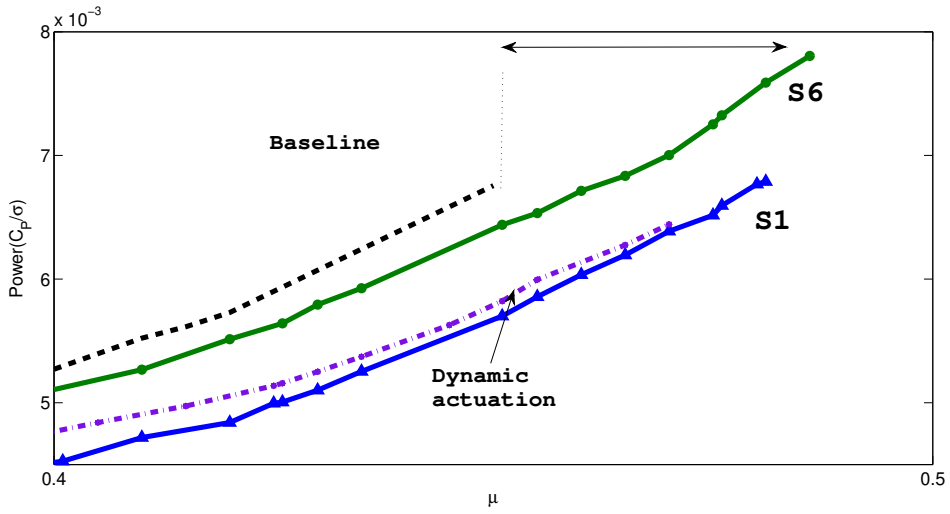

Figure 4.22: Effect of slats on rotor performance and rotor envelope;slats increase V_max by 20 knots,indicated by the double-ended horizontal arrows

4.8 Concluding remarks

Leading-edge slats with span 40% rotor radius, chord upto 15% blade chord and nominal midspan located at 70 % R and at different orientations were investigated for the purposes of improving the rotor maximum lift capability and reducing power requirement from the baseline rotor values. From this study, the following conclusions are drawn:

1. The maximum achievable rotor thrust was increased by about 15-30% at advance ratios greater than 0.2 using leading-edge slats. The slatted rotor had a smaller portion of the rotor disk with stalled blade sections as compared to the baseline rotor. Slatted blade sections need to operate at lower angles of attack to achieve the same thrust, due to increased lifting characteristics. They are

also able to operate till higher angles of attack before the onset of flow separation and stall. These factors contribute to the higher achievable maximum rotor lift with leading-edge slats.The high frequency content ($\succeq$ 4/rev) of the blade torsional loads, an indicator of dynamic stall, was also smaller for the slatted rotor at high speeds and high thrust levels.

2. At lower thrust levels, where the operating angles of attack are low, blades with slats do not benefit from the lift-enhancing properties of slats and high profile power penalties are incurred. This leads to increased power requirements at low thrust levels and low advance ratios. The performance benefits of leading-edge slats are most appreciable at high thrust flight conditions. Power reductions of the order of 10-15% at various speeds were achieved using dynamic slat actuations combining high-lift and low-drag orientations in a 1/rev fashion across azimuth. The maximum slat rotation angle between different orientations (relative to the baseline airfoil) was about 10°.

3. The dynamic actuations still yielded nearly the same improvements in maximum rotor lift capability.

4. Leading-edge slats were in general found to affect vibratory hub loads adversely, particularly at lower speeds. At higher forward speeds, there is a reduction in the hub vertical shear and in-plane moments at high thrust levels.The penalties are less severe at low speeds and thrust levels.Overall, the dynamic actuations appear to be a good compromise between enhancing performance while impacting vibration the least.

5. A 10% improvement in L/D accompanied with an increase of up to 20% (at high speeds) or decrease in the vibratory loads was seen with a 20% span slat located between 70-90% R.

6. The slatted rotor was trimmed at forward speeds not achievable by the baseline rotor i.e. up to $\mu = 0.49$, indicating that it is possible to push not just the lift limits of the rotor, but also the forward speed limits with the use of leading-edge slats.

Chapter 6: Summary and conclusions

Studies of active rotor TE flaps and LE slats in recent years have tended towards methods of enhancing performance over a wide range of operating conditions.Concepts such as fixed and dynamic slats, Variable Droop Leading-Edge airfoils, circulation control and trailing-edge flaps have been considered for active aerodynamic flow control, as opposed to passive designs involving blade geometry. Of these, trailing-edge flaps (TEFs) and leading-edge slats are notable for their conceptual simplicity and wide-ranging potential. Comprehensive rotor analyses appear suited for evaluation of active control concepts through parametric studies to determine configurations that yield maximum benefits, and understand the mechanisms of their operation.

The objective of this study has been to use a comprehensive analysis to assess and quantify the capabilities of trailing-edge flaps and leading-edge slats for performance improvement at high speeds, and recommend flap and slat configurations for the UH-60A rotor blades that maximize performance benefits.

6.1 Summary

The University of Maryland Advanced Rotorcraft Code(UMARC) was modified to simulate the effects of trailing-edge flaps and leading-edge slats.The near-wake model was modified to account for the effect of TEFs on the blade bound circulation distribution.The structural, inertial and aerodynamic contributions of TEFs and LESs were integrated into the baseline blade analysis in UMARC.The TEF is modeled as a single additional degree of freedom and the motion of the flap is prescribed in the analysis.The slat motion is modeled with 3 additional degrees of freedom to improve conformity of the slat airfoil with the blade airfoil.The slatted blade sections had the SC2110 baseline/slatted airfoils in place of the baseline UH-60A airfoils:SC1095 and SC1094R8.The slat configurations were designed for optimum channeling of the flow near the leading edge of the SC2110 airfoil, hence the replacement of the baseline UH-60A airfoils in the slat sections.

The impact of TEFs on hover performance was examined with different steady flap deflections and with a variation in the torsional stiffness. Performance gains with active control surfaces are expected to be largest at high speeds and high thrust levels, where a small redistribution of loading can result in significant reductions. Rotor performance in high speed forward flight with TEFs is investigated by carrying out parametric sweeps of TEF actuations to determine suitable combinations of steady, 1 and 2/rev TEF inputs that can yield overall power reductions. Different combinations of steady+2/rev TEF inputs were prescribed, in order to obtain the trends of the actuations that had the best impact on performance. Two advance

ratios, $\mu = 0.3$ and 0.4, were chosen for the study, and different thrust levels (in terms of non-dimensional vehicle weight coefficient C_W/σ) were investigated. Then, a moderate thrust level condition ($C_W/\sigma = 0.09$) at $\mu = 0.3$, and an operating condition close to the maximum lift boundary ($C_W/\sigma = 0.085$) at $\mu = 0.4$, were chosen to further investigate the benefits of 1/rev inputs, strictly in an open-loop sense. Rotor vibration reduction with TEFs was studied for high-speed flight conditions along with the effect of torsional stiffness to estimate the optimal actuation requirements to get the best results.The possibility of simultaneous power and vibration reduction with TEFs for high-speed flight conditions was explored with different steady and 2/rev inputs superimposed on 1/rev inputs.Stall alleviation using TEFs with down-only 1/rev inputs was studied to assess the scope for reduction of the magnitude of dynamic stall events occurring in high thrust forward flight.

The maximum lift boundary of the rotor without and with static slats S1 and S6 was obtained using UMARC and was compared with the McHugh's lift boundary obtained for a model rotor from wind tunnel testing to demonstrate that the high-lift slatted airfoils S6 and the low drag airfoils S1 can increase the maximum rotor thrust at moderate to high speeds and provide more lift than unslatted blades.Various dynamic actuations that take advantage of the lift enhancing properties of the slat on the retreating side while trying to minimize the drag penalty on the advancing side by means of low-drag slat configurations, were studied to identify a suitable configuration that can result in lower power consumption.The vibratory hub load levels in the presence of leading edge slats were studied at various speeds and low and high thrust levels to determine when the penalties are less severe.The trade-

offs in power requirements and vibratory hub loads with varying spanwise lengths were examined to arrive at the dynamic slat actuations that can offer the best compromise in enhanced lift, reduction of power requirement and changes of vibratory loads.Having pushed the maximum lift of the rotor at all forward speeds with the aid of leading-edge slats,it was also examined whether the vehicle with a slatted rotor can be trimmed to attain forward speeds higher than the baseline.

The advantages of superimposition of TEFs and leading-edge slats were studied for 1/rev TEF actuations of the form $\delta = \delta_{1p}\cos(\psi + \phi_{1p})$, which were imposed on the slatted rotor operating at μ=0.4,C_W/σ=0.095,in an effort to improve the power benefits by alleviating the negative loading on the advancing blade.The increments in section aerodynamic properties due to TEFs were assumed to be generic CFD-generated values obtained for the SC1094R8 airfoil.

6.2 Conclusions-TEFs

A trailing-edge flap with span of 10% rotor radius, chord of 15% blade chord and its midspan located at 65%R was evaluated for performance improvement in hover and high speed forward flight and reduction of 4/rev hub vibratory loads in forward flight. From this study, the following conclusions are drawn:

(1) The rotor performance in hover was improved with a combination of torsionally softer blades and positive flap deflections, which contribute to a favorable elastic twist response and reduced induced losses.

(2) The rotor performance in high speed forward flight was improved by a suitable

combination of steady, 1/rev and 2/rev TEF inputs to reduce the negative loading on the advancing blade and thus off-load the front and rear parts of the disk.

(3) The 2/rev actuation phase for the best benefits lies between 0° and 30°, while the 1/rev actuation phase for the best benefits in conjunction with 2/rev input lies between 0° and 90°.

(4) Power reductions of the order of 2% at $\mu = 0.3$ and 4-5% at $\mu = 0.4$ were observed using HPP actuation amplitudes of 5°-10°.

(5) The flap was shown to be capable of suppressing the target hub loads at a range of forward speeds, using half peak-to-peak deflections of about 5°. Softening the blades in torsion in order to improve the effectiveness of the TEF was found to increase the vibratory loads at high speed (C8534), resulting in larger flap actuation requirements for vibration reduction.

6.3 Conclusions-LESs

Leading-edge slats with span 40% rotor radius, chord upto 15% blade chord and nominal midspan located at 70 % R and at different orientations were investigated for the purposes of improving the rotor maximum lift capability and reducing power requirement from the baseline rotor values. From this study, the following conclusions are drawn:

(1) The maximum achievable rotor thrust was increased by about 15-30% at ad-

vance ratios greater than 0.2 using leading-edge slats. The slatted rotor had a smaller portion of the rotor disk with stalled blade sections as compared to the baseline rotor. Slatted blade sections need to operate at lower angles of attack to achieve the same thrust, due to increased lifting characteristics. They are also able to operate till higher angles of attack before the onset of flow separation and stall. These factors contribute to the higher achievable maximum rotor lift with leading-edge slats.The high frequency content ($\succeq$ 4/rev) of the blade torsional loads, an indicator of dynamic stall, was also smaller for the slatted rotor at high speeds and high thrust levels.

(2) At lower thrust levels, where the operating angles of attack are low, blades with slats do not benefit from the lift-enhancing properties of slats and high profile power penalties are incurred. This leads to increased power requirements at low thrust levels and low advance ratios. The performance benefits of leading-edge slats are most appreciable at high thrust flight conditions. Power reductions of the order of 10-15% at various speeds were achieved using dynamic slat actuations combining high-lift and low-drag orientations in a 1/rev fashion across azimuth. The maximum slat rotation angle between different orientations (relative to the baseline airfoil) was about 10°.

(3) The dynamic actuations still yielded nearly the same improvements in maximum rotor lift capability.

(4) Leading-edge slats were in general found to affect vibratory hub loads adversely, particularly at lower speeds. At higher forward speeds, there is a

reduction in the hub vertical shear and in-plane moments at high thrust levels .The penalties are less severe at low speeds and thrust levels.Overall, the dynamic actuations appear to be a good compromise between enhancing performance while impacting vibration the least.

(5) A 10% improvement in L/D accompanied with an increase of up to 20% (at high speeds) or decrease in the vibratory loads was seen with a 20% span slat located between 70-90% R.

(6) The slatted rotor was trimmed at forward speeds not achievable by the baseline rotor i.e., up to $\mu = 0.49$, indicating that it is possible to push not just the lift limits of the rotor, but also the forward speed limits with the use of leading-edge slats.

The superimposition of TEFs and leading-edge slats shows that for three different slat configurations from 50-90%:fixed slats S_6,and dynamic slat actuations 1 and 2,an additional power reduction of about 2% was possible by suitable TEF deployments superimposed on slat actuation 2, for a net reduction of about 15% at this flight condition.Again, the 1/rev input of the form $-\delta_{1p}\sin(\psi)$ increases the lift on the advancing side while offloading other parts of the disk, which translates into a net power reduction.Increasing the 1/rev amplitude beyond 5° begins to degrade performance.

6.4 My publications

6.4.1 Journal papers

(1) *Open-Loop Control of Performance And Vibratory Loads Using Leading Edge Slats*, with Chopra, Inderjit, submitted to the Journal of the American Helicopter Society 61, 0320032016.

(2) *Trailing-Edge Flaps for rotor performance enhancement and vibration reduction*, with Chopra, Inderjit and Wake, Brian and Hein, Benjamin, Journal of the AHS, 58.022006(2013).

6.4.2 Conference Papers

(1) *Active Rotor Controls for Vibration Reduction and Performance Enhancement*, with Ananthan, Shreyas and Chopra, Inderjit and Hein, Benjamin, 23-44, AHS Aeromechanics Specialists Conference, San Francisco, 20-22 January 2010.

(2) *Active Flaps and Slats for Rotor Performance Enhancement*, with Chopra, Inderjit and Wake, Brian and Hein, Benjamin, 188-204, 67th American Helicopter Society International Annual Forum 2011, Virginia Beach, 3-5 May 2011

(3) *Active Control of Performance and Vibratory Loads using Leading Edge Slats*, with Chopra, Inderjit, 53rd AIAA/ASME/ASCE/AHS/ASC Structures, Structural Dynamics and Materials Conference, 20th AI, 23-26 April 2012, Hon-

olulu, Hawaii.

6.5 Future areas of research

While the concept of active rotor control using trailing- edge flaps has been explored for several years now, it has not yet reached the point of being validated for in-flight primary and vibration control.

This study has shown that TEFs are capable of vibration reduction and performance improvement.Leading-edge slats are also shown to enhance the rotor thrust in moderate to high-speed flight conditions and reduce power requirements at high thrust levels.Experimental testing of the active rotor concept is key to the validation of the analysis employed. The most immediate areas of interest are:

- Systematic experiments need to be conducted under actual flight conditions to validate these results.
- Parametric studies for primary control using leading-edge slats to improve the flight envelope.
- Posssibility of vibration reduction using leading-edge slats.

In the long term, other possible areas of interest are:

- Relaxing the assumption of single-degree of freedom flaps/slats to model them as flexible structures.
- Development of a more complex aerodynamic model for unsteady motion of an airfoil with arbitrary geometry, fitted with flaps/slats.

- Validation of the trailing-edge flaps in unsteady flight conditions is important,since they are likely to be more tested under such conditions. Current work is focused on steady level flight.

- Vibration and noise analyses need a more elaborate study of the acoustics and fuselage low harmonics, rather than the rotor.

Bibliography

[1] Leishman,J.G.,"Principles of Helicopter Aerodynamics",Cambridge University Press,2002.

[2] Johnson,W., and Jolly.M.,"Helicopter Aeromechanics",AHS 63rd Annual Forum Proceedings,Virginia Beach,VA,May 1-3,2007.

[3] Bousman,W.,"Putting the Aero Back Into Aeroelasticity",Eighth ARO Workshop on Aeroelasticity of Rotorcraft Systems,University Park,PA,Oct 18-20,1999.

[4] United States Government,"Requirements for Helicopter Flying Qualities Aeronautical Design Standard-Requirements for Rotorcraft Design Standard-Requirements for Rotorcraft Vibration Specifications Modeling and Testing",MIL-H-8501,November 1952.

[5] United States Government,"General Requirements for Helicopter Flying and Ground Handling Qualities",MIL-H-8501A,September 1961.

[6] "Aeronautical Design Standard- Requirements for Rotorcraft Vibration Specifications Modeling and Testing,"ADS-27A-SP,U.S.Army Aviation and Missile Command, May 2006.

[7] Ellis,C.W., and Jones,R.,"Application of an Absorber to Reduce Helicopter Vibration Levels",Journal of the American Helicopter Society,8(3):330-38,July 1963.

[8] Schuett,E.P.,"Application of Passive Helicopter Rotor Isolation for Alleviation of Rotor Induced Vibration",Journal of the American Helicopter Society14(2):34-48,April 1969.

[9] Amer,K.B.,and Neff,J.R.,"Vertical Plane Pendulum Absorbers for Minimizing Helicopter Vibratory Loads",Journal of the American Helicopter Society,Vol.19(4):44-48,Oct 1974.

[10] Taylor,R.B.,"Helicopter Vibration Reduction by Rotor Blade Modal Shaping",38th Annual Forum of the American Helicopter Society,1982Anaheim,CA;19-21 Jan 1994,pp.5.2-1:5.2-9.

[11] Leconte,Ph,Geoffroy,P.,"Dynamic optimization of a rotor blade",presented at the AHS Aeromechanics Specialists Conference,San Francisco,January 1994.

[12] Wilson.M, and Jolly.M.,"Ground test of a Hub Mounted Active Vibration Suppressor",AHS63rd Annual Forum Proceedings,Virginia Beach,VA,May 1-3,2007.

[13] Loewy R.G"Helicopter Vibrations ;a technological perspective",Journal of AHS,Vol 29(4),October 1984, pp.4-30.

[14] Viswanathan,S.P. and McClure,Robert D.,"Analytical and experimental investigation of a bearingless hub absorber",Journal of the American Helicopter Society,Vol.28,No. 3,July 1983,pp. 47-55.

[15] Bielawa,R.L.,"Rotary wing and structural dynamics and Aeroelasticity",AIAA,Washington D.C.,1982.

[16] Lim,J. and Chopra,I.,"Aerodynamic optimization of a helicopter rotor absorber",Journal of the American Helicopter Society,Vol.34(1),Jan 1989,pp. 33-41.

[17] Bao,J.,Nagaraj,V.T.,Chopra,I.,and Bernhard,A.P.F.,"Development of a Low Vibration Mach Scale Rotor with Composite Couplings",American Helicopter Society 58th Annual Forum Proceedings,Vol II,11-13 June 2002,Montreal,Canada;11-13 Jan 1994,pp.2081-2094.

[18] Staple,A.E.,"An Evaluation of Active Control of Structural Response as a Means of Reducing Helicopter Vibration",pp. 51.1-51.18;15th European Rotorcraft Forum,September 1989,Amsterdam,The Netherlands.

[19] Blackwell Jr,R.H., "Blade design for reduced helicopter vibration", Journal of the American Helicopter Society,Vol.28(3), July 1983, pp. 33-41.

[20] Friedmann,P.P.,"Optimum design of rotor blades for vibration reduction in forward flight",Journal of the American Helicopter Society,Vol.29(4),October 1985,pp. 70-80.

[21] Lim,J.W.,"Aeroelastic Optimization of a Helicopter Rotor",Ph.D. Thesis,University of Maryland,College Park,MD,1988.

[22] Ganguli,R. and Chopra,I.,"Aeroelastic optimization of an advanced geometry helicopter rotor",Journal of the American Helicopter Society,Jan 1998,Vol.41(1),pp 18-28.

[23] Gandhi,F.,Frecker,M., and Nissky,A.,"Design optimization of a Controllable Camber Rotor Airfoil",AIAA Journal,2008,Vol.46(1),pp. 142-153.

[24] Friedmann,P.P.,and Millott T.A.,"Vibration reduction in rotorcraft using active control:a comparison of various approaches",Journal of Guidance,Control and Dynamics,July-Aug 1995,Vol.18(4),pp. 664-673.

[25] Chen,P.and Chopra,I.,"Wind-tunnel test of a smart rotor model with individual blade twist control",Journal of Intelligent Materials and Structures,8(5):414-425,May 1997.

[26] Wilbur,Mathew L.,Mirick,Paul H.,Yaeger Jr.,William T.,Langston,Chester W.,"Vibratory Loads Reduction Testing of the NASA/Army/MIT Active twist rotor",presented at AHS 57h Annual Forum,Washington D.C.,May 2001.

[27] Thakkar,D.,and Ganguly,R.,"Induced shear actuation of helicopter rotor blade for active twist control",Thin-walled structures,2007,45(1):111-121.

[28] Shaw,J.,and Albion,N.,"Active Control of Helicopter Rotor for Vibration Reduction",Journal of the American Helicopter Society,Vol. 25(3),July 1980,pp.32-39.

[29] Nguyen,K., and Chopra,I.,"Application of Higher Harmonic Control to Rotors Operating at High Speed and Thrust",Journal of the American Helicopter Society,Vol. 35(3),1990,pp.78-89.

[30] Nguyen,K., and Chopra,I.,"Effect of Higher Harmonic Control(HHC) on performance and control loads",Journal of Aircraft,Vol. 29(3),May-June 1992.

[31] Payne,P.R.,"Higher Harmonic Control",Aircraft Engineering,Vol. 30(354),August 1958,pp.222-226.

[32] Nguyen,K., and Chopra,I.,"Effect of Higher Harmonic Control(HHC) to Hingeless Rotors",Vertica,Vol. 14(4),October 1990,pp.545-556.

[33] Hammond,C.E.,"Wind Tunnel Results Showing Rotor Vibratory Loads Reduction using Higher Harmonic Blade Pitch",Journal of the American Helicopter Society,Vol. 28(1),January 1983,pp.10-15.

[34] Shaw,J.,Albion,N.,Hanker,E.J., and Teal,R.S.,"Higher Harmonic Control:Wind Tunnel demonstration of Fully Effective Vibratory Hub Forces Suppression",Journal of the American Helicopter Society,Vol. 34(1),January 1989,pp. 14-25.

[35] Nguyen,K.,Betzina,M.,and Kitaplioglu,C.,"Full-Scale Demonstration of Higher Harmonic Control for Noise and Vibration Reduction on the XV-15 Rotor",Journal of the American Helicopter Society,Vol. 46(3),July 2001,pp. 182-191.

[36] Sissingh,G.J.and Donham,R.E.,"Hingeless Rotor Theory and Experiment on Vibration Reduction by Periodic Variation of Conventional Controls",NASA SP-352,1974,pp.261-277.

[37] Wood,E.R.,Powers,R.W.,Cline,C.H.,and Hammond,C.E.,"On Developing and Flight Testing a Higher Harmonic Control System",Journal of the American Helicopter Society,Vol. 30(1),January 1985,pp. 3-20.

[38] Miao,W.,Kotapalli,S.B.R.,and Frye,H.M.,"Flight Demonstration of Higher Harmonic Control on the S-76",American Helicopter Society Forum,Washington D.C.,June 1986.

[39] Achache,M.,and Poychroniadis,M.,"Higher harmonic control:Flight test of an experimental system on an SA-349 research Gazelle", AHS forum,Washington D.C.,June 1986.

[40] Nguyen,K.,and Chopra,I.,NASA Technical Memorandum 103846,March 1991.

[41] Kretz,M.,"Research in Multi-cyclic and Active Control of Rotary Wings",Vertica,Vol 1,No.1/2,1976,pp.95-105.

[42] Ham,N.D.,"Helicopter Individual Blade Control and its Applications",American Helicopter Society 39th Annual Forum,St.Louis,MO,May 1983,pp.613-623.

[43] Ham,N.D.,"A Simple System for Helicopter Blade Individual Blade Control using Model Decomposition",Vertica,Vol.4,(1/2),pp.23-28,1980.

[44] Ham,N.D.,"Helicopter Individual Blade Control research at MIT,1977-1985",Vertica,Vol.11,(1/2),pp.109-122,1987.

[45] Singh,M., Dhanalakshmi, K. and Chakrabarty S.,"Navier-Stokes Analysis of Airfoils with Gurney Flap",Journal of Aircraft,Vol. 45(6),2007,pp. 1487-1493.

[46] Maughmer,M., and Bramesfeld,G.,"Experimental Investigation of Gurney Flaps",Journal of Aircraft,Vol. 45(6),2008,pp. 2062-2067.

[47] Yee,K., Joo,W., Lee,D H ,"Aerodynamic Performance Analysis of a Gurney Flap for Rotorcraft Application",Journal of Aircraft,Vol. 44(3),2007,pp. 1003-1014.

[48] Ormiston,R.A.,"Aeroelastic considerations for rotorcraft primary control with on-blade elevons",American Helicopter Society 57th Annual Forum Proceedings,AHS[129].

[49] J. Shen and I. Chopra. Swashplateless helicopter rotor with trailing-edge flaps. Journal of Aircraft, 41(2):208–214, March-April 2004.

[50] J. Shen, I. Chopra, and W. Johnson," Performance of swashplateless ultralight helicopter rotor with trailing-edge flaps for primary flight control",American Helicopter Society 59th Annual Forum Proceedings,AHS(131).

[51] Shen,Jinwei,"Comprehensive Aeroelastic Analysis of Helicopter Rotor with Trailing- Edge Flap for Primary Control and Vibration Control",PhD thesis,UMD,College Park,2003.

[52] J. Shen and I. Chopra. Aeroelastic modeling of trailing-edge-flap helicopter rotors including actuator dynamics. Journal of Aircraft, 41(6):1465–1472, November-December 2004.

[53] J. Shen, M. Yang, and I. Chopra. Swashplateless helicopter rotor with trailing-edge flaps for flight and vibration control. Journal of Aircraft, 43(2):346–352, March-April 2006].

[54] Falls, J., Datta, A., and Chopra, I., "Design and Analysis of Trailing-Edge Flaps and Servotabs for Primary Control," Proceedings of the 63rd Annual Forum of the American Helicopter Society, Virginia Beach, VA, May 2007.

[55] Falls,Jaye,"Design and Performance Prediction of Swashplateless Rotor with Trailing-Edge Flaps and Tabs",PhD thesis,UMD,College Park,2010.

[56] Milgram, J. and Chopra, I., "A Parametric Design Study for Actively Controlled Trailing Edge Flaps," *Journal of the American Helicopter Society*, Vol. 43, No. 2, April 1998, pp. 110-119.

[57] Straub.F.,Arbabd.V.,Birchette.T.,and Lau.B.,"Wind tunnel test of the SmartActive Flap Rotor,"American Helicopter Society 65th Annual Forum Proceedings, Ft.Worth,TX,May 27-29, 2009.

[58] Friedmann,P.P.,and Millott .T.A.," Vibration reduction in rotorcraft using active control:a comparison of various approaches",Jounal of Guidance, Control and Dynamics, Vol.18(4)Jul-Aug 1995, pp. 664-673.

[59] Koratkar, N. and Chopra, I., "Analysis and Testing of Mach-Scaled Rotor with Trailing-Edge Flaps," *AIAA Journal*, Vol. 38, No. 7, July 2000, pp. 1113–1124.

[60] Milgram,Judah Henry,"A Comprehenensive aeroelastic analysis of helicopter main rotors with trailing edge flaps for vibration reduction",PhD thesis,UMD,College Park,1997.

[61] Roget, B. and Chopra, I., "Wind-Tunnel Testing of Rotor with Individually Controlled Trailing-Edge Flaps for Vibration Reduction," *Journal of Aircraft*, Vol. 45, No. 3, May-June 2008, pp. 868-879.

[62] Konstanzer, P., Enenkl, B., Aubourg, P. A. and Cranga, P., "Recent Advances in Eurocopter's Passive and Active Vibration Control," Proceedings of the 64th Annual Forum of the American Helicopter Society, Quebec, Canada, April 2008.

[63] Jain, R., Szema, K., Munipalli, R., Yeo, H. and Chopra, I., "CFD-CSD Analysis of Active Control of Helicopter Rotor for Performance Improvement," Proceedings of the 65th Annual Forum of the American Helicopter Society, Grapevine, Texas, May 2009.

[64] Theodore, C. R., Cheng, R. P. and Celi, R., "Effects of Higher Harmonic Control on Rotor Performance," Proceedings of the 56th Annual Forum of the American Helicopter Society, Virginia Beach, VA, May 2000.

[65] Yeo,H.,"Assessment of active controls for Rotor Performance Enhancement",Journal of the American Helicopter Society, Volume. 53.(2).,April 2008, pp.154-163.

[66] Bangalore,A.,and Sankar,L.N.,"Forward flight analysis of slatted rotors using Navier-Stokes' method".Journal of Aircraft,34(1):80-86,1997.

[67] Martin,P.B.,McAlister,K.W.Chandrashekhara,M.S.and Geissler,W.,"Dynamic Stall Measurements and computations for a VR-12 Airfoil with a Variable Droop Leading Edge",presented at AHS 59th Annual Forum,Phoenix,Arizona,May6-8,2003.

[68] Wong,Tin-Chee,O'Malley,James A.,III, and O'Brien,David M.,Jr.,"Investigation of Effect of Dynamic Stall and its Alleviation on Helicopter Performance and Loads",presented at AHS 62nd Annual Forum,Phoenix,Arizona,2006.

[69] McAlister, K. W., and Tung, C., "Suppression of Dynamic Stall with a Leading-Edge Slat on a VR-7 Airfoil," NASA Technical Paper 3357 and ATCOM Technical Report 92-A0-013, March 1999.

[70] Noonan,K.W.,Yeager,Jr.,W.T.,Singleton,J.D.,Wilbur,M.L.,and P.H.Mirick,"Evaluation of Model Helicopter Main Rotor Blade with Slotted Airfoils at the tip",Proceedings of the 55th Annual Forum of the American Helicopter Society,Montreal,Canada,May 25-27, 1999.

[71] Carr,N.W., Chandrashekhara,M.S., Wilder,M.C., and Noonan,K.W.,"Effect of compressibility on Suppression of Dynamic Stall using a Slotted Airfoil",Journal of Aircraft,Vol 38,No.2,March-April 2001.

[72] Chandrashekhara,M.S.,"A Review of Compressible Dynamic Stall Control Principles and Methods",Proceedings of the Tenth Asian Congress of Fluid Mechanics,May 17-21,2004,Peradeniya,Sri Lanka.

[73] Narramore, J. C., McCroskey, W. J., and Noonan, K. W., "Design and Evaluation of Multi-Element Airfoils for Rotorcraft," Proceedings of the 55th Annual Forum of the American Helicopter Society, Montreal, Canada, May 25-27, 1999, pp. 1960-1970.

[74] Yeo, H., and Lim, J. W., "Application of a Slotted Airfoil for UH-60A Helicopter Performance," Proceedings of The American Helicopter Society Aerodynamics, Aeroacoustics, and Test and Evaluation Technical Specialists Meeting, San Francisco, CA, January 23-25 2002.

[75] Lorber, P. F., Bagai, A., and Wake, B. E., "Design and Evaluation of Slatted Airfoils for Improved Rotor Performance," 62nd Annual Forum and Technology Display of the American Helicopter Society International, Phoenix, AZ, May 9-11 2006.

[76] Mishra, A., Ananthan, S., Baeder, J., Opoku, D., Wake, B. and Lin, R., "Coupled CFD/CSD Prediction of the Effects of Leading Edge Slat on Rotor Performance," Proceedings of the 65th Annual Forum and Technology Display of the American Helicopter Society International, Dallas, TX, May 27-29, 2009.

[77] Yeo,H,"Assessment of active controls for Performance Enhancement,"Proceedings of the 62nd Annual Forum of the American Helicopter Society, Phoenix, Az, 2006.

[78] Jain,R.,Yeo,H.and Chopra I.,"An Examination of Rotor Loads due to On-Blade Active Controls for Performance Enhancement using CFD-CSD Analysis,"Proceedings of the AHS Specialists Conference on Aeromechanics, Jan 20-22,2010, San Francisco,CA.

[79] Bousman, W. G., and Kufeld, R. M., "UH-60A Airloads Catalog," NASA TM 2005-212827, August 2005.

[80] Chopra, I. and Bir, G., "University of Maryland Advanced Code : UMARC," American Helicopter Society Aeromechanics Specialists Conference, San Franscisco, CA, January 1994.

[81] Bagai,A. and Leishman,J.G.,"Rotor Free-Wake Modeling using a Relaxation Technique-Including comparisons with experimental data"Journal of the American Helicopter Society, Vol.40,(2),April 1995.

[82] Leishman,J.G., Beddoes,T.S.,"A Semi-Empirical Model for Dynamic Stall,"Journal of the American Helicopter Society, July 1989, pp.3-17.

[83] Datta A.,Chopra I.,"Validation of Structural and Aerodynamic Modeling Using UH-60A Airloads Program Data,"Journal of the American Helicopter Society,Vol.51,(1),January 2006,pp. 43-58.

[84] McHugh,F.J.,"What are the lift and propulsive force limits at high speed for the conventional rotor?,"Proceedings of the 34th Annual Forum of the American Helicopter Society, Washington D.C.,May 1978.

[85] Hoerner.S.F., and Borst H.V.,"Characteristics of Trailing-edge Wing Flaps," Fluid-Dynamic Lift:Practical Information on Aerodynamic and Hydrodynamic Lift,Hoerner Fluid Dynamics, Vancouver,WA,1985,Chap.V,pp.5-1 to 5-42.

[86] Smith, M.J.,Wong,T.C., Potsdam, M.A.,Baeder, J.,and Phanse,S.,"Evaluation of computational fluid dynamics to determine two-dimensional airfoil characteristics for rotorcraft applications",Journal of the American Helicopter Society, Volume 51(1), January 2006, pp. 63-77.

[87] Johnson, W., "Self-tuning Regulators for Multicyclic Control of Helicopter Vibration", NASA Technical Paper 1996, March 1982.

[88] Landgrebe,A.,Lorber,P.,and Stauter,R.,"A comprehenensive Hover Test of the Airloads and Airflow of an Extensively Instrumented Model Helicopter Rotor,"Proceedings of the 45th Annual Forum of the AHS,Boston,MA,May 1989.

[89] Duraisamy,K.,Sitharaman,J. and Baeder, J."High Resolution Wake-capturing Methodology for Accurate Simulation of Rotor Aerodynamics",Proceedings of the 61st Annual Forum of the American Helicopter Society, Dulles, Texas, June 8-11, 2005.

[90] Chopra,I.,and McCloud.J.L.,III,"A Numerical Simulation Study of Open-Loop, Closed-Loop and Adaptive Multicyclic Control Systems",Journal of the American Helicopter Society, Volume 28(1),January 1983, pp. 63-77.

[91] Milgram,J.and Chopra,I.,"Helicopter Vibration Reduction with Trailing-Edge Flaps",Proceedings of the 36th AIAA/ASME/ASCE/AHS/ASC Structures,Structural Dynamics and Materials Conference, New Orleans,LA,April 10-12,1995.